

AD-A251 588



2

PL-TR-91-2137

INVESTIGATIONS INTO ATMOSPHERIC RADIATIVE
PROCESSES IN THE 50 - 300 km REGIME

D. C. Robertson, P. K. Acharya, S. M. Adler-Golden,
L. S. Bernstein, F. Bien, J. W. Duff, J. H. Gruninger,
R. L. Sundberg, R. J. Healey, J. M. Sindoni,
P. M. Bakshi, A. Dalgarno, and B. Zygelman

Spectral Sciences, Inc.
99 South Bedford Street
Burlington, MA 01803

30 April 1991

DTIC
ELECTE
MAY 20 1992
S. D.

Final Technical Report
January 1989 - March 1991

APPROVED FOR PUBLIC RELEASE,
DISTRIBUTION UNLIMITED



Phillips Laboratory
Air Force Systems Command
Hanscom Air Force Base, Massachusetts 01731-5000

92-13350

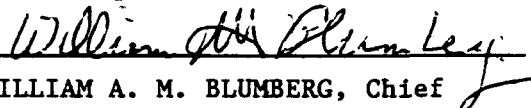


92 5 10 2


This technical report has been reviewed and is approved for publication.



DEAN F. KIMBALL
Contract Manager
Simulation Branch



WILLIAM A. M. BLUMBERG, Chief
Simulation Branch
Optical Environment Division



ALAN D. BLACKBURN, Col, USAF, Director
Optical Environment Division

This document has been reviewed by the ESD Public Affairs Office (PA) and is releasable to the National Technical Information Service (NTIS).

Qualified requestors may obtain additional copies from the Defense Technical Information Center. All others should apply to the National Technical Information Service.

If your address has changed, or if you wish to be removed from the mailing list, or if the addressee is no longer employed by your organization, please notify PL/IMA, Hanscom AFB, MA 01731-5000. This will assist us in maintaining a current mailing list.

Do not return copies of this report unless contractual obligations or notices on a specific document requires that it be returned.

REPORT DOCUMENTATION PAGE			Form Approved OMB No 0704-0188	
<small>Public reporting burden for this collection of information is estimated to average 1 hour per response, including the time for reviewing instructions, searching existing data sources, gathering and maintaining the data needed, and completing and reviewing the collection of information. Send comments regarding this burden estimate or any other aspect of this collection of information, including suggestions for reducing this burden, to Washington Headquarters Services, Directorate for Information Operations and Reports, 1215 Jefferson Davis Highway, Suite 1204, Arlington, VA 22202-4302, and to the Office of Management and Budget, Paperwork Reduction Project (0704-0188), Washington, DC 20503.</small>				
1. AGENCY USE ONLY (Leave blank)	2. REPORT DATE 30 April 1991	3. REPORT TYPE AND DATES COVERED Final Report (1/89-3/91)		
4. TITLE AND SUBTITLE Investigations into Atmospheric Radiative Processes in the 50 - 300 km Regime		5. FUNDING NUMBERS C - F19628-87-C-0130 PE - 63220C PR - S321 TA - 22 WU - AA		
6. AUTHOR(S) L.S. Bernstein R.L. Sundberg A. Dalgarno D.C. Robertson F. Bien R.J. Healey* B. Zygelman° P.K. Acharya J.W. Duff J.M. Sindoni* S.M. Adler-Golden J.H. Gruninger P.M. Bakshi†				
7. PERFORMING ORGANIZATION NAME(S) AND ADDRESS(ES) Spectral Sciences, Inc. 99 South Bedford Street, #7 Burlington, MA 01803-5169		8. PERFORMING ORGANIZATION REPORT NUMBER SSI-TR-188		
9. SPONSORING/MONITORING AGENCY NAME(S) AND ADDRESS(ES) Phillips Laboratory Hanscom AFB, MA 01731-5000 Contract Manager: Dean Kimball/GPOS		10. SPONSORING/MONITORING AGENCY REPORT NUMBER PL-TR-91-2137		
11. SUPPLEMENTARY NOTES *Yap Analytics, Inc., 594 Marrett Rd., Lexington, MA; †Boston College, Chestnut Hill, MA; #Smithsonian Observatory, Harvard University, Cambridge MA; °University of Nevada, Dept. of Physics, Las Vegas, NV				
12a. DISTRIBUTION/AVAILABILITY STATEMENT Approved for Public Release; Distribution Unlimited.		12b. DISTRIBUTION CODE		
13. ABSTRACT (Maximum 200 words) This report describes research into high-altitude infrared (IR) radiance models to describe sources of high-altitude NLTE radiation in the IR spectral region. Many of the models have been combined into SHARC, the Strategic High Altitude Radiance Code. SHARC calculates the radiation from quiescent and auroral atmospheres in the 2-40 μ m spectral region for arbitrary paths that lie above 50 km, including space viewing. In related activities, analyses of data taken under the SPIRIT and EXCEDE programs have been analyzed. The SPIRIT I data were used to study O ₃ , NO, and CO ₂ IR Emissions. The EXCEDE flight in April 1990 observed atmospheric emissions following excitation by an electric beam. Models for new applications of the Impulse Approximation for low-energy collision processes and for precise calculation of the ground state structure of atomic oxygen are also presented.				
14. SUBJECT TERMS Infrared Radiation Impulse Approximation Thermosphere Aurora Atmospheric Radiance Atomic Oxygen Mesosphere			15. NUMBER OF PAGES 112	
			16. PRICE CODE	
17. SECURITY CLASSIFICATION OF REPORT UNCLASSIFIED	18. SECURITY CLASSIFICATION OF THIS PAGE UNCLASSIFIED	19. SECURITY CLASSIFICATION OF ABSTRACT UNCLASSIFIED	20. LIMITATION OF ABSTRACT SAR	

TABLE OF CONTENTS

SECTION	PAGE
1 INTRODUCTION	1
2 THE SHARC COMPUTER MODEL	2
2.1 The INTERPRETER Program	3
2.2 SHARC	5
2.3 Ambient Molecular Populations	5
2.4 Auroral Molecular Populations	8
2.5 LOS Spectral Radiance	9
2.6 Comparisons to Field Data	10
2.7 Multiple Atmospheric Regions	13
2.8 Atmospheric Spatial Structures	14
3 SHARC AURORAL MODEL	20
3.1 Model Description	20
3.1.1 Aurora Definition	21
3.1.2 Auroral Kinetics	22
3.1.3 Radiative Transfer Model for CO ₂ (4.3 μm)	28
3.2 Comparison of SHARC with AARC	29
3.3 Illustrative Calculation	33
4 ANALYSIS OF SPIRIT 1 DATA	36
4.1 9-12 μm Ozone (ν ₃) Emission	37
4.2 Identification of O ₃ High Vibrational States	39
4.3 CO ₂ (ν ₂) and NO(Δv=1) Emissions	39
4.4 O and H Profiles Derived for SPIRIT 1 and SPIRE	43
5 ANALYSIS OF EXCEDE DATA	46
5.1 Sensor Module CVF Instrumentation	47
5.2 Representative CVF Data	48
5.3 EXCEDE Kinetic Model	53
5.3.1 Molecular Radiators	54
5.3.2 Model Predictions	54
5.4 Summary	57
6 CONCEPTS FOR A SMALL ROCKET EXPERIMENT	58
6.1 Stray Light Analysis	58
6.1.1 Prototype Telescope Baffle	59
6.1.2 Prototype Optical System	60
6.2 Prototype Instrumentation Package	64
6.2.1 Design Constraints	64
6.2.2 Diffraction Grating Selection	66
6.2.3 Spectrometer Design	66
6.2.4 SSPM Detectors	68
7 IMPULSE APPROXIMATION FOR ATOM-MOLECULE COLLISIONS	69

TABLE OF CONTENTS (Continued)

SECTION	PAGE
8 FINE-STRUCTURE TRANSITIONS IN COLLISIONS OF OXYGEN ATOMS	75
8.1 Introduction	75
8.2 Theoretical Formulation	75
9 REFERENCES	83
APPENDIX A	A-1

LIST OF ILLUSTRATIONS

FIGURE	PAGE
1 Major Components of SHARC	4
2 Calculational Sequence for SHARC	6
3 Comparison of Calculated and Observed Radiation in the 15 μm Band of CO_2 for Limb Viewing from Space	10
4 Comparison of Calculated and Observed Daytime Radiation in the 4.3 μm CO_2 Band for Limb Viewing from Space	11
5 Comparison of Calculated and Observed Nighttime Radiation in the 9.6 μm O_3 Band for Limb Viewing from Space	12
6 Comparison of Calculated and Observed Radiation in the 5.3 μm NO Band for Limb Viewing from Space	12
7 Layering Schematic with Local Auroral Region	14
8 Major Components of the Auroral Model	20
9 Ion Pair Production Rate for a Class III ⁺ Aurora	22
10 Steady State Secondary Electron Distribution at an Altitude of 100 km for a Class III ⁺ Aurora	24
11 Comparison of the SHARC $\text{NO}(\Delta v=1)$ Time-Dependent Photons/Ion Pair with the AARC Efficiency	30

LIST OF ILLUSTRATIONS (Continued)

FIGURE		PAGE
12	Comparison of the SHARC NO($\Delta v=1$) Predictions of Photon/Ion Pair Efficiencies Using the EXCEDE and AARC Rate Constants for Eq. (11)	31
13	SHARC Prediction of the N ₂ (v) Efficiencies (Quanta/Ion Pair) for Several Production Mechanisms	32
14	AARC Prediction of the N ₂ (v) Efficiencies (Quanta/Ion Pair) for Several Production Mechanisms	32
15	Comparison of the SHARC and AARC NO ⁺ ($\Delta v=1$) Efficiencies (Photons/Ion Pair)	33
16	SHARC Prediction of Ambient and Auroral IBC II Altitude Dependent Volumetric Emission Rates for NO($\Delta v=1$)	34
17	Comparison of the SHARC Spectral Radiance with FWI Data for a Near Zenith Line-of-Sight	35
18	Ozone Limb Spectra from SPIRIT 1 with Kaiser-Bessel Apodization	38
19	Comparison of Standard Nighttime Ozone Density Profiles with Profile Derived from SPIRIT 1 Data	38
20	Comparison of Observed and Synthetic Unapodized Ozone Spectra	41
21	CO ₂ ν_2 Limb Radiance Profile From SPIRIT 1, and Average of SPIRE Data	41
22	Typical CO ₂ ν_2 Spectra at Various Tangent Heights with Kaiser-Bessel Apodization	42
23	NO $\Delta v=1$ (5.3 μ m) Limb Radiance Profile, Showing Second-Degree Fit and Full Limb Corrected SPIRIT 1 Data	42
24	Limb and Local Kinetic Temperature Profiles from SPIRIT 1 NO $\Delta v=1$ Data	43
25	O Atom Profiles Calculated from the Inverted SPIRIT 1 Hot Band Data	44

LIST OF ILLUSTRATIONS (Continued)

FIGURE	PAGE
26 H Atom Profiles Calculated from the SPIRE and SPIRIT 1 Data	45
27 Sensor Module CVFs Fields-of-View	48
28 Electron Beam Enhancement of NO($\Delta v=1$) and NO($\Delta v=2$) Radiance for Three Electron Gun Pulses	49
29 Effect of Electron Beam on O ₃ (9.6 μ m) Radiance During Four Electron Gun Pulses	50
30 Time-Dependent Effects at an Altitude of 100 km Illustrated by the 8° and 20° CVFs	51
31 Altitude Dependence of the 8° CVF IR Data	52
32 Altitude Dependence of the 20° CVF IR Data	52
33 Model Prediction of the Time-Dependence of the O°, 8°, and 20° CVFs at an Altitude of 100 km	55
34 Model Prediction of the Altitude Dependence for the 8° CVF	56
35 Model Prediction of the Altitude Dependence for the 20° CVF	56
36 Small Aperture Foreoptics Design	60
37 Point Source Transmittance for a Small-Diameter Optical System	62
38 Stray Light Equivalent Spectral Radiance for a Small-Diameter Optical System that is Viewing the Earth Limb	63
39 Differential Cross Sections for the Exact and PA Calculations vs. Energy Loss for the Collision Process Li ⁺ + N ₂ (v=0) → Li ⁺ + N ₂ (v=2,3)	73

LIST OF TABLES

TABLE		PAGE
1	Atmospheric Structure Scales	15
2	Energies & Band Centers for O ₃ Vibrational States	40
3	1X Telescope Optical Prescription	61
4	Design Goals for a Small Rocket Spectrometer	65
5	Connections between Atomic and Molecular States for Two Oxygen ³ P Atoms.	77
6	Values of the Parameter C ₅	81



Accession For	
NTIS GRA&I	<input checked="" type="checkbox"/>
DTIC TAB	<input type="checkbox"/>
Unannounced	<input type="checkbox"/>
Justification	
By	
Distribution/	
Availability Codes	
Dist	Avail and/or Special
A-1	

1. INTRODUCTION

This final report describes research into high-altitude infrared (IR) radiance models done under Contract No. F19628-87-C-0130. A major result of this effort has been the development of predictive models which have been combined into a general calculational model for atmospheric radiance. These models include sources of high-altitude NLTE (Non Local Thermodynamic Equilibrium) radiation in the IR spectral region. Many of the models have been combined into SHARC, the Strategic High Altitude Radiance Code. SHARC calculates atmospheric radiance in the 2-40 μm spectral region for arbitrary line-of-sight (LOS) paths that lie above 50 km, including space viewing. The latest version, SHARC-2,^{1,2} also includes a fully integrated auroral model.

At lower altitudes molecular collisions are many and frequent, so collisional processes dominate radiative ones, and molecular excited states are quenched before they can radiate. The molecules are then said to be in Local Thermodynamic Equilibrium (LTE), and the local temperature, total number densities, and molecular mixing ratios suffice to determine excited state populations. At higher altitudes (above 40-60 km), competing processes like radiative decay become more important and eventually dominate collisional deexcitation.^{2,3} Atmospheric radiation then arises from emissions by molecules that are in NLTE. The work described in this report and the resultant computer models address the NLTE regime.

The NLTE models and the resultant SHARC Code are described in Sections 2 and 3. In related activities, data taken under the SPIRIT, EXCEDE, and SPIRE programs have been analyzed and compared to model predictions. The SPIRIT 1 data were used to study O_3 emission in the 9.6 μm band, determination of O and H atom profiles, and NO and CO_2 emissions in their 5.3 and 15 μm bands. The EXCEDE flight in April, 1990, returned much useful data; Section 5 presents an initial look at the spectral data. The SPIRE data were used to help validate parts of SHARC. Other modeling and concepts for possible new measurements approaches are discussed in Sections 6, 7, and 8.

2. THE SHARC COMPUTER MODEL

Under NLTE conditions, both the ground- and excited-state densities must be modeled for each molecule and transition. The population of the various excited vibrational states deviate most strongly from LTE. The relevant NLTE processes fall into three groups: radiative, collisional, and chemical:

- Radiative: Pumping mechanisms include absorption of sunshine, upwelling earthshine, and photons emitted by other molecules. Subsequent spontaneous emission then results in the observed radiation.
- Collisional: Non-reactive, inelastic collisions, which result in vibrational and rotational energy exchange or transfer, are still significant in the upper atmosphere. Although collisions are less frequent due to low number densities, molecule-radical interactions, such as interactions with O atoms, and near-resonant interactions, such as V-V exchange between N₂ and CO₂, are important.
- Chemical: Inelastic two- and three-body collisions combined with chemical reactions frequently leave highly excited products which subsequently cascade down to the ground state by emitting photons. An example is ozone recombination⁴ via $O + O_2 + M \rightarrow O_3^* + M$ and formation of vibrationally excited NO via $O_2 + N(^2D)^5$ (atomic nitrogen is formed during auroral activity).

Identifying and quantifying the important IR radiators depend on data obtained from field measurements; these indicate that the major sources (and bands) above 80 km are NO (5.3 μm), CO₂ (15 μm and 4.3 μm), and O₃ (9.6 μm). Other emitters of varying importance include CO (4.6 μm), O₂ (1.27 μm), and OH (3.0 & 1.5 μm).^{3,6} At lower altitudes, H₂O (2.7 & 6.3 μm) and OH become increasingly important, and the strength of NO emissions decreases.

Various models that describe these processes have been synthesized into an overall computer model, SHARC (the Strategic High-Altitude Radiance Code).^{2,7-10} SHARC calculates NLTE and LTE radiance and transmittance for paths between 50 and 300 km (including space viewing) within the 2-40 μm spectral region and with a resolution of 0.5 cm^{-1} .

It allows arbitrary paths (e.g., limb, horizontal, vertical, or slant) between any two points within or without the atmosphere. The code presently includes the six most important ambient molecules at high altitude: CO₂, O₃, NO, H₂O, CO, and OH. In addition, SHARC calculates auroral emission from CO₂, NO, and NO⁺.

SHARC is a completely new code. Modular construction has been emphasized so that models and model parameters can be modified or upgraded as additional data and/or better models become available. It is a successor to the AFGL HAIRM Code.^{11,12} Both SHARC and HAIRM are based on analyses of various AFGL lab and field measurements for these radiative processes. The molecular line parameters are taken from the 1986 HITRAN line atlas¹³ and supplemented with additional lines for the high vibrational states of O₃(ν_3) in the 10-12 μ m spectral region¹¹ and lines for auroral emission by NO and NO⁺.¹⁴ Parameters in the SHARC data base can be upgraded as additional data are analyzed. This upgrade ability, its integrated auroral model, flexible geometry package, and interactive input module represent significant advances over HAIRM.

The three major SHARC components are indicated in Fig. 1. The INTERPRETER, which is a modified version of that furnished with the Sandia CHEMKIN code,¹⁵ prepares the differential equations for the chemical/kinetic reaction scheme. This module is run only when changes have been made to either the reaction scheme or any associated rate constants. The SHARC component calculates the required atmospheric transmittance and radiance. The chemistry modules, ambient and auroral, utilize differential equations set up by the INTERPRETER. The PLOTTING package generates spectral radiance plots.

2.1 The INTERPRETER Program

Within SHARC, the CHEMKIN module computes the steady-state and time-dependent number densities of vibrationally excited atmospheric species from a set of chemical kinetics/reaction mechanisms. The chemical kinetics scheme describes molecular formation, all forms of vibrational energy transfer, and the absorption of solar and/or

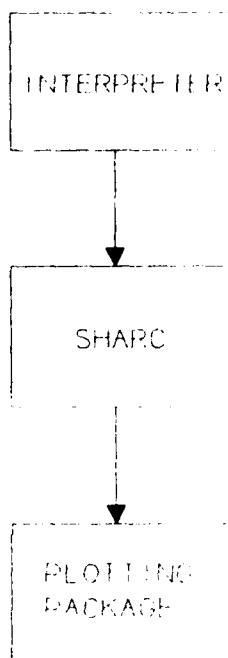


Figure 1. Major Components of SHARC.

earthshine radiation. The INTERPRETER program, which is based entirely on and includes subroutines directly from the Sandia Livermore INTERPRETER code,¹⁵ reads a symbolic description of the chemical kinetics mechanisms and creates a binary "linking" file with all the kinetics information. The Sandia CHEMKIN package is described as¹⁵ "a general-purpose, problem-independent, transportable, FORTRAN chemical kinetics code." The SHARC INTERPRETER is a modified version from which information on elements in the periodic table and the thermodynamic data base (useful for combustion reactions), extraneous to the atmospheric application, have been removed. The INTERPRETER reads a symbolic description of an arbitrary chemical kinetics mechanism in a manner that is just as would be written by a chemical kineticist. To be more specific, consider irreversible kinetic (energy transfer or reactive) processes, each given in the general form

$$\sum_{k=1}^K \nu_{ki} C_k \xrightarrow{k_i} \sum_{k=1}^K \nu'_{ki} C_k, \quad (1)$$

where the stoichiometric coefficients ν_{ki} are integers; C_k is the chemical symbol for the k^{th} species; and k_i is the rate constant for the i^{th} process. The INTERPRETER reads these equations and translates the mechanism into the appropriate differential equations

$$\frac{dw}{dt} = \sum_{i=1}^I (\nu'_{ki} - \nu_{ki}) k_i \prod_{k=1}^K [C_k]^{\nu_{ki}} \quad (2)$$

All variables defined in Eqs. (1) and (2) are written into a binary "linking" file for use by SHARC. Although this example is for irreversible processes, SHARC-2 allows reversible vibrational to translational processes. The INTERPRETER only has to be run once for a given kinetics mechanism and data base.

2.2 SHARC

The schematic shown in Fig. 2 illustrates the calculational sequence for SHARC. All modules are called by the MAIN program. The input module is interactive and queries the user for parameters needed by the rest of the code. The chemistry module includes two components, the chemical kinetics (CHEMKIN) and radiative transfer (NEMESIS) modules. They calculate an altitude profile of populations for the various molecular excited and ground states. The auroral module calculates auroral enhancement of the CO_2 , NO , and NO^+ ambient populations. GEOMETRY determines the line-of-sight (LOS) trajectory parameters for the viewing geometry requested by the user. The SPCRAD module calculates the spectral transmittance and radiance for the required LOS path(s).

2.3 Ambient Molecular Populations

The first component of the SHARC Ambient module is CHEMKIN. It computes the steady-state number densities of vibrationally excited atmospheric species for each atmospheric layer. Again these subroutines are based on those in the Sandia Livermore CHEMKIN package.¹⁵

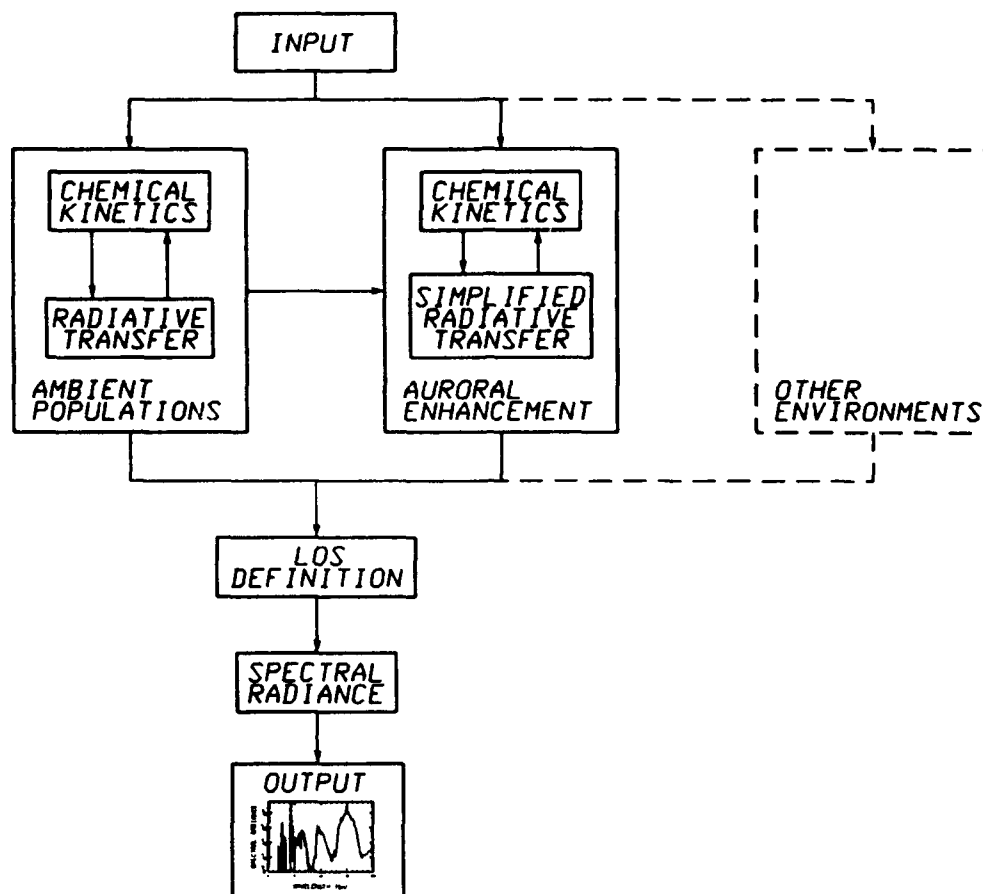


Figure 2. Calculational Sequence for SHARC.

CHEMKIN uses information from the binary "linking" file (species identification, stoichiometric coefficients, and rate constant parameters) to construct steady state equations for the vibrationally excited states

$$\sum_{i=1}^I (\nu_{ki}' - \nu_{ki}) k_i \prod_{k=1}^K [C_k]^{\nu_{ki}} = 0 \quad (3)$$

The variable definitions are identical to those defined in Eq. (2). In general, solving Eq. (3) for the vibrationally excited-state densities requires a nonlinear equation algorithm. However, using the assumption that the ν_{ki} of the vibrationally excited species (i.e., the unknowns in

the problem) are unity, Eq. (3) simply reduces to a set of linearly independent algebraic equations for the N unknown excited-state number densities. This assumption is not overly restrictive and has been used previously in atmospheric radiation models.^{11,14} The information necessary to solve Eq. (3) is simply the atmospheric species number densities and the kinetic temperature from which the rate constants are computed. SHARC then uses a lower/upper (LU) decomposition algorithm to solve for the number densities.

The second component is NEMESIS, the Non-Equilibrium Molecular Emission and Scattering Intensity Subroutine.¹⁶ It computes the enhancement of the atmospheric excited-state layer populations due to layer radiative self-trapping and layer-layer radiative pumping. Some molecular bands, in particular the 4.3 μm CO₂ band, are optically opaque to emitted radiation. Photons emitted in these bands may be absorbed and emitted many times before either escaping the atmosphere or becoming collisionally quenched.

Calculating radiatively enhanced excited-state populations involves:

- determination of layer steady-state source populations, which includes excitation by external light sources, sun and earthshine, and molecular collisions and de-excitation by radiative decay and collisional quenching;
- determination of first-order population enhancements using a Monte Carlo simulation of source photon emissions and their subsequent absorption or escape; and
- determination of the total enhanced populations using a recursive orders-of-enhancement approximation which is initialized by the Monte Carlo first-order results.

The source populations include all sources of excitation exclusive of the internal atmospheric radiative effects of layer self-trapping and layer-layer pumping. CHEMKIN generates the source populations for use by NEMESIS. The Monte Carlo simulation calculates the first-order enhancements and the probabilities that a photon emitted from a layer "i" will create a new excited-state in each layer "j". This simulation involves sampling over the initial emission position, emission

direction, emission frequency, emission line strength, and length of travel. The contribution of each succeeding order-of-enhancement is determined recursively by

$$(P_k) = (P_{k-1})(W) \quad , \quad (4)$$

where (P_k) is the k th-order layer population enhancement matrix, and (W) is the layer-layer absorption probability matrix. Both (P_1) and (W) are calculated by the first-order Monte Carlo calculation.

The end result of each NEMESIS calculation is the total excited-state population distribution for a pair of vibrational levels, where the lower level of each pair may itself be an excited level. A cycling procedure between CHEMKIN and NEMESIS is used to step up the vibrational energy ladder until the top of the ladder is reached. Finally, these enhanced populations are passed to the SPCRAD module for the LOS radiance computation.

2.4 Auroral Molecular Populations

The AURORA module performs a time-dependent calculation to determine auroral species number densities as a function of altitude. The Gear method for stiff differential equations is used to numerically integrate the chemical kinetic rate equations that describe the various auroral chemical and energy transfer processes. This integration package is part of the Sandia CHEMKIN code¹⁵ and thus has been extensively applied to many different types of scientific problems.

Auroral excitations result from the atmosphere's stopping of high-energy electrons impinging upon it. The deposition model for these primary electrons is based upon the work of Grün, Rees, and Strickland and has been discussed in some detail in the AARC manual.¹⁴ The SHARC routines for energy deposition are based upon those used in AARC. The ion pair production rate is obtained from the energy deposition rate by assuming that 35 eV are required to produce each ion pair.

Chemical kinetics mechanisms which lead to population enhancements of NO, NO⁺, and CO₂(4.3 μm) are included in the SHARC-2 data base. The

relevant chemical reactions and energy transfer processes starting with the initial electron deposition are also described in the AARC manual¹⁴ and in Section 3. The mechanisms include kinetic processes for ionization, electronic and vibrational excitation, recombination, chemical reactions, and formation of the secondary electron energy distribution.

2.5 LOS Spectral Radiance

Calculation of the spectral transmittance and radiance for the requested LOS path uses a finite-difference form of the radiative transfer equation. A single-line equivalent width approximation based on the Voigt lineshape is used to calculate segment transmittances and radiances. This approach enables the spectral radiance to be calculated on a line-by-line (LBL) basis at a spectral resolution as high as 0.1 cm^{-1} , although the resolution in the current version of SHARC is set at 0.5 cm^{-1} . Since the radiation computation is explicitly based on the difference of the upper and lower state populations, it is equally valid in both the NLTE and LTE regimes. Line strengths and locations are taken from a modified line file generated from the 1986 AFGL HITRAN line atlas.¹³ The major modifications were addition of some additional lines and changing the line parameter data base to decompose the energy of the lower state into vibrational and rotational energies. This enables the line strengths to be scaled separately for the rotational temperature and the NLTE vibrational population of the lower level.

There is a trade-off between speed and accuracy when the atmosphere is layered into many homogeneous layers. Times for LOS radiance calculations depend linearly on the number of layers. Currently the atmospheric profiles used by SHARC are layered by 2 km from 50 to 150 km and by 10 km steps from 150 to 300 km. Thus the LOS path for a limb calculation with a tangent height of 50 km traverses 129 atmospheric layers.

2.6 Comparisons to Field Data

Initial SHARC validation was accomplished by comparison to field data from the GL SPIRE,¹⁷ SPIRIT 1,¹⁸ and FWI¹⁹ programs. In addition, extensive comparisons have been made to other GL codes to verify both the performance of individual modules and the overall code.

The SPIRE measurements were taken from a sounding rocket with spectrometers that had a spectral resolution of about 2 per cent.¹⁷ The data are for partial to full limb observations. All presented data have been corrected to full limb radiances. Figures 3 and 4 present comparisons for CO₂ radiances integrated over the CO₂ ν_2 and ν_3 bands at 15 and 4.3 μm , respectively. The two calculations in Fig. 3 illustrate the contribution of molecular radiative exchange. The NO-NEMESIS calculation for which the radiance is calculated with just chemical and earthshine excitation processes, illustrates the importance of radiative excitation. The shoulder around 100 km arises from a complicated

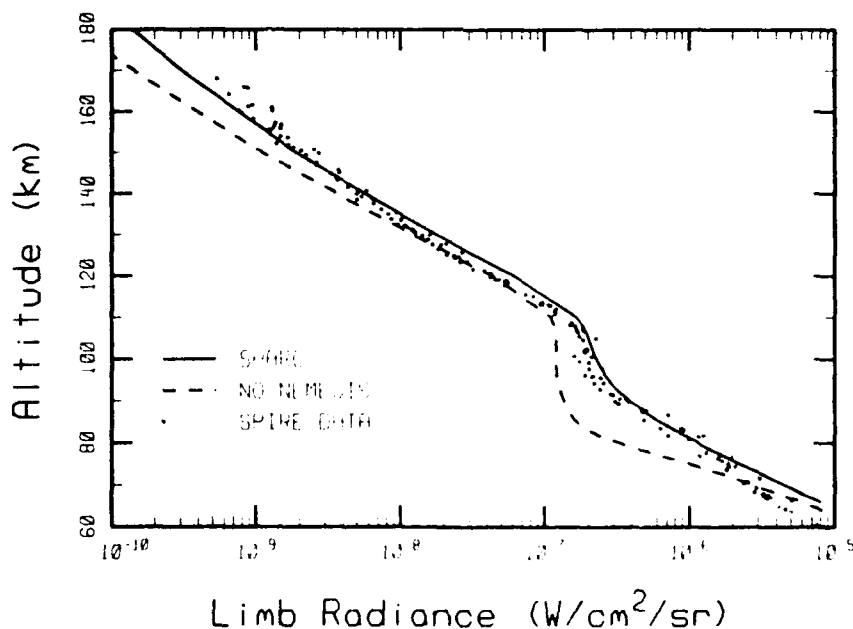


Figure 3. Comparison of Calculated and Observed Radiation in the 15 μm Band of CO₂ for Limb Viewing from Space. The NO-NEMESIS Calculation Does Not Include Molecular Radiative Excitation.

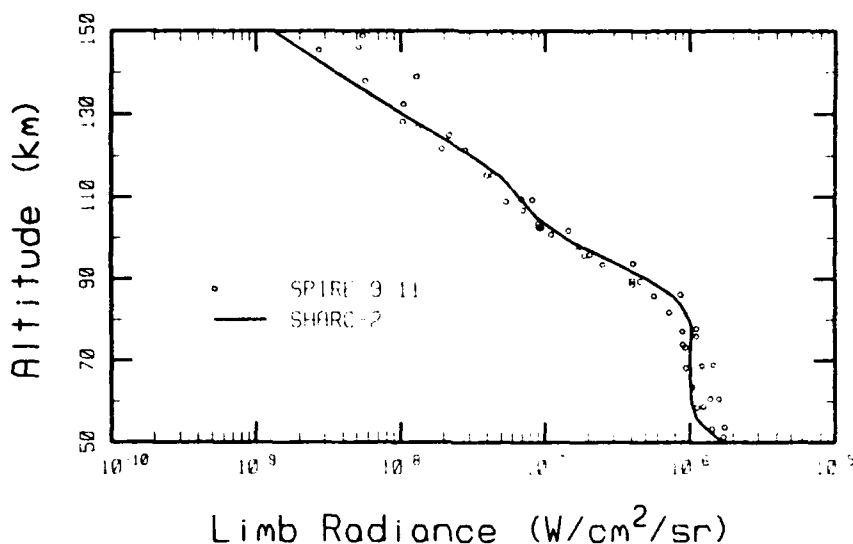


Figure 4. Comparison of Calculated and Observed Daytime Radiation in the $4.3 \mu\text{m}$ CO_2 Band for Limb Viewing from Space.

interplay between optical opacity of the primary CO_2 isotope and excitation of $\text{CO}_2(\nu_2)$ by O atoms. Sunlit SPIRE scans and model calculations are shown for the $4.3 \mu\text{m}$ ν_3 band in Fig. 4. Different phenomena dominate at various altitude regimes. Above 110 km, direct solar excitation of the primary isotope dominates. Below this altitude, the radiance is strongly enhanced both by emission from the minor isotopes and by solar pumping of the $2.7 \mu\text{m}$ band with subsequent radiative decay of the hot bands in the $4.3 \mu\text{m}$ region. The strongest excitations coupled to the $2.7 \mu\text{m}$ band are the $\nu_1=1$ and $\nu_2=2$ states combined with additional ν_3 quanta. The shoulder below 85 km arises from collisional quenching. As the density increases, these NLTE excitations are quickly quenched, and the single ν_3 excitation of the primary isotope again dominates as LTE emissions. There is a small nighttime shoulder around 85 km due to the isotopes (not shown).

Figures 5 and 6 show data-model comparisons for the $9.6 \mu\text{m}$ O_3 and $5.3 \mu\text{m}$ NO bands, respectively. Both model calculations were done for a 60° North (Subarctic) Winter Profile. The primary source of the nighttime limb emission for O_3 in Fig. 5 results from three-body

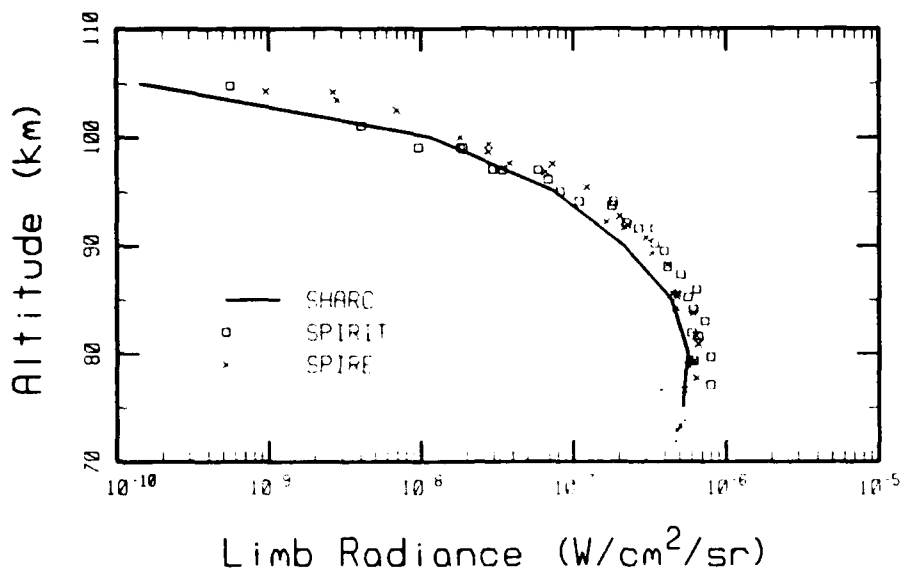


Figure 5. Comparison of Calculated and Observed Nighttime Radiation in the $9.6 \mu\text{m}$ O_3 Band for Limb Viewing from Space.

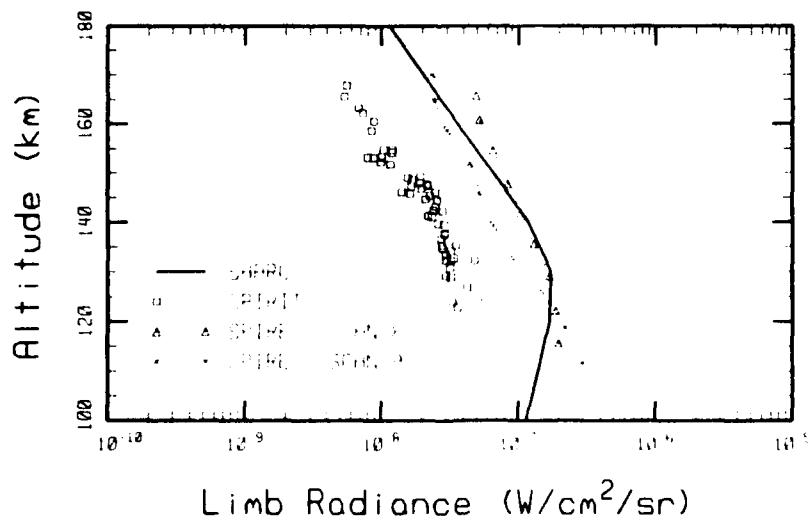


Figure 6. Comparison of Calculated and Observed Radiation in the $5.3 \mu\text{m}$ NO Band for Limb Viewing from Space.

recombination of O_2 with atomic oxygen. The data in the figure are from the SPIRE and from SPIRIT 11^8 field measurements. The model and data are in good agreement. A similar comparison to emissions in the NO band is shown in Fig. 6. Agreement with the SPIRE data is quite good, while the SPIRIT measurements are about a factor of five lower. This is indicative of the effects of atmospheric variability. The strength of NO radiation is proportional to

$$[O] [NO] e^{-2600/T} , \quad (5)$$

where T is the atmospheric temperature and $[O]$ and $[NO]$ are the concentrations; thus, emissions in this band have a strong dependence on the ambient number densities and temperature. As discussed in Section 4, ambient temperatures during the SPIRIT measurements were consistently lower than those during SPIRE.

2.7 Multiple Atmospheric Regions

Much of the nomenclature in the GEOMETRY module has been borrowed from the LOWTRAN-6 geometry routines.²⁰ No knowledge of LOWTRAN 6 is required as GEOMETRY is self-contained. A curved-earth geometry is used for all LOS path calculations; since atmospheric refraction is insignificant under these rarefied conditions, it is not calculated.

The auroral excitation is confined to a finite region within the atmosphere. This has led to the development of local regions with their own atmospheric profiles. A local region can receive auroral excitation due to a prior history of electron dosing or be just a different ambient region. Up to four local regions are allowed.

Local regions are defined by four (latitude, longitude) points plus the upper and lower altitudes of the region. The four (lat,lon) points must form a convex quadrilateral which has no interior angles greater than 180° . Two local regions must not intersect one another, but they can share common boundaries. If a pole is to be within a local region, the input geometry should use the other coordinate system, i.e., use polar coordinates when the local region includes the geomagnetic pole.

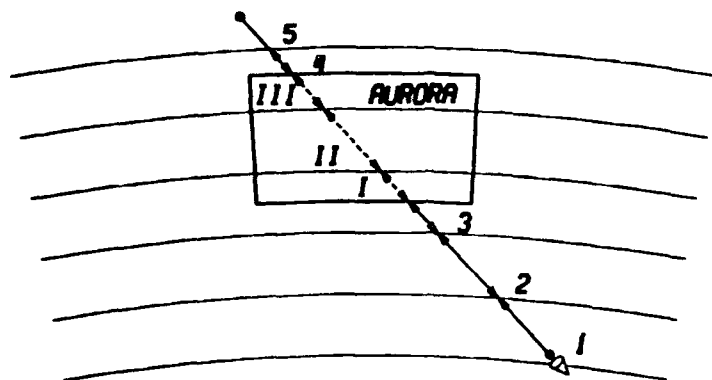


Figure 7. Layering Schematic with Local Auroral Region.

Usually the LOS of the radiance calculation only intersects a local region twice. A typical path is illustrated in Fig. 7. However four intersections are possible for a limb path whose minimum altitude is just slightly less than the lower region boundary. This arises because of earth curvature effects. For example, a limb path at 89 km combined with a lower region boundary of 90 km will have four intersections when the horizontal extent of the region is several hundred kilometers to each side of a long tangent path.

2.8 Atmospheric Spatial Structures

Natural backgrounds are non-uniform in both space and time and are subject to changes due to geophysical conditions such as latitude, magnetic activity, and localized dynamic effects. Other spatio-temporal non-uniformities can be attributed to factors like aurora, eddy diffusion, winds or large scale circulations, tides, solar wind, and gravity waves. Structured features in the upper atmosphere can be divided into three general classes:²¹

- long-term variations of the quiescent atmosphere,
- short-term, wave-like fluid responses to forces acting on the atmosphere, and
- variations due to energy deposition from the magnetospheric particles and fields.

Short-term variations are the primary sources of "clutter" for systems applications, that is, spatial and/or temporal fluctuations in atmospheric radiance. Long-term variations are global effects which describe average properties of the atmosphere over distances larger than those related to an observer's FOV or LOS. One major manifestation of energy deposition is, of course, auroral activity. Scales associated with some typical atmospheric structures are given in Table 1.

Table 1. Atmospheric Structure Scales.

• LONG-TERM VARIATIONS	
horizontal scale	- 100 km
vertical scale	- scale height $H \approx 6$ km
temporal scale	- 1 hr
occurrence	seasonal, solar activity, etc.
• SHORT-TERM TURBULENCE	
horizontal scale	$100 \text{ m} < \lambda < 100 \text{ km}$
vertical scale	$200 \text{ m} < \lambda < 2 H$
temporal scale	- 1 s
fractional perturbation	$\frac{\Delta \rho}{\rho}, \frac{\Delta T}{T} \approx 10\%$
form of PSD	$\frac{\Delta \rho}{\rho} \propto k^{-n} \quad n \in [1, 2]$
occurrence	random
• SHORT-TERM GRAVITY WAVES	
horizontal scale	$100 \text{ m} < \lambda < 1000 \text{ km}$
vertical scale	$0.5 H < \lambda < 3 H$
temporal scale	- 5 min to 3 hr
fractional perturbation	$\frac{\Delta \rho}{\rho} \approx 1-10\%$
occurrence	random
• THERMAL TIDES	
vertical scale	- 50 km
temporal scale	- 12 hr
fractional perturbation	$\frac{\Delta \rho}{\rho} \approx 20\%$
occurrence	regularly, due to solar heating of atmosphere

There is a severe lack of good data on atmospheric spatial structures in the 50-300 km regime. Several approaches for using the basic science contained in the present SHARC chemistry and radiation transport modules as the basis for a systematic phenomenological approach to clutter were studied. Structures with large-scale variations could be adequately handled for many applications by expanding the number of default atmospheres to include latitudinal, diurnal, seasonal, geomagnetic, and solar-activity effects. These profiles could be linked to an available model like MSIS,²² that has been upgraded to include profiles for important IR molecules like CO₂, NO, and O₃. Small-scale fluctuations could be modeled with a causal approach in which spatial structures in radiance are calculated from spatial variations in basic atmospheric parameters like density, composition and temperature. These structures can be introduced into SHARC by defining different local atmospheric regions, each having its own density and temperature profile.

This approach to small-scale clutter, which we call geometric, assumes that radiance structures result from atmospheric regions with different temperatures and species densities. The region profiles are selected, within physical limits, to reproduce observed radiances and/or incorporate other, related measurements. The utility of the approach is realized when systems studies address issues like filter bandpasses and multiple LOS's. Signal and clutter intensities can be calculated for different bandpasses that include the same radiators. Non-linear effects like those due to opaque spectral lines (e.g., clutter at 60 km is not relevant for limb viewing at 4.25 μ m) are naturally included. Atmospheric effects on moving and/or multiple targets can be calculated as different sensor LOS's will traverse different parts of the various atmospheric regions.

The large-scale variations include diurnal and other latitude/longitude effects, as well as correlations with more global parameters such as solar and geomagnetic activity. Model atmospheres such as MSIS,²² and Jacchia,²³ or Kenesha²⁴ empirically relate temperature, density, and major species concentrations to geophysical parameters, geographic location and universal time. Lower altitudes and

important IR species like CO_2 , O_3 , and NO would have to be added. Their densities could be inferred from the major species and temperature profiles using photochemical or empirical models. For example, O_3 concentrations above 90 km may be computed from the major species via known chemical reactions.^{3,25,26} MSIS provides profiles for atomic O , which in turn directly effects O_3 (see Section 4). Diurnal effects are obtained by including photochemical reactions in the chemical kinetics. The CO_2 profile depends more on transport than chemistry; assuming it remains uniformly mixed, its variability can be estimated by scaling to the MSIS profiles for Ar .

Short-term, wave-like responses of the atmosphere can be considered as localized heating events superimposed on the smooth diffusive profiles of the long-term variations. These structures have a wide range of scale sizes and amplitudes and are characterized by irregular features resulting from the dissipative breakdown of waves into turbulent eddies. Their principal sources are:²⁷

- turbulence or random fluctuations in the velocity and density which serve to mix the atmosphere,
- gravity wave structures that originate in troposphere, propagate through the stratosphere and ionosphere into the upper atmosphere,
- diurnal and semidiurnal tidal motions that propagate from the upper atmosphere into the middle atmosphere, and
- winds and circulation.

All of these phenomena are closely related. For example, gravity waves are associated with irregular wind components around the mesopause (70 to 120 km); thermospheric winds are the result of thermally created tidal waves; and wind shears may be a primary turbulence source. Geostrophic wind and tidal motion would be considered as part of the average background because their spatial and temporal scales are larger than any LOS path.

Most atmospheric flows are turbulent and occur on length and time scales that range from several thousand kilometers to sub millimeter and years to milliseconds, respectively. Turbulence cannot maintain itself indefinitely, so it must obtain energy from its environment. Turbulence

mixes atmosphere species and opposes gravity which tends to separate species vertically according to their molecular masses.

If not overwhelmed by convection, buoyant forces tend to restore displaced parcels of air from vertical displacements. The air parcel tends to oscillate around its undisturbed position at a frequency known as the Brunt-Vaisala frequency. Typical periods are in the vicinity of five minutes. Pressure waves generated with larger frequencies propagate as sound waves, and those with smaller frequencies propagate as internal gravity waves. These waves are excited near the earth's surface, probably in wind systems, and the energy flow is upward, reaching well into the ionosphere. Their amplitudes increase with altitude and above 60 km become so large that they dominate the wind profiles. Above about 100 km, dissipative mechanisms like viscosity, thermal conductivity, and eddy transport of heat and momentum break up these waves which, in turn, provide an energy source for the upper atmosphere. These phenomena have been incorporated into Global Climatic Models (GCM) by parameterizing gravity wave drag and diffusion.²⁸⁻³⁴

Atmospheric tides are internal gravity waves of particular frequencies. Tidal phenomena usually imply gravitational attraction by the moon or sun, but it can also refer to waves caused by solar heating. Barometric pressures in the tropical latitudes normally have two maxima and two minima per day with a period of 12 hours. At higher latitudes the amplitudes are smaller and are frequently dominated by noise from passing weather systems. Tidal wind patterns in the upper atmosphere also generate ionospheric electrical currents, which, in turn, produce diurnal variations in the geomagnetic field. These effects are included in some GCM's,^{27,31,35,36} and an initial approach for SHARC could use different profiles with its multiple regions.

Small-scale fluctuations in the SHARC local-regions model must be determined initially from field data. Fluctuations in atmospheric density, composition and temperature provide the basis for calculating the resultant IR clutter. They can either be measured or obtained from some first-principles model (for example, one for gravity waves). SHARC would calculate the excited state chemistry within each regions and then the LOS radiances for arbitrary views and spectral bandpasses. Good

agreement with observed radiance data would demonstrate that chosen power spectral density functions (PSD) for atmospheric composition are consistent with the data, but by no means will they form a unique set. These PSD's then provide the basis for predicting radiances for other scenarios. As an example of this non-uniqueness, consider clutter in the NO band which might be due to fluctuations in [NO], [O], or temperature. If these fluctuations are in [O] or temperature, the CO₂(ν₂) band, for example, would likewise be affected (or correlated); if the fluctuations are mainly due to [NO], it would be uncorrelated. The crucial point is that the chemistry, radiation transport, and multiple region capability in SHARC provides a framework for studying sources of and models for IR clutter.

3. SHARC AURORAL MODEL

3.1 Model Description

The scientific approach used in SHARC auroral model is substantially based on the Geophysics Laboratory Infrared Spectral Radiance Code for the Auroral Thermosphere (AARC).¹⁴ The calculational procedure for the AURORA module is shown schematically in Fig. 8. The primary function of this module is to perform a time dependent chemical kinetics calculation to determine auroral species number densities as a function of altitude. For $\text{CO}_2(\nu_3)$, the chemical kinetics are coupled to a simplified radiative transfer scheme³⁷ to obtain the excited state number densities. The Gear method for stiff differential equations is used to perform the integration. This package was supplied as part of the Sandia CHEMKIN code,¹⁵ and thus it has been thoroughly tested. In addition to the specification of the auroral electron spectra, the AURORA module uses the input from the "linking" file (species identification, stoichiometric coefficients, and rate constant parameters) to construct the time dependent production rates for the auroral species. After completing the numerical integration, the AURORA module returns the vibrationally excited number densities to the SHARC main program. The ambient and auroral populations are then stored for

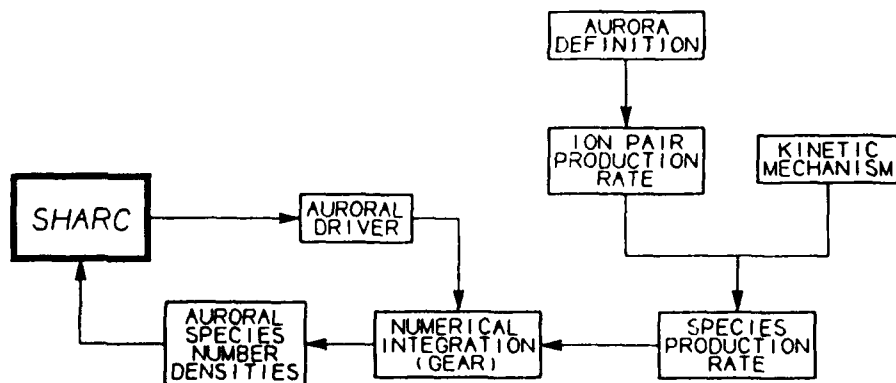


Figure 8. Major Components of the Auroral Model.

each layer along the LOS. SPCRAD uses those populations to calculate the path radiance and transmittance.

The remainder of this section contains a general discussion of the approach used in the auroral model, a comparison of SHARC with the AARC model, and an illustrative auroral calculation.

Calculating the radiance for a LOS through an aurora requires the following:

- definition of the strength of the aurora,
- specification of the chemical kinetics mechanism for the selected emitter, including primary and secondary electron processes, and
- identification of the radiative transition and the associated spectroscopic data.

In addition to the above information, a description of the ambient atmosphere must also be included. Each of the above topics are described in more detail in the following subsections.

3.1.1 Aurora Definition

The primary electron energy deposition model included in SHARC is based upon work by Grün, Rees, and Strickland.³⁸⁻⁴⁰ The model has been described in detail in the AARC user's manual.¹⁴ Routines describing the energy deposition have been written for SHARC. These routines were taken from the AARC model, and modified to be consistent with the SHARC structure.

As an example of the primary electron energy deposition model, the total ion pair production rate for a class III⁺ aurora is shown in Fig. 9. The parameters for generating this ion pair production rate are contained in the AURORA module as part of the data base. Of course, the user may choose to define his/her own aurora by overriding the default inputs.

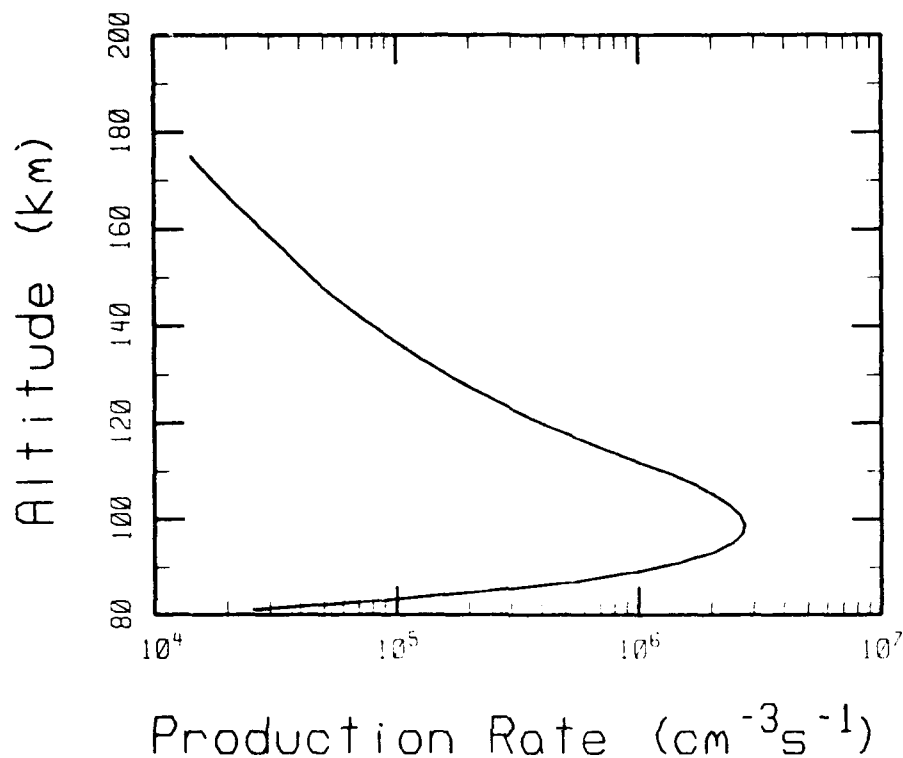


Figure 9. Ion Pair Production Rate for a Class III⁺ Aurora.

3.1.2 Auroral Kinetics

The auroral kinetic model solves the time/energy dependent rate equations to calculate the secondary electron distributions and reactive/energy transfer processes, and the subsequent enhancement to various CO₂, NO, and NO⁺ vibrational states. The chemical reactions and energy transfer processes resulting from primary electron deposition in the atmosphere have been described in some detail in the AARC¹⁴ and SHARC² manuals. The following subsections briefly describe the auroral kinetic mechanisms employed by SHARC, and present comparisons of SHARC and AARC volume emission rates for the auroral emitters.

Secondary Electron Kinetics

Since IR emissions resulting from direct electron impact excitation, as well as recombination reactions, depend on the low energy secondary electron spectra, it is important that the histogram treatment used in SHARC retain the major features of the secondary electron spectra. Secondary electrons are formed via collisional ionization of $M (= N_2, O_2, \text{ or } O)$



From an assumed initial secondary electron energy distribution, the secondary electrons undergo further collisions with major species



and



which result in the electronic or vibrational relaxation of the secondary electron spectra.

Given the ion pair production rate as a function of altitude, ionization efficiencies, electronic and vibrational excitation rate constants, the secondary electron distribution resulting from ionization of the major atmospheric constituents can be calculated. An example of a secondary distribution calculated as an input to the AURORA module is shown in Fig. 10. The most interesting feature of this distribution is the large dip around 3 eV, which is due to vibrational excitation of N_2 by the secondary electrons. The features and altitude dependence of secondary electron distributions have been discussed in great detail elsewhere.⁴¹

NO 5.3 and 2.7 μm

Nitric oxide in the upper atmosphere both during quiescent and disturbed conditions forms a major source of infrared radiation⁴² in the

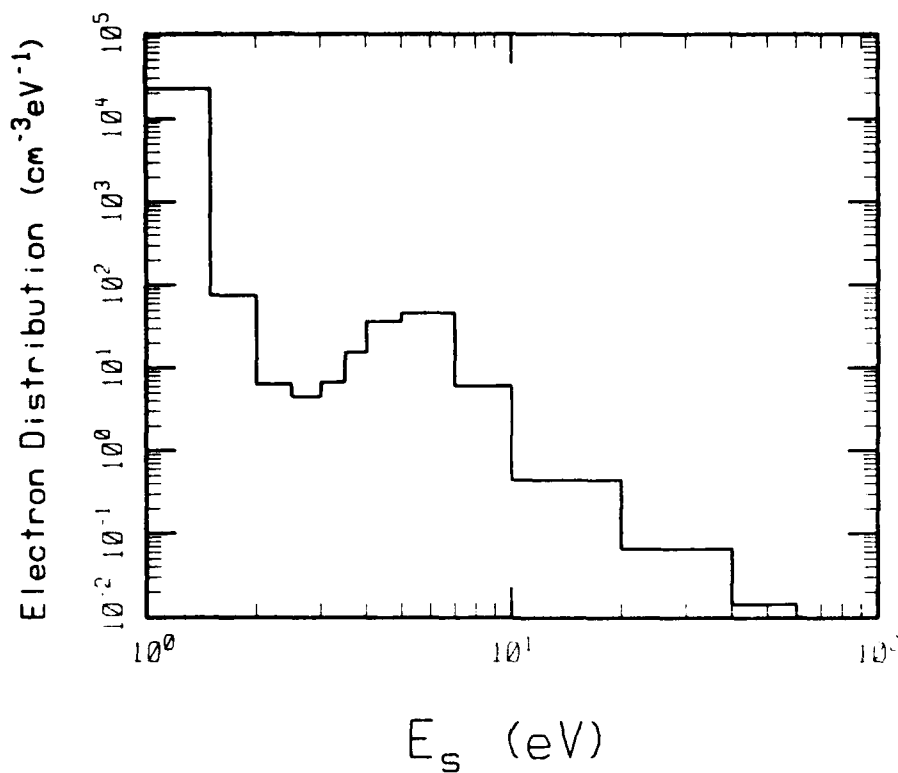


Figure 10. Steady State Secondary Electron Distribution at an Altitude of 100 km for a Class III⁺ Aurora.

2.7 to 3.3 μm and the 5.3 to 6 μm bands. When electrons interact with the ambient atmosphere, ionization forms odd nitrogen in the form of $\text{N}(^2\text{P})$, $\text{N}(^2\text{D})$, and $\text{N}(^4\text{S})$. Collisions between these species and O_2 create NO in the upper atmosphere. This production rate is in turn found to be highly dependent on the ratio of $\text{N}(^2\text{D})$ to $\text{N}(^4\text{S})$ formed in the interaction of electrons and N_2 .

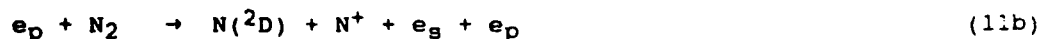
Nitric Oxide is primarily produced by the reaction of $\text{N}(^2\text{D})$ with O_2



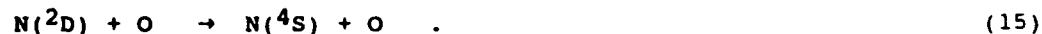
and destroyed by reaction with ground state $\text{N}(^4\text{S})$



The dominant production mechanisms for excited nitrogen atoms are: direct dissociation of N_2 by the primary electrons produced in the electron beam (11), ion recombination reactions with secondary electrons (12), and charge transfer reactions of the primary ionic products (13)



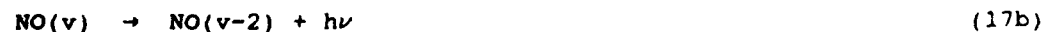
Nitrogen atoms are also subject to quenching by other species which compete with the reactions of Eqs. (9) and (10) in the production and destruction of NO



The vibrationally hot $NO(v)$ can be quenched by O_2



Similarly, the upper levels can emit radiation, and thus cascade down the vibrational ladder.



Radiative decay rates from the high v states by $\Delta v=2$ are comparable to that for $\Delta v=1$.

Laboratory and field measurement programs have indicated the existence of extremely high rotational excitation (rotational temperatures on the order of 10000 K) for vibrational states up to $v=5$. There is some evidence that the mechanism for the formation of this rotationally hot NO is from the reaction



although this process is not currently treated in SHARC.

CO₂ 4.3 μ m

There are two ways to excite CO₂ efficiently in an aurorally excited atmosphere: direct electron excitation, and the transfer of energy from vibrationally excited N₂ to CO₂. Different models of N₂ excitation due to secondaries have as much as a factor of three disagreement. Assumptions differ on the precise shape of the secondary electron energy spectrum and mechanisms assumed for thermalizing these electrons.

In order to calculate the intensities of the prompt and delayed emissions, several assumptions are made. Important parameters are the ion pair production rate and the aurora duration. The total amount of energy put into the atmosphere determines the amount of energy stored in N₂, while the ion pair production rate determines the number of secondary electrons present to transfer energy directly to CO₂. These reactions are represented in SHARC by:



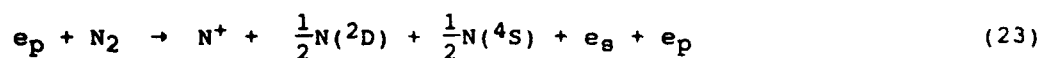
By binning the secondary electrons e_s and e'_s , both the energy spectra and the $N_2(v)$ are simultaneously treated. The number of vibrationally hot N_2 molecules created in this way was found to vary with altitude and dose.

The mechanisms for the prompt emission at $4.3 \mu m$ are given by



NO^+ $4.3 \mu m$

NO^+ emission in the $4.3 \mu m$ region has not been unambiguously identified in the region to the red of $CO_2 \nu_3$ due to the lack of high-sensitivity, high resolution spectral measurements. Previous models have assumed the primary source of NO^+ formation is from the ion molecule reaction of N^+ with O_2 . The primary reaction set used in these calculations is as follows:



The formation of NO^+ competes with the charge exchange reaction,



The vibrationally excited $NO^+(v)$ can be quenched by N_2



as well as emit radiation, and thus cascade down the vibrational ladder



3.1.3 Radiative Transfer Model for CO₂(4.3 μm)

The emission from NO and NO⁺ is both optically thin and prompt. Thus, coupling of the radiative transfer and collisional processes, is not required, and the solutions to the mechanisms given previously suffice in the calculations. However, for CO₂(4.3 μm), emission below 100 km is both optically thick and delayed due to the N₂-CO₂(ν₃) vibrational energy transfer. Thus, to treat the radiative transfer correctly requires the coupling of the CO₂ time-dependent chemical kinetics with the radiative transfer scheme. Unfortunately, such a treatment in SHARC is prohibitively time consuming and is not possible at this time.

Kumer³⁷ has presented a model in which he has shown how to uncouple the radiative transport from the time-dependent kinetic processes, and which he has termed the Q_w approximation. The approximation has also been discussed in some detail in the AARC report.¹⁴ In this approximation, the chemical kinetic equation for CO₂ becomes

$$\begin{aligned} \frac{d}{dt}[\text{CO}_2(001)]_i &= k_e[e_s]_i[\text{CO}_2(000)]_i + k_1[\text{N}_2^*]_i[\text{CO}_2(000)]_i \\ &- k_1'[\text{N}_2]_i[\text{CO}_2(001)]_i - k_M[M]_i[\text{CO}_2(001)]_i \\ &- (1 - \sum_j w_{ji})A_{4.3}[\text{CO}_2(001)]_i + k_a[\text{CO}_2(000)]_i \end{aligned} \quad (28)$$

where the first four terms in Eq. (28) result from the direct secondary electron excitation of CO₂, the vibrational energy transfer of CO₂ with N₂^{*}, and the quenching of CO₂(001) by the atmosphere. The last two terms represent the effects of radiation transport on the chemical kinetics. The first effect (given by the fifth term) is simply a modification of the Einstein coefficient, A_{4.3}, due to the fact that not all photons emitted from the ith layer escape the atmosphere. The second effect is included as an external source, represented by the rate constant k_a, and accounts for the excitation of CO₂ in the ith layer by radiation emitted from all other layers.

An analogous rate equation for the excitation of N_2 is

$$\begin{aligned} \frac{d}{dt}[N_2^*]_i &= k_e[e_s]_i[N_2]_i + k_1'[N_2]_i[CO_2(001)]_i \\ &\quad - k_1[N_2^*]_i[CO_2(000)]_i + k_2'[N_2]_i[CO_2(011)]_i \\ &\quad - k_2[N_2^*]_i[CO_2(010)]_i - k_M[M]_i[N_2^*]_i \\ &\quad + k_{3e}[N(^4S)]_i[NO]_i + k_{4e}[O(^1D)]_i[N_2]_i \end{aligned} \quad (29)$$

where the first six terms in Eq. (29) result from the direct secondary electron excitation of N_2 , the vibrational energy transfer of $CO_2(001)$ and $CO_2(011)$ with N_2 , and the quenching of N_2^* by the atmosphere. The last two terms in Eq. (29) represent the effective rate of formation of N_2^* from aurorally produced species. The relative importance of these terms in producing N_2^* is discussed in the next section.

3.2 Comparison of SHARC with AARC

This section presents a brief validation of the chemical kinetics mechanisms used by SHARC by comparing the efficiency of producing photons per ion pair predicted by SHARC with those from AARC.¹⁴ The intent of this section is not to discuss the particular features of the efficiencies since this has been done in some detail in the AARC report. Efficiencies are computed by SHARC for $NO(\Delta v=1)$, $N_2(v=1)$, and $NO^+(\Delta v=1)$ assuming an IBC III aurora and a standard atmosphere which is included with SHARC.

The altitude and time dependence of the $NO(\Delta v=1)$ photons/ion pair predicted by SHARC is compared with the steady state AARC prediction in Fig. 11. At altitudes less than 115 km, SHARC indicates that the efficiency is indeed time independent and in excellent agreement with the AARC calculation. However, at altitudes greater than 115 km, the number of photons produced per ion pair shows a significant time dependence and is almost a factor of 2 greater than the AARC efficiency. This effect results almost entirely from the collisional excitation of ground state NO (which is continually produced by the aurora) by O atoms. However, in AARC, an initial, time independent NO number density

profile is assumed, and the steady state NO vibrational populations are then normalized to the input profile. Although there is a sizeable difference between SHARC and AARC at high altitudes, the effect of this difference is relatively unimportant for most LOS radiances because emissions from the ambient atmosphere are dominant at these altitudes.

One significant difference between SHARC and AARC is the rate constant assumed for the process



which results in almost a factor of two difference in the predicted efficiencies as shown in Fig. 12. The SHARC value for Eq. (11) is based upon work done in the GL EXCEDE program and is more than a factor of two less than the value assumed by AARC.

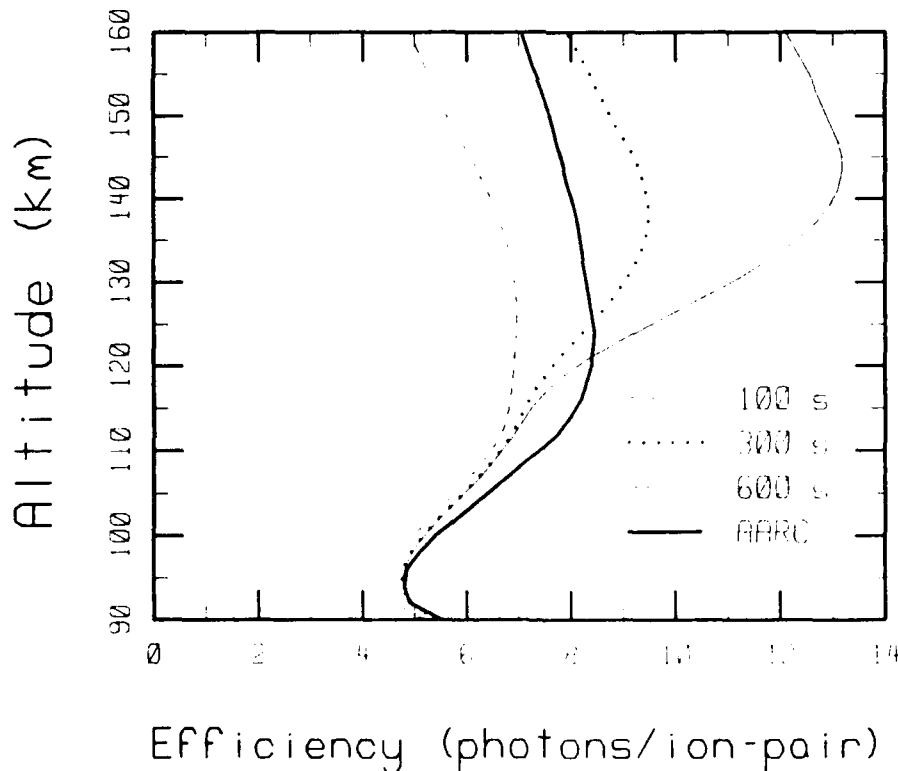


Figure 11. Comparison of the SHARC NO($\Delta v=1$) Time-Dependent Photons/Ion Pair with the AARC Efficiency.

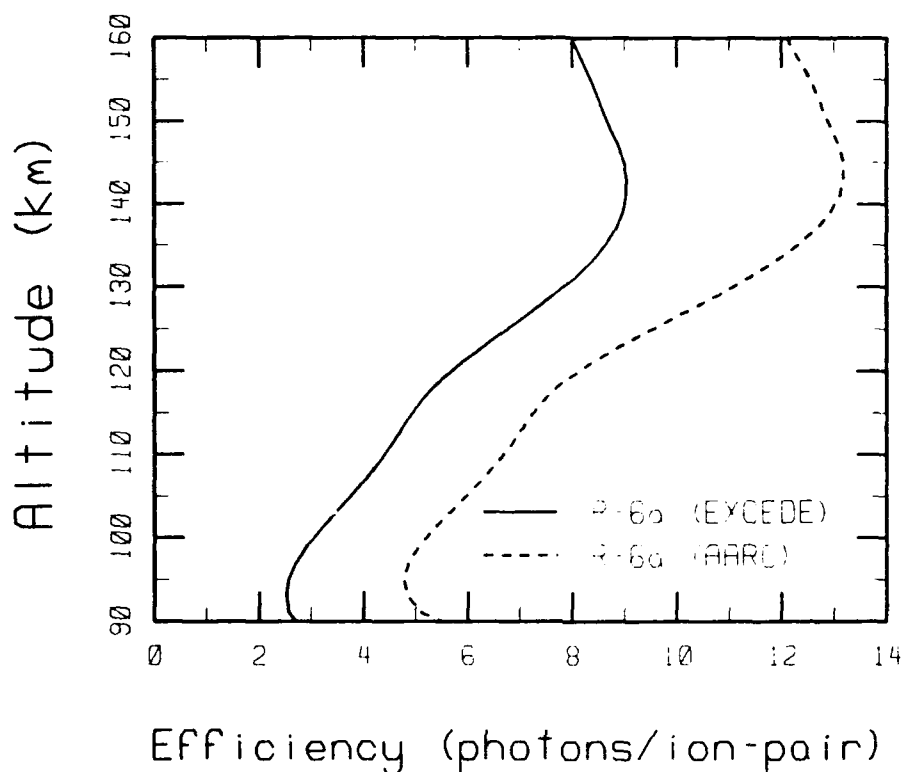


Figure 12. Comparison of the SHARC $\text{NO}(\Delta v=1)$ Predictions of Photon/Ion Pair Efficiencies Using the EXCEDE and AARC Rate Constants for Eq. (11).

The dominant mechanism for the CO_2 $4.3 \mu\text{m}$ emission is the transfer of energy from vibrationally excited N_2 to CO_2 . The most important processes for formation of N_2^* are the direct secondary electron excitation of N_2 , the reaction of N atoms with NO , and electronic to vibrational energy transfer between $\text{O}(^1\text{D})$ and N_2 (see Eqs. (19)). The altitude dependence of the SHARC efficiency due to each of these processes is shown in Fig. 13. For the assumed mechanisms and rate constants, it can be seen that the direct electron excitation of N_2 is of comparable importance to the chemical production mechanisms. Furthermore, there is only a slight altitude dependence to the efficiencies. The AARC prediction of the N_2^* efficiencies for the same processes are shown in Fig. 14. For the chemical mechanisms (19b and 19c), the agreement between SHARC and AARC is no worse than 30%,

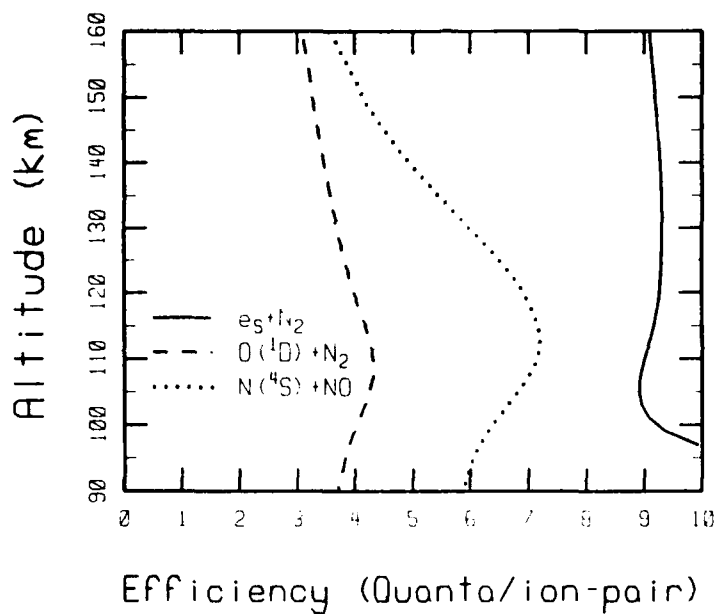


Figure 13. SHARC Prediction of the $N_2(v)$ Efficiencies (Quanta/Ion Pair) for Several Production Mechanisms.

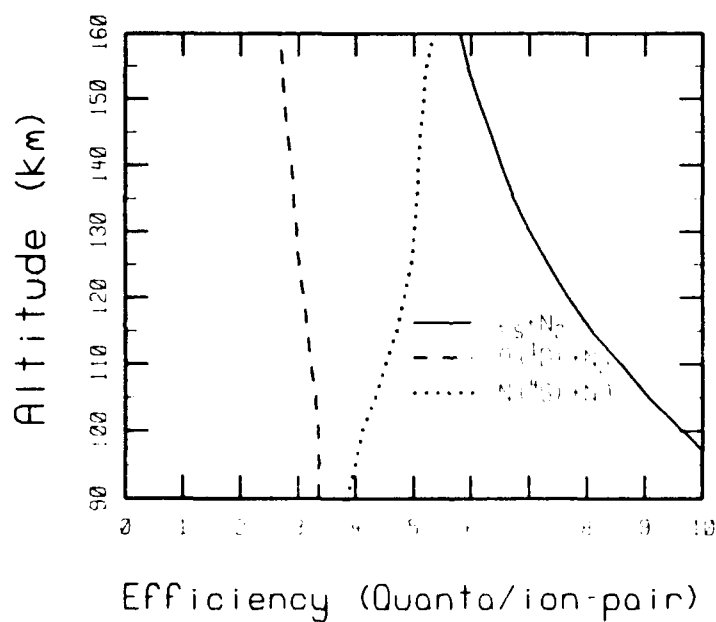


Figure 14. AARC Prediction of the $N_2(v)$ Efficiencies (Quanta/Ion Pair) for Several Production Mechanisms.

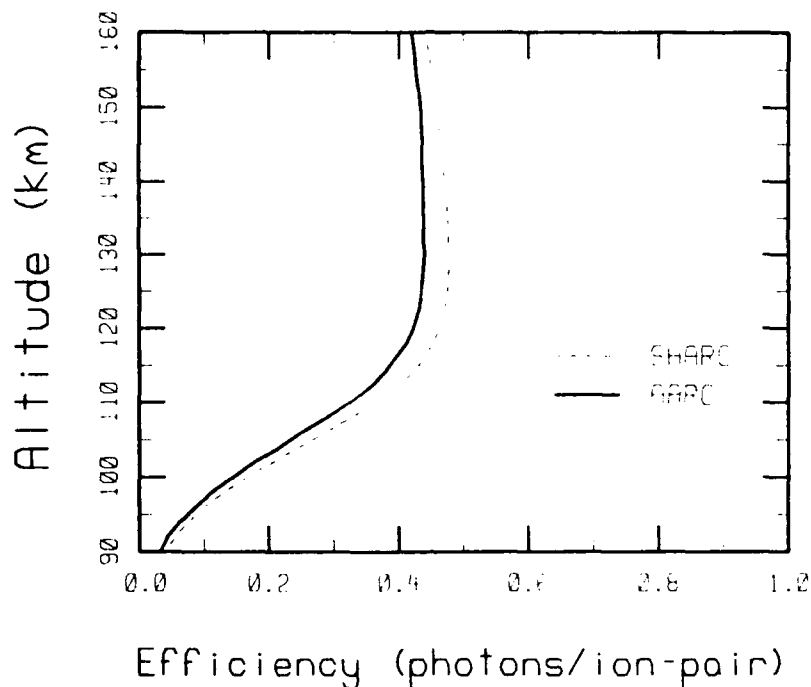


Figure 15. Comparison of the SHARC and AARC $\text{NO}^+(\Delta v=1)$ Efficiencies (Photons/Ion Pair).

although the detailed profile of the efficiency due to $\text{N}(^4\text{S})+\text{NO}$ is quite different due to the manner in which the NO profile is generated during an aurora. The most substantial difference between SHARC and AARC is the secondary electron excitation efficiency at altitudes greater than 110 km, which is not understood at the present time.

The final comparison of SHARC and AARC efficiencies is shown in Fig. 15 for $\text{NO}^+(\Delta v=1)$. The agreement between SHARC and AARC is excellent over the entire altitude regime.

3.3 Illustrative Calculation

As an example of the auroral enhancement of NO $5.3 \mu\text{m}$ radiation, a calculation has been performed for an IBC II aurora, appropriate to the FWI¹⁹ experiment. The calculation uses an augmented HITRAN data file,¹⁴ which has been expanded to include lines for high NO vibrational states and NO^+ .

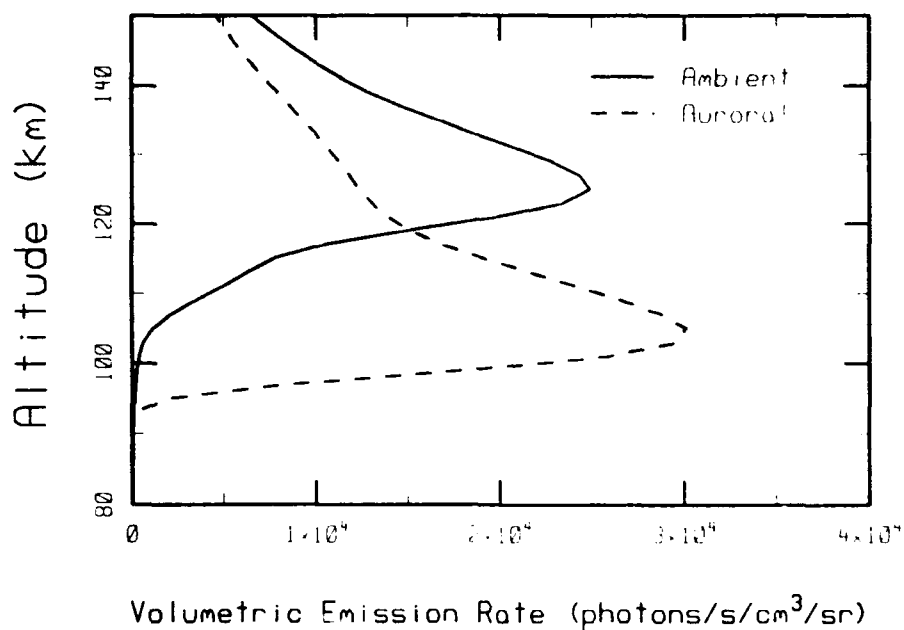


Figure 16. SHARC Prediction of Ambient and Auroral IBC II Altitude Dependent Volumetric Emission Rates for $\text{NO}(\Delta v=1)$.

The relative contributions of the ambient and auroral components to the volumetric emission rate as a function of altitude are illustrated in Fig. 16 for $\text{NO}(\Delta v=1)$. The ambient emission increases with altitude until approximately 125 km and then begins to decrease. This behavior is due to $\text{O}+\text{NO}(v=0)$ collisional excitation, which depends on the O and NO number density profiles and the ambient temperature (see Eq. 5). The altitude dependence of the auroral emission is dictated by the $\text{N}(\text{2D})$ altitude profile, which in turn is determined by the ion pair production rate (see Fig. 9).

A comparison of a SHARC auroral calculation to FWI data¹⁹ is shown in Fig. 17. The data were taken from a sounding rocket launched from Poker Flat, Alaska in April 1973 under auroral conditions. These measurements provided the first high spectral resolution IR data for an aurorally disturbed atmosphere. Ground measurements prior to launch indicated an auroral strength of 50 kiloRayleighs, but it had weakened to less than 12 kR by launch time. The spectral data have a

resolution of about 1 cm^{-1} . The model calculations are for a Class II aurora of 10 kR. Although the calculations fall about a factor of four below the data, the results are quite promising for an ab initio calculation that starts with electron dosing of the ambient atmosphere. During auroral events, the NO and NO+ populations increase significantly, and we ascribe the difference to strong predosing and population enhancement prior to the measurements, which are not modeled in the present version of SHARC. It is also possible that the uncertainty in the rate of $\text{N}(^2\text{D})$ creation from Eq. (11a) as shown in Fig. 12 is responsible for part of the discrepancy. Further detailed analysis of the full data set is required to clarify this point.

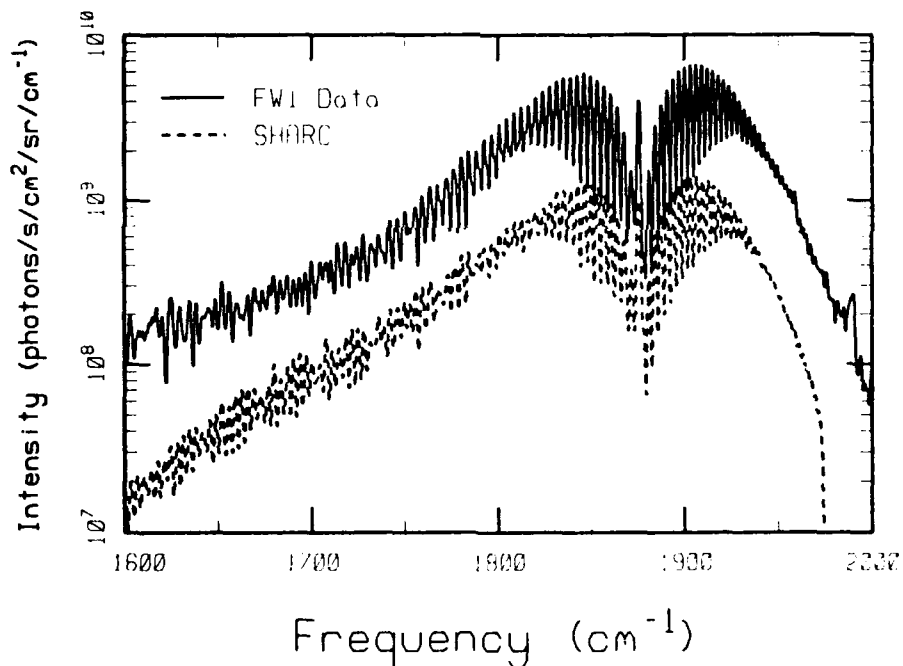


Figure 17. Comparison of the SHARC Spectral Radiance with FWI Data for a Near Zenith Line-of-Sight.

4. ANALYSIS OF SPIRIT 1 DATA

The Spectral Infrared Interferometric Telescope (SPIRIT 1) experiment, launched in 1986 from Poker Flat, Alaska, generated a large and valuable body of earth limb LWIR spectral data during auroral conditions.¹⁸ Emissions were observed from CO₂ ν_2 , the NO fundamental, and the O₃ ν_3 fundamental and hot bands. These data were analyzed by SSI as part of an overall effort to improve our understanding of LWIR backgrounds and to validate model calculations.

Data analysis under this effort included data compilation and selection, identification of background contamination sources, contamination subtraction, spectral modeling using atmospheric radiation codes, limb inversions using a specially-developed least-squares method, temperature profile determinations using a novel moment method, and density profile determinations using photochemical models. In the course of this work, several upgrades to the raw data reduction scheme developed by Boston College were also implemented. These included the determination and application of wavelength response curves and scale factors for absolute radiance calibration, and tangent height corrections based on data from the on-board horizon and star sensors. The results of the SPIRIT 1 data analysis program are summarized in four publications, which are described briefly in the following subsections.

A general conclusion to be drawn from the SPIRIT 1 observations is that the LWIR limb radiances as well as the average densities of the pertinent species (O, O₃, CO₂, and NO) in this experiment were typically within a factor of two of current non-auroral model predictions. Features such as NO hot bands that are known to arise from auroral excitation channels were not observed in SPIRIT 1 due to their weakness relative to the quiescent atmospheric limb background, or due to instrumental effects such as the presence of strong CO₂ ν_2 radiation or background contamination. However, evidence may exist for more subtle effects, such as O and H atom depletion, associated with atmospheric disturbances. It is suggested that future auroral observation experiments utilize nadir- or slant-viewing rather than limb-viewing

geometries to minimize off-axis contamination as well as the normal atmospheric background radiation.

An important result from SPIRIT 1 is the acquisition of high-quality, well-resolved ozone hot band spectra in the 10-13 μm atmospheric window. Analysis of these spectra have resulted in new hot band center assignments, as well as a quantification of the relationship between the hot band intensity and the O-atom recombination rate.

4.1 9-12 μm Ozone (ν_3) Emission

Spectra of ozone ν_3 emission observed in the auroral, nighttime atmosphere during the SPIRIT 1 experiment were analyzed.¹⁸ The well resolved hot-band spectra reveal spectral structure not previously observable, and provide a critical test of ozone radiance models. The limb radiance profile is in good agreement with previous data below -95 km, but above this altitude it falls off more rapidly. Results of this study include limb spectra, limb radiances and volumetric emissions in various band passes. Also a nighttime ozone profile was derived.

Examples of the ozone spectra are shown in Fig. 18. The (001)-(000) (cold) band appears as the strong double-peaked feature. The ν_3 hot bands, which arise from $\text{O} + \text{O}_2 + \text{M}$ recombination, appear as the tail to the red of the cold band.

Figure 19 compares ozone density profiles obtained from several different sources: a calculation based on the SPIRIT 1 cold band radiance profile with an estimated T_v ; the profile assumed for the HAIRM code;¹¹ and a photochemical model calculation with assumed O and H profiles. The factor-of-two consistency between these profiles up to altitudes of 100 km supports the claim that the essential physics and chemistry of ozone formation, destruction, and radiation at these altitudes are reasonably well understood. An improved analysis resulted in more accurate O, H and T_v profiles.⁴³

The ozone hot band spectrum is briefly discussed. The need to update the current hot band center frequencies in HAIRM and SHARC was noted, and a modified formula for ozone vibrational energy levels was proposed.⁴⁴

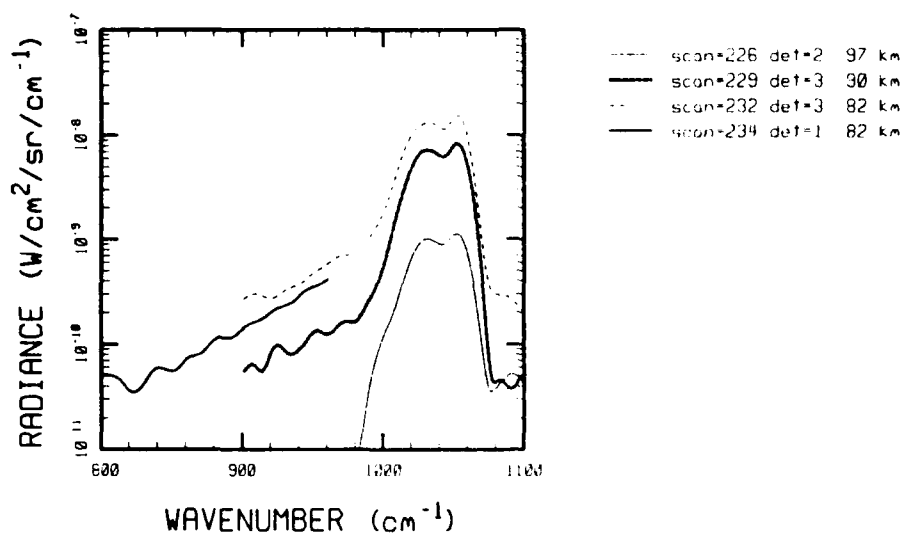


Figure 18. Ozone Limb Spectra from SPIRIT 1 with Kaiser-Bessel Apodization.

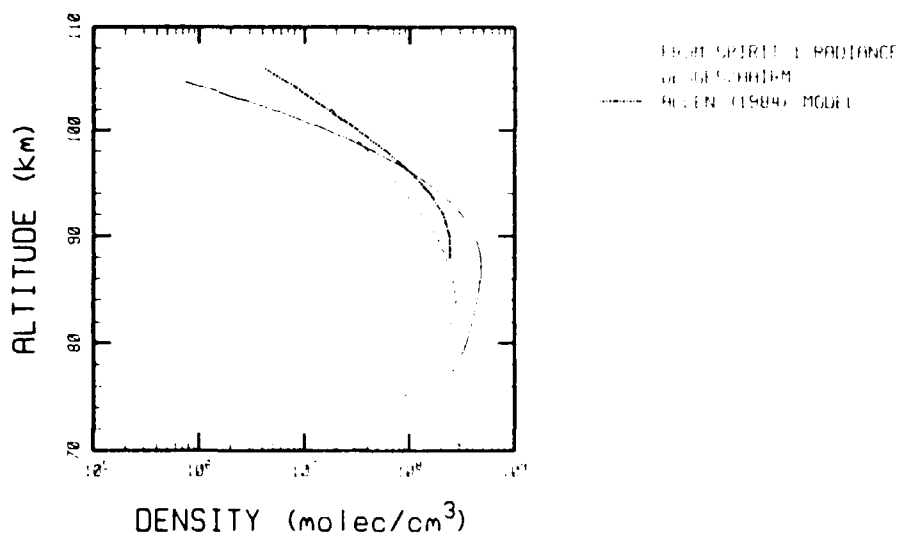


Figure 19. Comparison of Standard Nighttime Ozone Density Profiles with Profile Derived from SPIRIT 1 Data.

4.2 Identification of O₃ High Vibrational States

O₃ hot band chemiluminescence spectra obtained in SPIRIT 1 were analyzed in detail with the aid of laboratory data and vibrational energy and band contour predictions.⁴⁴ Band centers and energies for previously unreported vibrational states of ozone having up to seven quanta were derived. The assignments are supported by the predictions of an improved Darling-Dennison-type energy level formula which behaves realistically towards dissociation. Bands associated with bending as well as stretching excitation appear due to an accidental vibrational resonance and a non-mode-specific population distribution.

The band centers and vibrational energies derived from this analysis are summarized in Table 2. Eight bands whose isolated Q branches were observed in the SPIRIT 1 spectrum appear in the "Current" column; their centers are accurate to within -2 cm^{-1} or better.

A synthetic spectrum was generated by least-squares fitting to the observed spectrum using eight independent population components. The overall agreement between the synthetic and observed spectra (Fig. 20) is quite good, considering the approximations in the spectral model.

4.3 CO₂(ν_2) and NO($\Delta v=1$) Emissions

SPIRIT 1 spectral data for CO₂ ν_2 and NO 5.3 μm emissions were analyzed.⁴⁵ These data cover auroral intensities from several kR to over 100 kR at 391.4 nm, and tangent heights of ~ 70 -200 km. Volumetric emission and kinetic temperature profiles have been obtained using linear least-squares inversion procedures. The CO₂ ν_2 radiance profile is found to be similar to previous observations. The NO 5.3 μm emission is weaker than usual, which is ascribed mainly to a low thermospheric temperature. Auroral enhancement of NO hot bands was not observable with the available sensitivity.

Table 2. Energies & Band Centers for O₃ Vibrational States.

STATE	ENERGY (cm ⁻¹)			BAND CENTER (cm ⁻¹)		
	Calc.	Obs.	Current	Calc.	Obs.	Current
003	3045	3046±1 ^a	3046	987	987±3 ^b	988
004	3999		4000	954	952±3 ^b	954 ^c
005	4910 ^d			911 ^d		
	4918 ^e	4918±1 ^f	4919	919 ^e	916±3 ^b	919
311	4902 ^d					
	4894 ^e	4895±1 ^f	4894	895 ^{g,e}		894 ^g
006	5767	5761±10 ^h	5771	841 ^d		
				849 ^e		852
				873 ^{g,e}		877 ^g
102	3085	3084±1 ^a	3083	975	971±3 ^b	972
103	4025	4019±1 ^f	4020	940	939±3 ^b	937 ^c
104	4925		4926	900	904±3 ^b	906 ^c
105	5774		5778	849		852 ^c
013	3695	3697±1 ^a	3697	970		971
014	4631		4633	936		936
015	5519		5517	888		884 ^c
016	6342		6345	823		828 ^c
112	3743		3743	958		958
113	4663	4659±1 ^f	4660	920		917
114	5537		5536	874		876 ^c
115	6351		6353	814		817 ^c

^a Barbe, et al. (Ref. 46); absorption

^b Rawlins and Armstrong (Ref. 47); emission

^c Q branch identified in SPIRIT 1 spectrum

^d Excludes (311)-(005) resonance

^e Includes (311)-(005) resonance

^f Contour analysis of Damon et al. (Ref. 48) absorption spectrum

^g Crossover band

^h Imre (Ref. 49); Raman spectrum

Examples of the data appear in Figs. 21 thru 23. Figure 21 shows the CO₂ ν₂ radiance versus altitude, and Fig. 22 shows representative CO₂ spectra at different altitudes. The NO radiances appear in Fig. 23. Figure 24 shows the results of a determination of the mesospheric temperature profile from the NO band shape using a new method based on

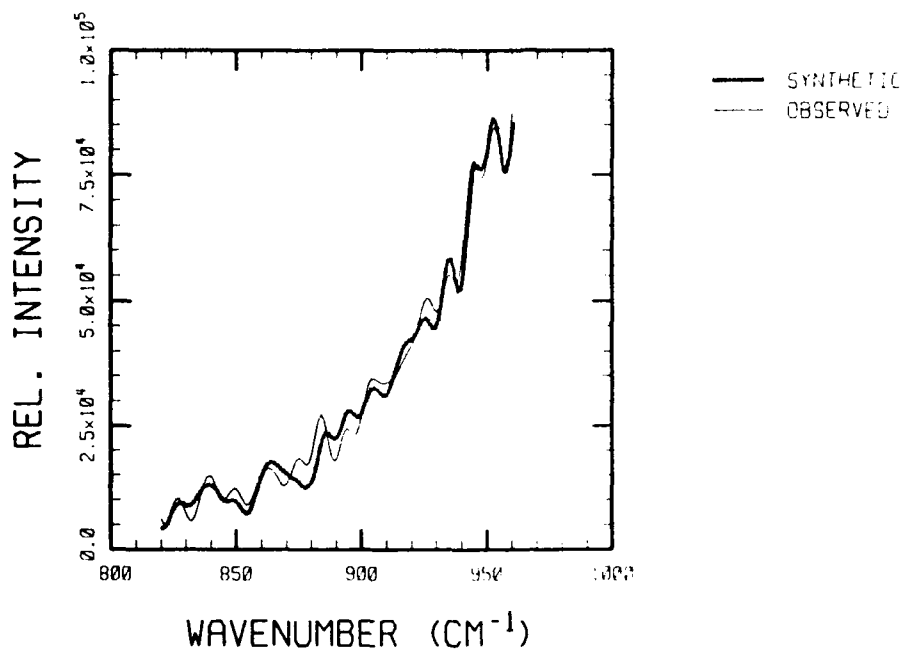


Figure 20. Comparison of Observed and Synthetic Unapodized Ozone Spectra.

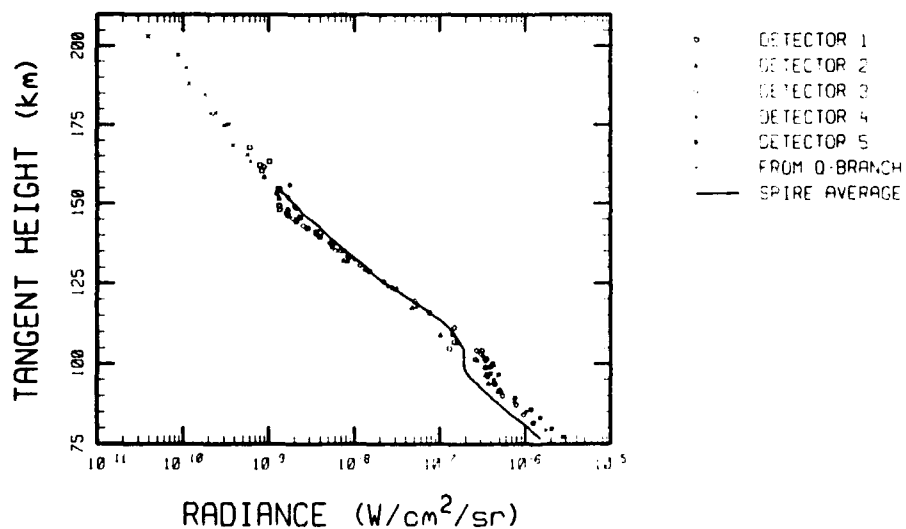


Figure 21. CO_2 ν_2 Limb Radiance Profile From SPIRIT 1, and Average of SPIRE Data.

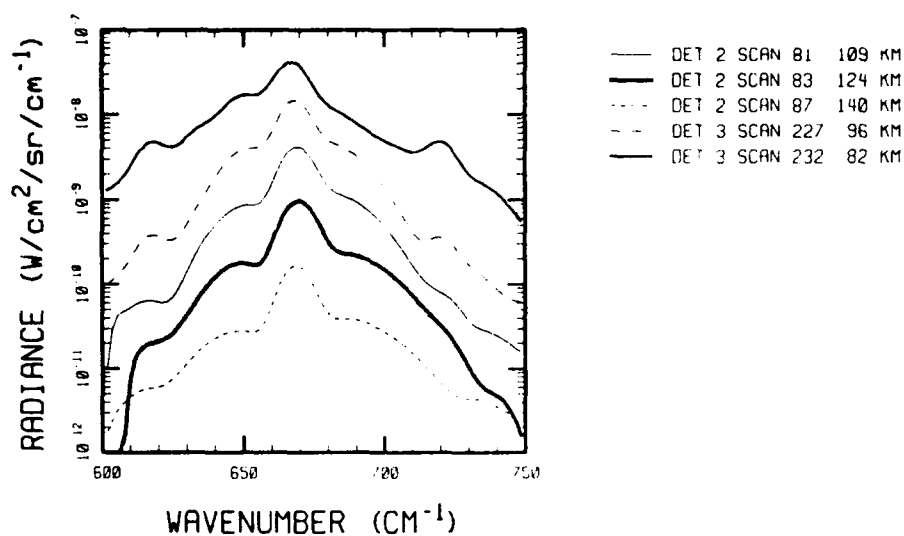


Figure 22. Typical CO₂ ν₂ Spectra at Various Tangent Heights with Kaiser-Bessel Apodization (11 cm⁻¹ Resolution).

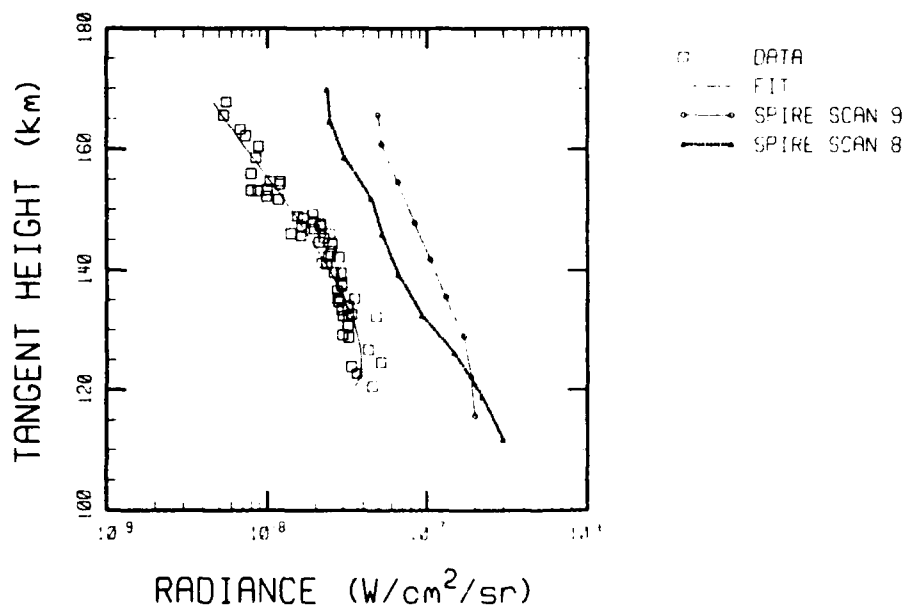


Figure 23. NO Δv=1 (5.3 μm) Limb Radiance Profile, Showing Second-Degree Fit and Full Limb-Corrected SPIRIT 1 Data. SPIRE Full Limb Data are also Plotted.

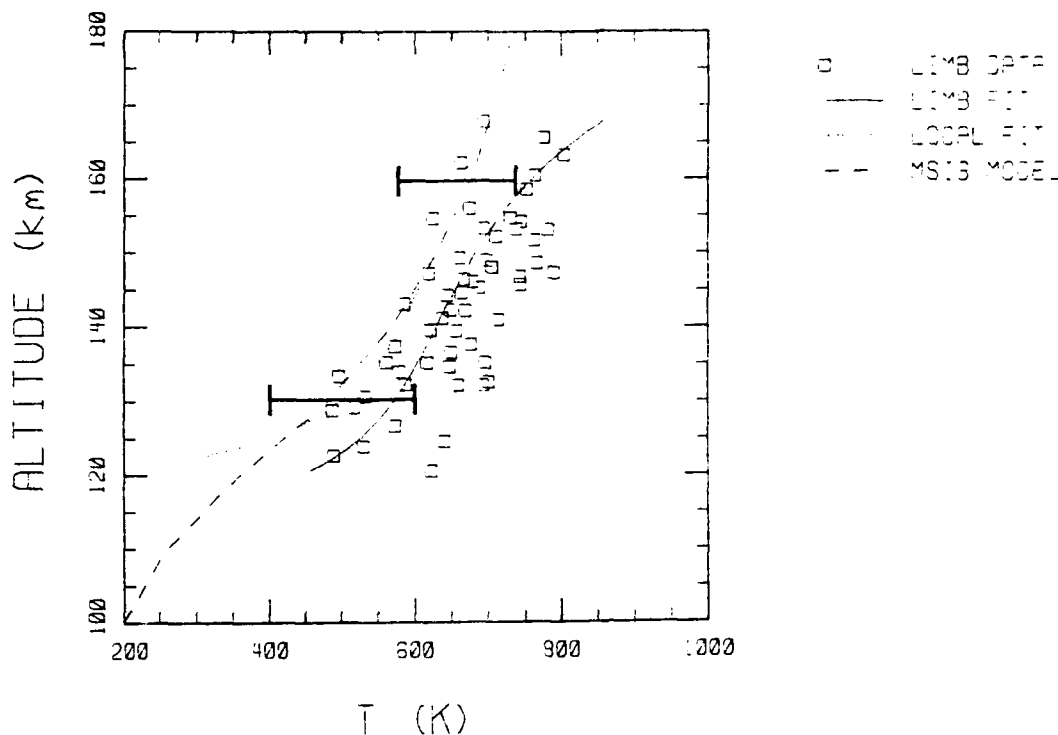


Figure 24. Limb and Local Kinetic Temperature Profiles from SPIRIT 1 NO $\Delta v=1$ Data. Error Bars Show Approximate Uncertainty in Local Temperature.

spectral moments. To within the rather large error bars which arise from scatter in the band shape, the determined profile is in agreement with the MSIS model.

4.4 O and H Profiles Derived for SPIRIT 1 and SPIRE

A method was developed for deriving atmospheric O and H atom density profiles in the mesopause region using ozone ν_3 emissions.⁴⁴ The 10-12 μm hot band intensity determines the $\text{O} + \text{O}_2 + \text{M}$ recombination rate, while the nighttime cold band intensity determines the chemical destruction rate and hence the H atom density. Cold band emissions under sunlit conditions (in the SPIRE experiment) have been used to provide an absolute calibration. Derived density profiles are presented for the SPIRIT 1 and SPIRE rocket experiments, and compare reasonably

with MSIS-86 model predictions. The somewhat lower atom densities found in the auroral SPIRIT 1 conditions may reflect local transport effects.

The computed O and H atom profiles for the SPIRIT 1 experiment are shown in Figs. 25 and 26. The SPIRE O atom density is 2-3 times larger, in better agreement with MSIS. The estimated absolute accuracy of the O atom profile is within a factor of two, while the H atom profile is believed to be more accurate than this.

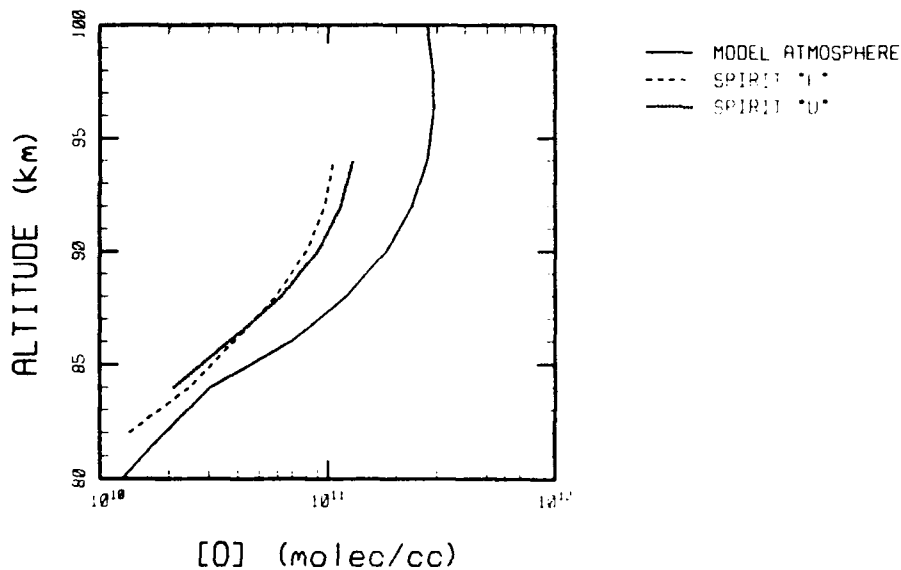


Figure 25. O Atom Profiles Calculated from the Inverted SPIRIT 1 Hot Band Data.

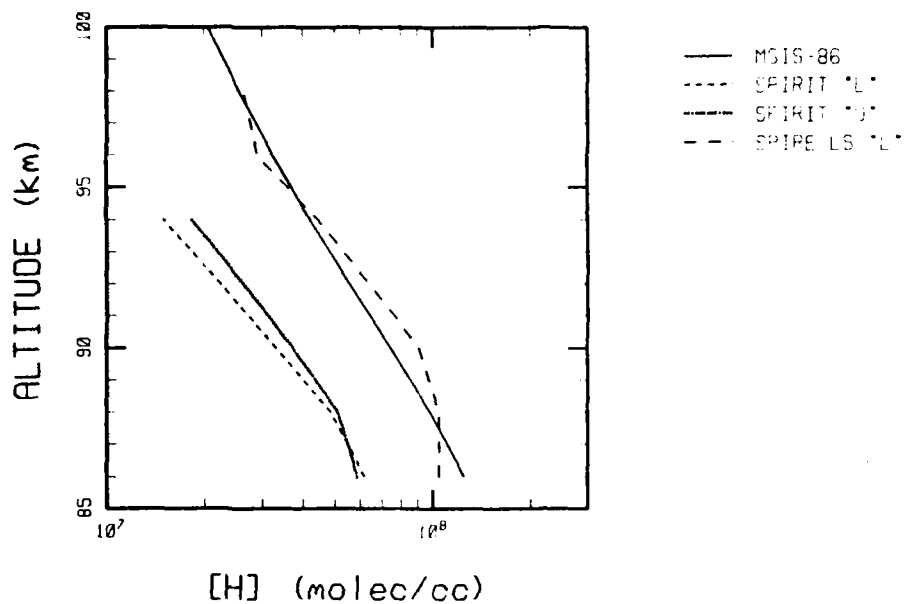


Figure 26. H Atom Profiles Calculated from the SPIRE and SPIRIT 1 Data. MSIS-86 Model Profiles are Essentially Identical for Both Experiments.

5. ANALYSIS OF EXCEDE DATA

The goal of EXCEDE III is to provide a data base to reduce uncertainties in modeling electron-dosed atmospheres. To this end the response of the natural, quiescent atmosphere to dosing by energetic electrons is studied. A beam of electrons having a nominal initial energy of 2.6 keV was injected into the upper atmosphere between 80 and 115 km. Optical instruments observed the interaction of these electrons with the atmosphere from both on-board the electron accelerator bearing module and from off-board platforms. EXCEDE III is the fifth flight in the EXCEDE program which has demonstrated the principle of artificially creating a electron-excited cloud in the upper atmosphere.

Four Circular Variable Filter Spectrometers (CVFs) were flown on EXCEDE III; one was located on the accelerator module to look at emissions near the electron beam source, while three were placed on the sensor module. Of these three, one CVF was pointed at the electron beam deposition region, looking at the prompt emission, a second looked in the region 8° behind the electron beam, corresponding to emissions nominally 0.2 seconds in the afterglow, and a third looked 20° behind the electron beam, measuring emissions 0.5 seconds in the afterglow. The CVFs had continuous spectral coverage from 2.4 to $21\ \mu\text{m}$ and 3% FWHM spectral resolution. Data from the three sensor CVFs measured emissions which provide important information on the time-dependent chemistry responsible for IR radiation. With the aid of interferometer measurements, emissions have been positively identified. Infrared spectra of CO_2 , CO, NO, and O_3 were seen both during beam-on and beam-off periods. Time histories of infrared-active bands are studied.

Current uncertainties in the phenomenological models based on reaction rate coefficients and calculated electron concentrations that affect infrared emissions are thought to be a factor of 2 or 3 in the best known situations and much worse in many other cases. Thus, it is important to validate both the emission rate and the mechanisms of formation of important IR radiators in the disturbed atmosphere. Particular species of interest are $\text{CO}_2(\nu_2 \text{ and } \nu_3)$, $\text{NO}(\Delta v = 1 \text{ and } \Delta v =$

2), $\text{CO}(\Delta v=1)$, NO^+ , O_3 , and other oxides of nitrogen such as N_2O and NO_2 . Unknowns, or disputed reaction rates, include the quenching of precursor species such as $\text{N}(^2\text{D})$ by $\text{O}(^3\text{P})$, fractional yields of species such as $\text{N}(^2\text{P})$ and $\text{N}_2(\text{A})$, effects of these species in the disturbed atmosphere, and creation mechanisms for species such as O_3 and N_2O . Emissions due to very high rotation levels which are not quenched in the field experiment may impact the atmospheric bandpasses being considered for possible surveillance instruments.

This section discusses a first-look analysis of the infrared data obtained from the Circular Variable Filter Spectrometers (CVFs) flown on the EXCEDE III sensor module. Only a small fraction of the available data and model calculations is presented here. A post-flight calibration of the CVF instruments has recently been completed, and, therefore, the data shown here is not yet final. Although much of this work is preliminary, qualitative observations from the data and kinetic model will no doubt survive a more rigorous quantitative analysis.

5.1 Sensor Module CVF Instrumentation

The purpose of the CVF instruments is to obtain spectral information on the prompt and delayed (afterglow) emission resulting from the irradiation of the atmosphere by an electron beam. The approximate scan time for each CVF was 1.8 sec. The spectral coverage was 2.4-21 μm with a 3% resolution.

As shown in Fig. 27, the arrangement of three CVFs on the sensor module at 0° , 8° , and 20° with respect to the electron beam allows spectral data to be obtained not only for prompt emission, but also for the afterglow region. In particular, for the geometry of the EXCEDE III flight, spectral data is obtained for up to 0.5 sec after the electron dosing.

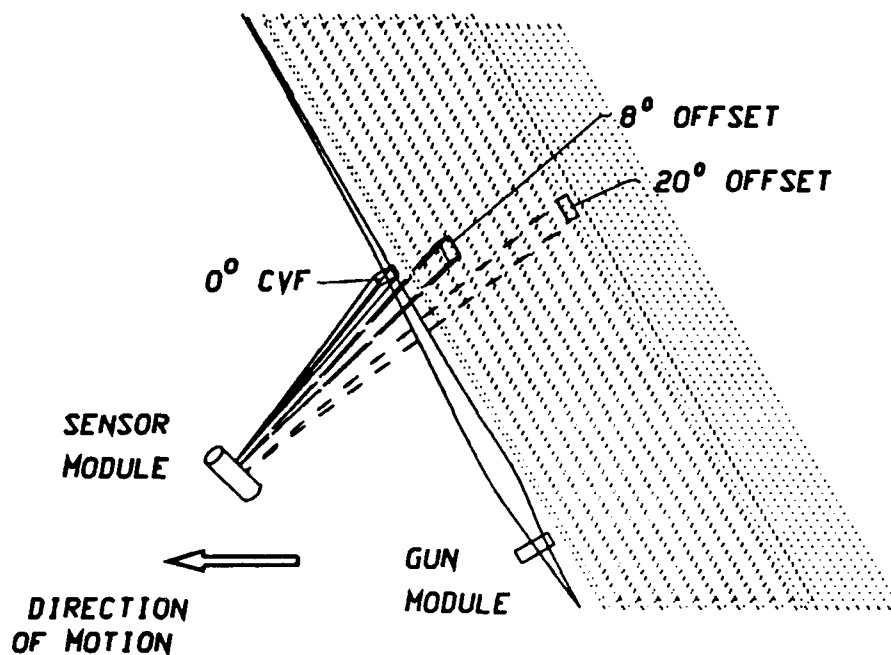


Figure 27. Sensor Module CVFs Fields-of-View.

5.2 Representative CVF Data

During the course of the experiment, each of the three sensor module CVFs obtained approximately 88 spectral scans. Two complete spectral scans were made during each beam-on period and one scan during beam-off. The altitude range over which the scans were taken was approximately 85 km to 115 km (apogee). Although excellent quality spectra were obtained for both electron-beam initiated emission and emission from the quiescent atmosphere, it should be realized that these data are still preliminary. In particular, no data are shown from the 0° CVF due to a calibration problem. The CVFs have only recently undergone a post-flight calibration, and the recalibrated data are not yet available.

The effect of the electron-beam dosing in the 2.4-6.0 μm is shown in Fig. 28. The data are from the 8° CVF looking approximately 0.2 sec into the afterglow. The time period shown includes three electron gun pulses corresponding to an altitude range of 113 to 107 km. The

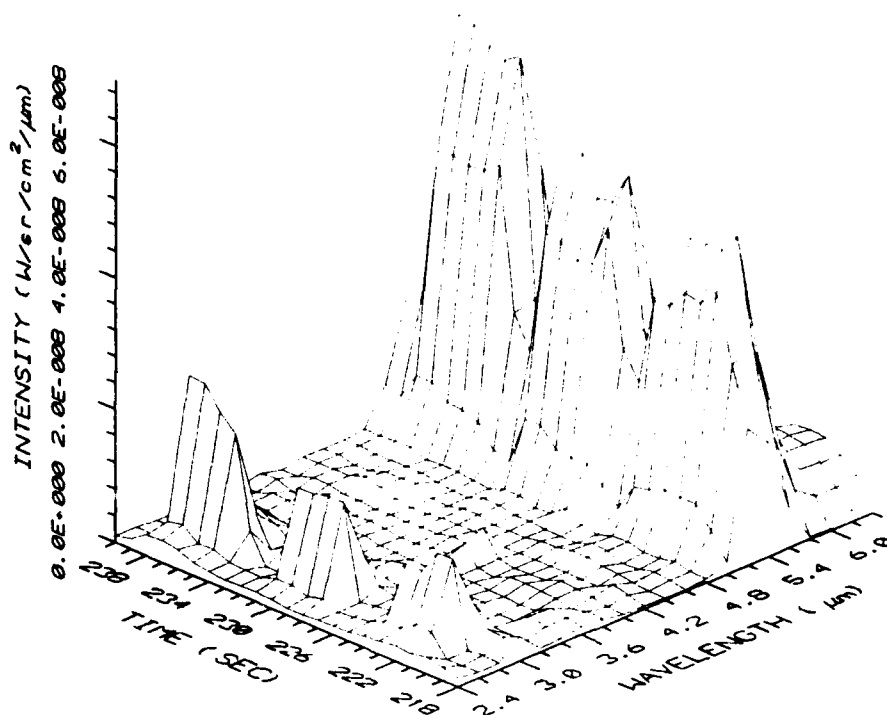


Figure 28. Electron Beam Enhancement of NO($\Delta v=1$) and NO($\Delta v=2$) Radiance for Three Electron Gun Pulses.

enhancement of the NO($\Delta v=1$) and NO($\Delta v=2$) emission at 5.3 μm and 2.7 μm is clearly shown. Although not evident from the figure, there is significant hot band emission at wavelengths greater than 5.3 μm (from vibrational states > 2) which is not present in the ambient emission.

Figure 29 illustrates the effect of the electron-beam dosing in the 8.5-10.5 μm spectral region. Again, the data are from the 8° CVF. This time period includes four electron gun pulses corresponding to an altitude range of 110 to 99 km. As expected, the O₃ (9.6 μm) intensity becomes significant below approximately 105 km. In contrast to NO, there does not appear to be any significant enhancement of the O₃ (9.6 μm) emission over the ambient background. However, this does not mean there is no O₃ (9.6 μm) enhancement due to the electron beam, only that the background is large enough to mask any electron beam

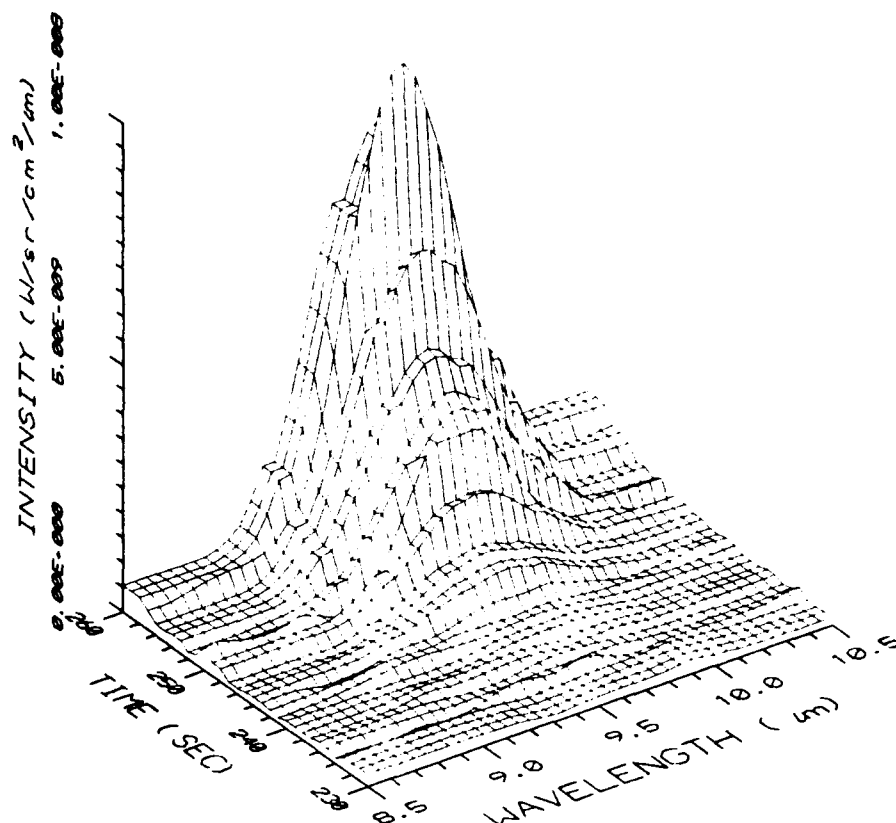


Figure 29. Effect of Electron Beam on O_3 ($9.6 \mu m$) Radiance During Four Electron Gun Pulses.

excitation. In fact, recent laboratory experiments at the Geophysics Laboratory have indicated that O_3 ($9.6 \mu m$) is very efficiently excited by electron bombardment.⁵⁰

The CVF data also provide a wealth of information on the time and altitude dependence of quenching and vibrational-to-vibrational energy transfer. For example, Fig. 30 shows the effects of the time-dependent collisional processes by comparing the 8° and 20° CVF data. Recall that the 8° and 20° CVFs look approximately 0.2 and 0.5 sec, respectively, after beam excitation. The effect of quenching on the prompt emitters, such as $NO(\Delta v=1$ and $2)$ at 5.3 and $2.7 \mu m$ and $CO(\Delta v=1)$ at $4.7 \mu m$ is quite dramatic. However, the behavior of $CO_2(\nu_3)$ at $4.3 \mu m$ is quite

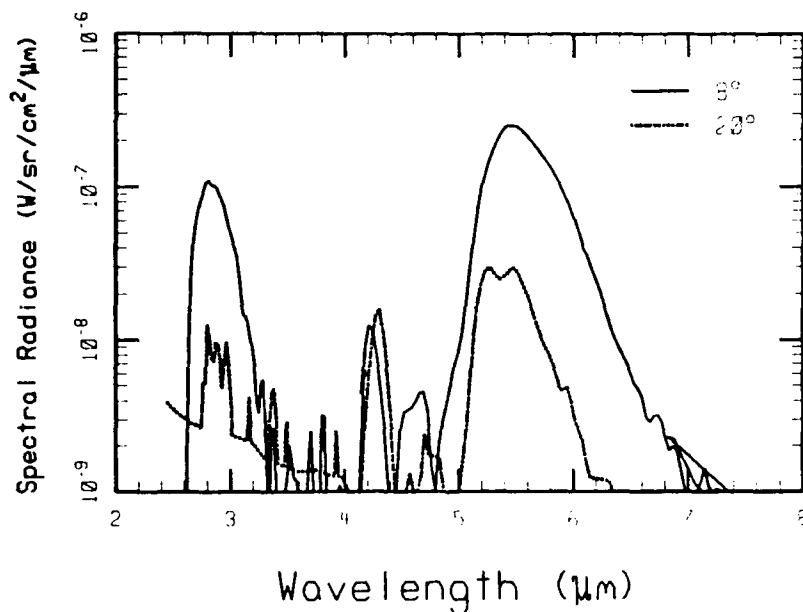


Figure 30. Time-Dependent Effects at an Altitude of 100 km Illustrated by the 8° and 20° CVFs.

different. The 20° CVF shows an increase in radiance over the 8° CVF due to the resonant energy transfer of CO₂ with vibrationally excited N₂ (see Subsection 5.3).

The effect of altitude on the electron beam-induced emission is shown in Figs. 31 and 32 for the 8° and 20° CVFs, respectively. These data were taken during the downleg portion of the flight. For the prompt emission from NO, quenching not only becomes increasingly important at longer times, but also becomes more important as altitude decreases. However, for NO, the most dominant quenching process appears to be the quenching of the precursor for NO, N(²D). The effects of quenching the high vibrational states of NO are also shown at long times. For CO₂, the quenching of CO₂(ν₃) and/or vibrationally excited N₂ is also evident. On the other hand, CO(Δv=1) is not effectively quenched and shows the effect of a relatively long vibrational lifetime.

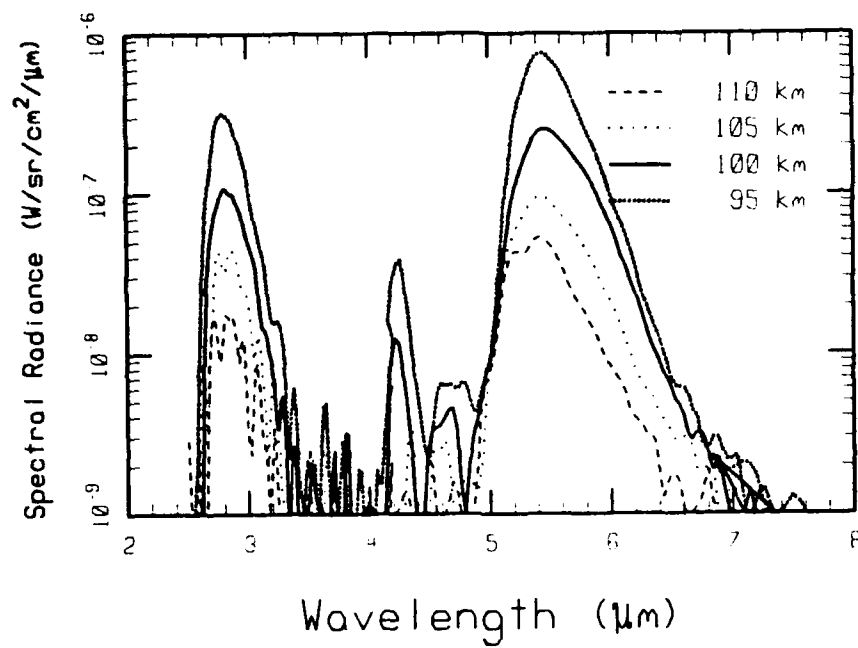


Figure 31. Altitude Dependence of the 8° CVF IR Data.

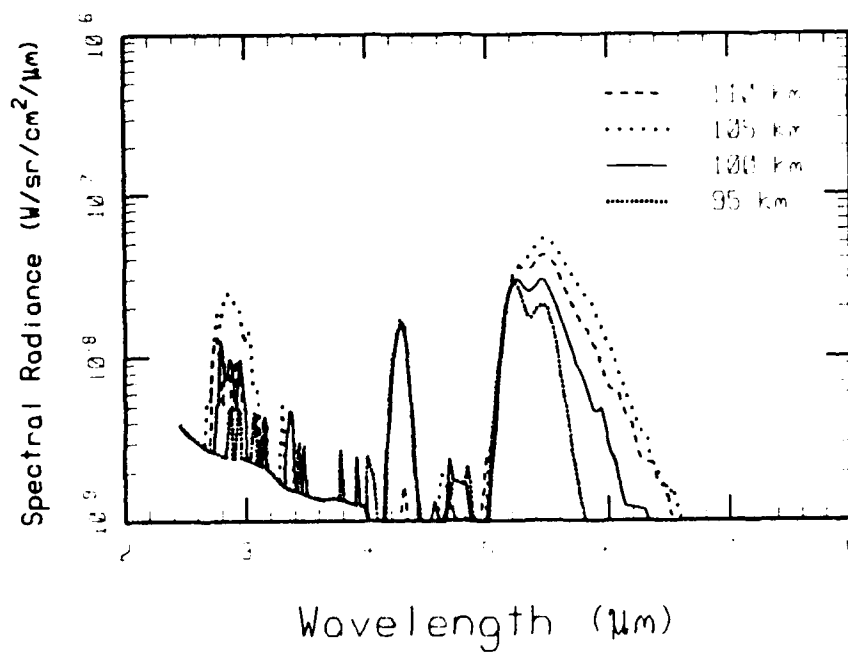


Figure 32. Altitude Dependence of the 20° CVF IR Data.

5.3 EXCEDE Kinetic Model

The most important IR emitters in an electron-dosed atmosphere include CO₂, CO, and NO. Emissions from O₃ are also of potential systems interest. However, much less is known about O₃ emission during disturbed conditions, and therefore it is much harder to treat its emission in detail. We have developed a general kinetic model (EXCEDE) to describe the chemical and collisional processes occurring during the electron dosing of the atmosphere. This code is based on the CHEMKIN code developed at Sandia Laboratories.¹⁵ The computer code uses a finite rate approach in modeling the generation of secondary electrons and the resultant molecular emission from collisions as well as from chemiluminescent reactions. In particular, the model:

- Solves the time and energy dependent rate equations for arbitrary dose rates and times to obtain species number densities,
- Treats the chemical and collisional processes for each vibrational state of interest,
- Assumes a simplified histogram treatment of the secondary electron spectra, and
- Uses an optically thin line-by-line treatment of molecular emission with the rotational temperature equal to the ambient temperature to obtain volumetric emissions.

Since the IR emission resulting from direct electron impact excitation, as well as recombination reactions, depends on the low energy secondary electron spectra, it is important that the histogram treatment retain the major features of the secondary electron spectra. Secondary electrons are formed via collisional ionization of M(= N₂, O₂, or O)



From an assumed initial secondary electron energy distribution, secondary electrons undergo further collisions with major species



and



which results in the relaxation or cascading of the secondary electron spectra.

5.3.1 Molecular Radiators

The three major IR radiators presently included in the EXCEDE code are NO, CO₂, and CO. Descriptions of the kinetics for NO and CO₂ are given in Subsection 3.1.2.

CO emission in the 4.7 μ m region is important in the atmospheric window to the red of CO₂ ν_3 . The primary source of excitation is from secondary electron excitation. Vibrationally excited CO is formed through shape resonance excitation by secondary electrons in the spectral regions of interest. Thus, the CO signature is calculated by the same technique as used to calculate CO₂ ν_2 . The primary reaction set used in these calculations is as follows:



The CO vibrational state populations predicted by Reactions (33) and (34) are in excellent agreement with those deduced from analysis of earlier EXCEDE flight data.

5.3.2 Model Predictions

The chemical kinetics mechanisms detailed above have been incorporated into the EXCEDE code data base. Preliminary calculations have been performed as a function of dose time and altitude in order to compare with the EXCEDE III CVF data. It should be emphasized that the

model calculations are preliminary in two ways: (1) the dose rates used are obtained from the ARCTIC⁵¹ model, as the beam dose rate profiles from the N₂⁺ first positive 319.4 nm emission are not yet available from the data and (2) the natural background has not been included in the calculations. Therefore, only a qualitative comparison with the data should be made.

The time dependence of the spectral emission for NO($\Delta v=1,2$), CO₂(ν_3), and CO($\Delta v=1$) at 100 km predicted by the EXCEDE kinetic model is shown in Fig. 33. Recall that the 0°, 8°, and 20° CVFs correspond approximately to 0, 0.2, and 0.5 sec after beam irradiation of the atmosphere. The trends in the model prediction should be compared with the data presented in Fig. 30. The qualitative agreement between the model and the data is very good. For NO, the effect of quenching as a function of time is clearly seen. The importance of both direct electron excitation of CO₂ and vibrational-to-vibrational energy transfer of vibrationally excited N₂ with CO₂ to form CO₂(ν_3) is also evident. From the calculations, the emission at 0° corresponds to

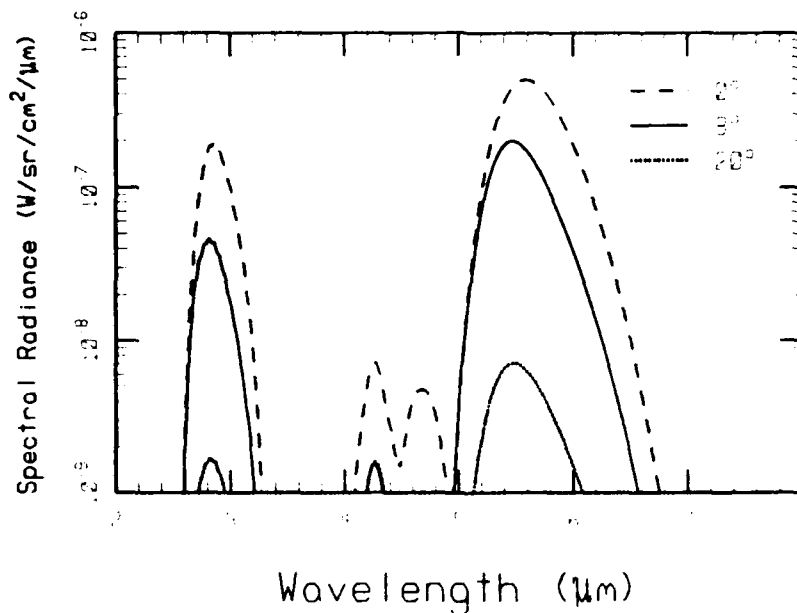


Figure 33. Model Prediction of the Time-Dependence of the 0°, 8°, and 20° CVFs at an Altitude of 100 km.

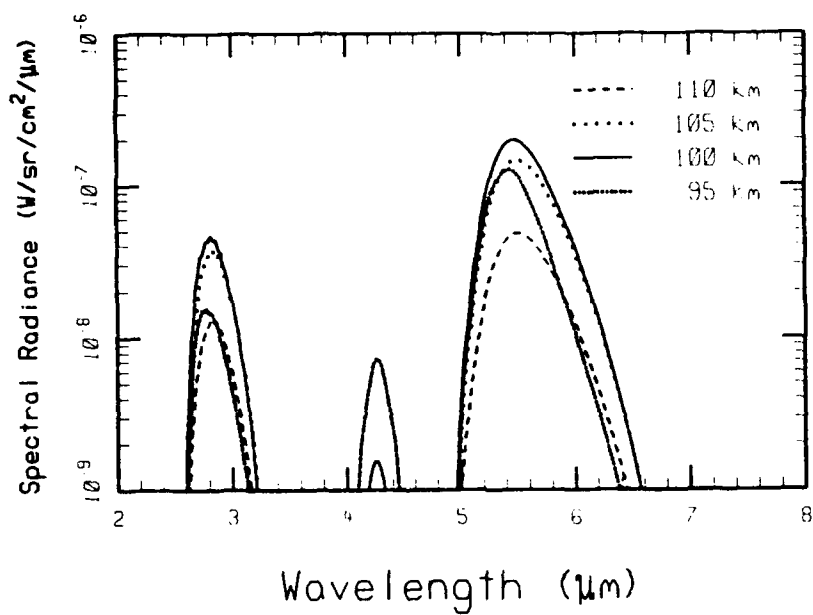


Figure 34. Model Prediction of the Altitude Dependence for the 8° CVF.

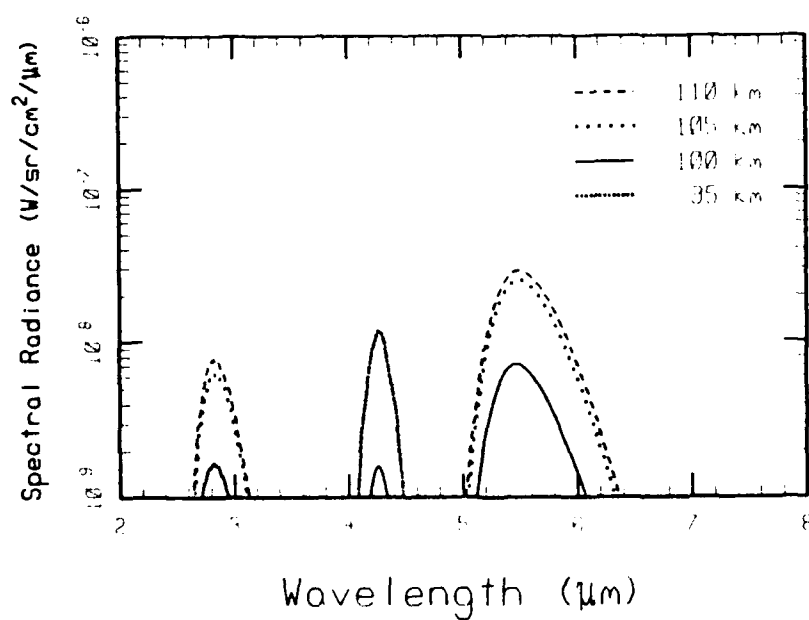


Figure 35. Model Prediction of the Altitude Dependence for the 20° CVF.

direct electron excitation (35), while 8° and 20° correspond to vibrational energy transfer with N_2 (Eqs. 19 and 20). In complete agreement with the data, the model shows that $CO_2(4.3 \mu m)$ emission increases with time.

The calculated altitude dependence of the electron beam-induced emission is shown in Figs. 34 and 35 for the 8° and 20° CVFs, respectively. These calculations should be compared with the data shown in Figs. 31 and 32. Although the trends illustrated by the model calculations are consistent with the data, there are two discrepancies worth mentioning. First, the model predicts that the NO emission peaks at 100 km, while the data indicate that NO emission is greatest at 95 km. This observation suggests that the quenching rate of $N(^2D)$ by O (Eq. 15) may be too fast. Indeed, there is some disagreement between laboratory measurements of the rate constant and the rate constant deduced from atmospheric observations. Secondly, the data show that CO emission decays at a rate much slower than expected based on the vibrational lifetime. Since the kinetic model for CO only includes direct electron excitation, the calculated CO emission is extremely small for the 8° and 20° CVFs (also see Fig. 33). This observation suggests that another mechanism for $CO(\Delta v=1)$ emission may exist.

5.4 Summary

Excellent electron beam-off and beam-on infrared data have been obtained in the altitude range of 85 to 115 km. The use of three CVFs offset from each other allows the measurement of time-dependent effects in an electron-dosed atmosphere. Significant enhancement of the quiescent atmosphere has been observed for NO (2.7 and $5.3 \mu m$), CO_2 ($4.3 \mu m$), and CO ($4.7 \mu m$). Inconclusive evidence has been found for NO^+ ($4.3 \mu m$), O_3 ($9.6 \mu m$), and CO_2 ($15 \mu m$) enhancement. However, it should be stressed that the lack of significant enhancement for certain species merely indicates that the background radiation dominates radiation from possible local electron-beam excitation. Comparison of the data with a kinetic model developed for EXCEDE indicate good qualitative agreement for both altitude and time-dependent processes.

6. CONCEPTS FOR A SMALL ROCKET EXPERIMENT

Experimental measurements of the altitude profiles of various ambient species, especially atomic oxygen, will help resolve questions and uncertainties in current models. One possible measurement concept which merits strong consideration is the utilization of small sounding rockets to directly measure species profiles. This concept has an advantage in that launch costs would be substantially reduced while still having the capability to perform multiple experiments. Reduced costs will permit multiple launches to provide information about species variability. The main constraint is that the measurement system must be small enough to fit into a small rocket and still be able to garner useful data. The feasibility of such measurements, including possible instrument configurations, were studied by Telic Optics, Inc.⁵² and HSS, Inc.⁵³ Telic Optics performed generic trade-off and stray-light analyses for an optical telescope, and HSS investigated the feasibility of packaging a high resolution spectrometer into a small volume. This section summarizes some key results.

6.1 Stray Light Analysis

Local IR atmospheric emissions at high altitudes are several orders of magnitude less than the upwelling radiation from the lower atmosphere and earth surface.⁵⁴ The small telescope apertures due to a small diameter vehicle can lead to severe problems with stray light contaminating the desired observations. Several candidate optical systems for a small-rocket measurement system were evaluated for stray-light effects. Small aperture-to-wavelength ratios generic to these systems cause diffracted stray light to be a major contributor to system stray light, even though such systems usually have both a field stop and a Lyot stop.

The results of the optical trade-off study can be summarized in graphs of the Point Source Transmittance (PST) and Stray Light Equivalent Spectral Radiance (SLESR). The general conclusions from the Telic Optics study are:⁵²

- 1) The stray light is dominated by diffracted stray light, even at shorter IR wavelengths (3-4 μm);
- 2) The L/D ratio of the baffle must be about 12 or greater to achieve the needed off-axis performance, that is, the aperture stop and primary mirror must be shaded from earthshine at all look angles; and
- 3) Performance can always be improved by making the baffle longer or the aperture stop larger.

6.1.1 Prototype Telescope Baffle

Stray light suppression in a small-aperture system can be dramatically improved by making a baffle that is oversize in diameter compared to the aperture stop of the system. When the off-axis angle to the earth is large enough so that the stop is not illuminated, any stray light must make four diffractions before impinging the FOV. First, light is diffracted at the baffle opening, then at the aperture stop (at the primary mirror), then at the field stop, and finally at the Lyot stop. At each diffraction the irradiance is reduced by a factor proportional to approximately $\frac{1}{\theta^3}$, where θ is the angle by which the light diffracts at that particular aperture. Oversizing the diameter of the baffle opening can easily increase the first diffraction angle by a factor of four (that is, from 1° to 4°), thereby reducing the multiple diffraction contribution to stray light by a factor of 64. This reduces the diffracted stray light to a level comparable to the baffle (multiple-scatter) contribution to stray light.

The oversize baffle concept was used to design a prototype baffle system, which is shown in Fig. 36. This was, in turn, used to study the fore-optics of a small-aperture spectrometer. Parameters used for the foreoptics include a 1:1 relay consisting of confocal paraboloids, but with the aperture stop at the first paraboloid, giving an L/D ratio for the stop equal to the L/D ratio for the primary mirror. In comparison

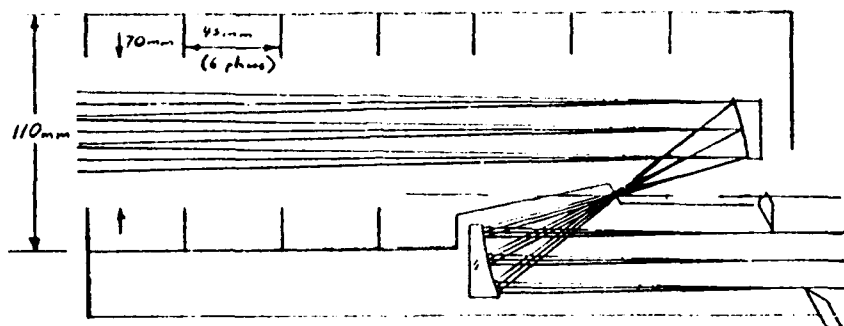


Figure 36. Small Aperture (One Inch) Foreoptics Design.

to a large (four-inch) aperture system, this small-aperture system gives equal performance at large earth angles (greater than 20°), and superior performance at small earth angles (10 to 20°). The baffle opening is oversized so that the edge of the baffle opening is 3° away from the near edge of the primary mirror.

The baffle vanes are closely spaced so that no first diffuse reflections strike the primary mirror, and furthermore, no first diffuse reflections from the outer baffle vane cavity can strike the unvaned portion of the baffle tube.

6.1.2 Prototype Optical System

One feasible optical system has a collecting aperture of only 1" which allows for the use of 1X confocal paraboloids. A wide FOV can be obtained by correcting the unit-magnification confocal paraboloids for all aberrations except field curvature.

The imaging capability of the telescope is felt to be of secondary importance since the image quality needs only to be sufficient to gather light from within the FOV and focus it on the spectrometer slit. Of greater importance is the control of aberrations between the aperture stop and Lyot stop. Diffraction is the dominant source of stray light in a small-aperture system, and it is important that rays diffracted at the aperture stop do not leak through the Lyot stop because of pupil

aberrations. The aperture stop is the edge of the primary mirror. That edge is a circle tilted with respect to the LOS. Its image is also tilted.

The aperture-stop image is also tilted because of the telescope field curvature. Tilting the Lyot stop increases its effectiveness. Figure 36 shows a schematic of this proposed optical design, and Table 3 lists relevant optical parameters.

The PST has been calculated for the baffle and foreoptics described above. The PST for a 9.2-10.0 μm bandpass is shown in Fig. 37. The oversize baffle greatly reduces the diffracted component of the PST to the point where it is small compared to the baffle scatter component for angles outside of the direct shading angle.

The Stray Light Equivalent Spectral Radiance (SLESR) is the amount of apparent spectral radiance that the system sees due to the presence of stray light in the system. It can be calculated from the PST by integrating the spectral radiance over the extended source (the earth) weighted by the PST, normalized to one steradian. The reduced PST results in SLESR values which meet a nominal sensitivity goal of $10^{-12} \text{ w/cm}^2/\text{sr}/\mu\text{m}$. Predicted values of SLESR are shown in Fig. 38 for this baseline 25 mm aperture system.

Table 3. 1X Telescope Optical Prescription.

Element	Radius	Thickness	Material	Clear Aperture Diameter
Baffle Opening	Infinite	300 mm	Air	70.0 x 88.0
Primary	-127.0 cc	-63.5	Refl	25.4
Field Stop	Infinite	-63.5	Air	2.382 x 7.153
Secondary	127.0 cc	127.0	Refl	30.2 x 39.7
Lyot Stop	Infinite	-	Air	22.9

Point Source Transmittance Band 3, 25mm ap, 300mm baf., 4deg HFOV

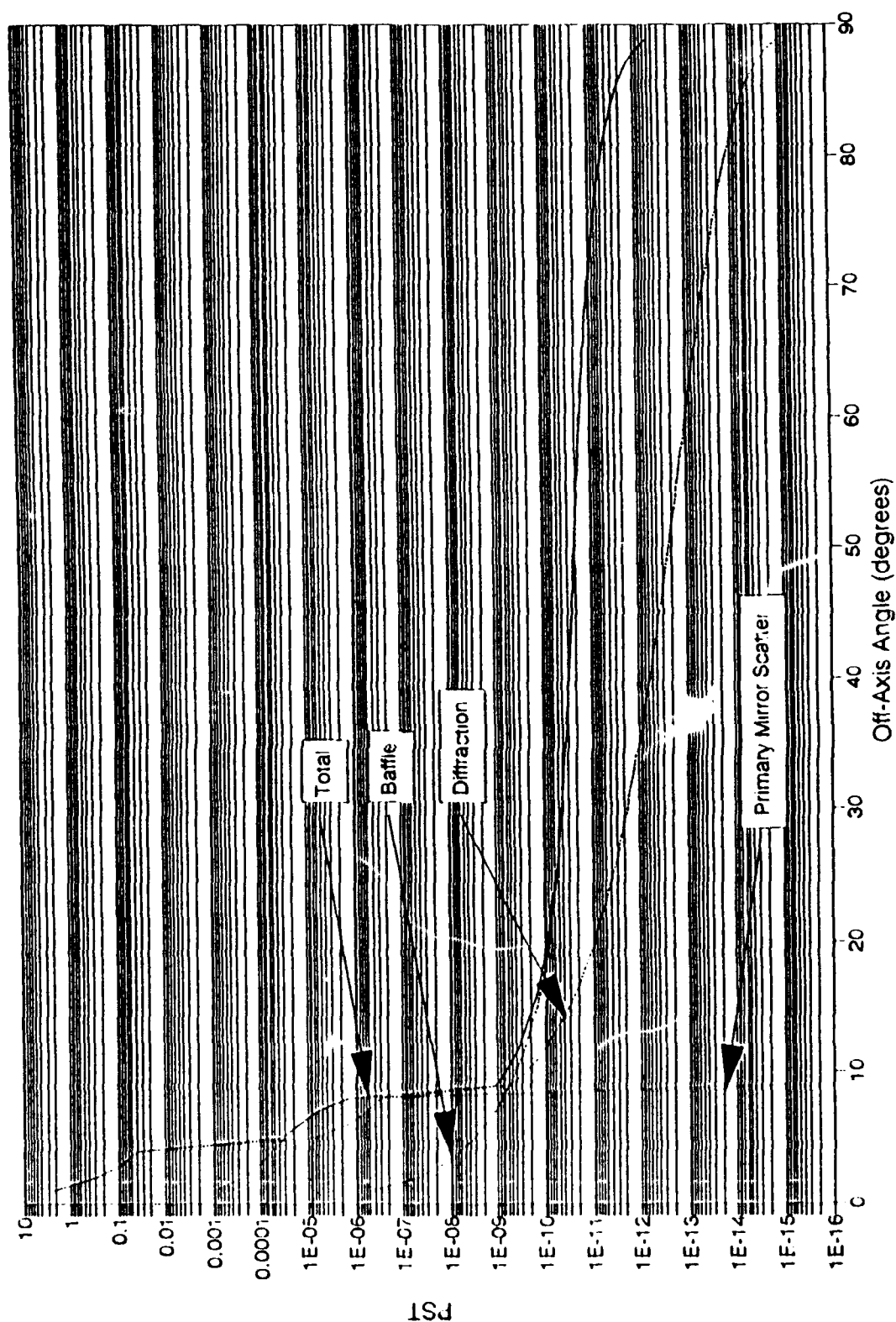


Figure 37. Point Source Transmittance (PST) for a Small-Diameter Optical System.⁵³

Stray Light Equiv. Spectral Radiance 25mm Aperture, 300mm Baffle, Waveband 3

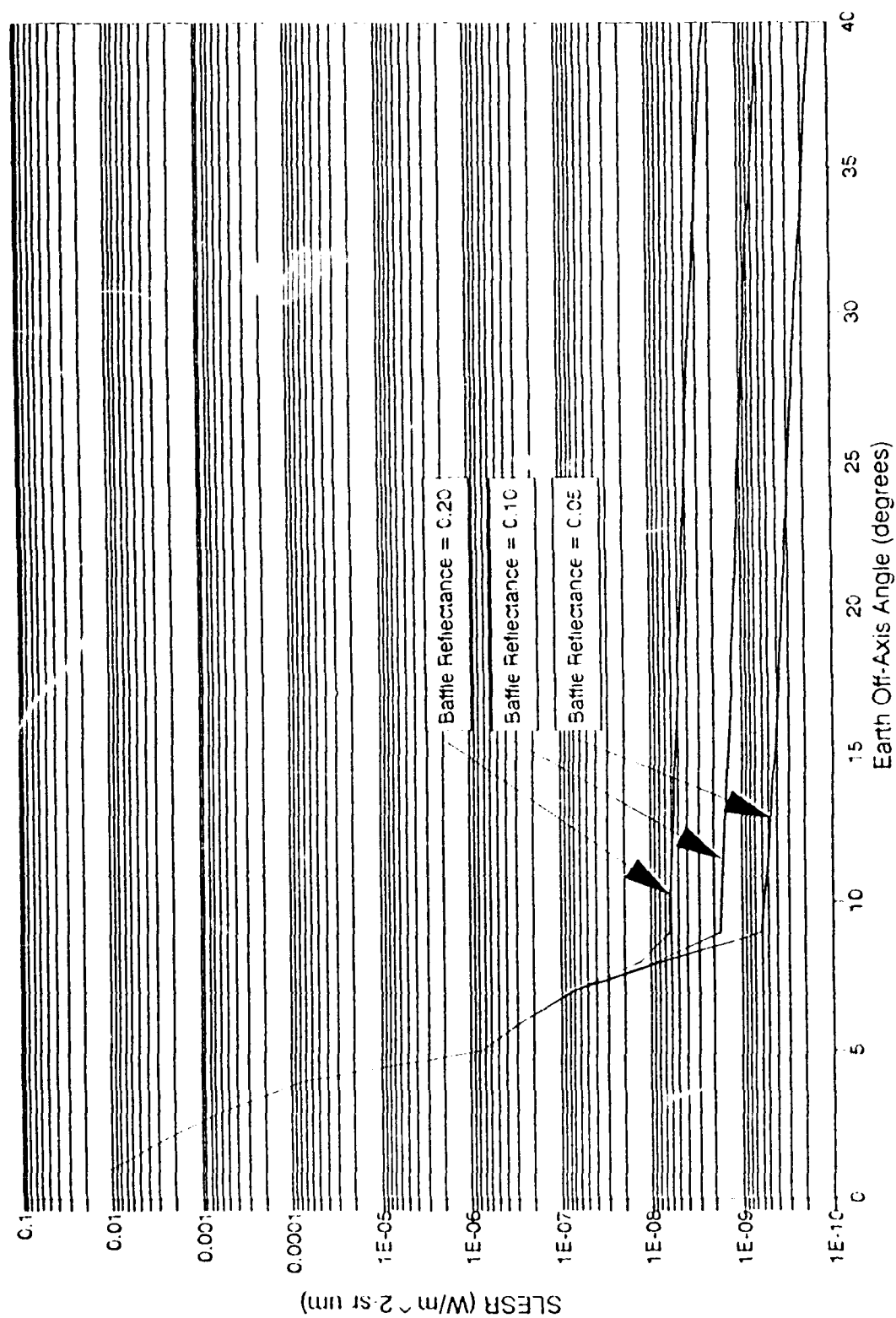


Figure 38. Stray Light Equivalent Spectral Radiance for a Small-Diameter Optical System that is Viewing the Earth Limb.⁵³

6.2 Prototype Instrumentation Package

HSS, Inc. developed and studied a conceptual design for a small-rocket IR grating spectrometer.⁵³ Sensitivity is an important issue because atmospheric emissions are weak in the window regions. Requirements for a grating spectrometer are driven by constraints imposed by the small size of the rockets. The advent of solid state photomultiplier (SSPM) detectors now makes it possible to design compact grating spectrometers that can achieve the needed spectral resolution and NESR. Further cost reductions would be achieved by developing a single reusable spectrometer that spans the full 4.5 to 22 μm range. On any given flight this spectrometer would measure the atmospheric emissions in only a small spectral region of 1-2 μm ; grating and detector/slit parameters would be changed for each flight to achieve optimum performance for the desired spectral region.

Spectrometer performance goals are listed in Table 4. Also shown are characteristics of a spectrometer that is likely to meet these goals. A spectral resolution of 2 cm^{-1} is assumed, although resolutions from 1 to 4 cm^{-1} are undoubtedly acceptable depending upon tradeoffs necessary to achieve other objectives. The threshold sensitivity is equivalent to 1/30 of the Zodiacal background radiance (ZLB), which is about $3 \times 10^{-11}\text{ w/cm}^2/\text{sr}/\mu\text{m}$ over the 4-20 μm region. Requiring the dynamic range of the spectrometer to be 1000:1 is related more to characteristics of the SSPM detector than to the the spectrometer design.

6.2.1 Design Constraints

The spectrometer will be flown on a rocket having a diameter of from 9 to 14 inches. Using a SSPM detector demands that the spectrometer be housed in a cryogenic vacuum dewar with an outside diameter of 7 to 12 inches, depending upon the rocket diameter. The dewar constrains the outside diameter of the spectrometer to be 5 to 10 inches, depending upon the size of the rocket. Total allowable payload

Table 4. Design Goals for a Small Rocket Spectrometer.⁵³

<u>PERFORMANCE</u>	
Operating Range	4.5 to 22 μm
Spectral Resolution	2 cm^{-1}
NESR	10^{-12} w/($\text{cm}^2.\text{sr}.\mu\text{m}$)
S/N Ratio	30:1
(Zodiacal Light Background)	
Dynamic Range	$10^3:1$
<u>CHARACTERISTICS</u>	
Type: LHe-Cooled, Prefiltered Grating Spectrometer	
Scan Time	2 sec
Field-of-View	2 degrees
Relative Aperture	f/2.5
Throughput	6×10^{-3} cm^2 sr
Detector:	
Type	SSPM
No. Channels	1
Objective Optics:	
Type	High Resolution Off-Axis Telescope
Aperture	5 cm^2
Baffle	High Efficiency Design; $1/D \geq 12$
Size	Compatible with a 9-14 inch diameter rocket
Weight (Including Cryostat)	100 to 200 lbs.

will be in the vicinity of 500 to 600 pounds with 100 to 200 pounds allocated to the spectrometer and cryogenic dewar; the remainder is allocated to payload support systems.

The LOS of the spectrometer will be oriented by the payload support system so that its FOV lies slightly above the earth's limb. A telescope and baffle system is required to sharply define the FOV and reject off-axis radiation from the earth's limb and lower atmosphere.

The telescope's objective will be about one inch in diameter and the FOV will be about 2 with a throughput of $6 \times 10^{-3} \text{ cm}^2 \text{ sr}$. Efficient coupling of the telescope to the spectrometer is required to maximize sensitivity.

6.2.2 Diffraction Grating Selection

The requirement for high linear dispersion in a spectrometer is customarily met by use of long focal length optics or high angular dispersion, or a combination of both approaches. Long focal length optics imply large instruments, an approach necessarily ruled out in the present situation where a small compact spectrometer is required.

The alternative approach, high angular dispersion, requires working at large diffraction angles. At large diffraction angles, however, wide spectral ranges are not possible with a single grating spacing unless a coarse ruling is employed. This, in turn, leads to large spectral order numbers, where many orders are required to cover a given spectral range. At extreme diffraction angles, the physical length of the grating becomes several times the aperture dimension so that for large apertures and fast f/numbers, the grating size becomes excessive.

The HSS study⁵³ concentrated on the use of coarse diffraction gratings and moderate diffraction angles to avoid an excessive grating size. This approach necessarily led to the use of multiple orders to cover the spectral range 4.4 to 22 μm .

Nominal grating and instrument parameters which are consistent with all other aspects of the spectrometer design are:

Grating Constant:	$a = 50 \mu\text{m}$
Diffraction Angle:	$\beta = 20^\circ$
Focal Length:	$f = 200 \text{ mm}$
Detector Element Width:	$w = 0.150$

6.2.3 Spectrometer Design

Because of the large spectral range (4.4 to 22 μm) to be covered by the spectrometer and the lack of suitable refractive optical materials

for such a range, reflective rather than transmission optics are indicated. Four basic spectrometer configurations were considered: the reflective (Littrow), the Ebert, the Conventional Czerny-Turner (CCT) and the Crossed Czerny-Turner (XCT). These configurations were selected for examination because of their known qualities of simplicity, compactness and fast relative apertures.

Primary consideration was given to throughput and image quality. The Littrow configuration was rejected because of lack of first-hand experience with it in the reflective version. (It appears to be more adaptable to refractive rather than reflective optics.) The Ebert configuration was rejected in favor of the Czerny-Turner configurations because the latter configurations offer larger numerical apertures with good image quality. Finally, the XCT configuration was chosen over the CCT configuration because experience has shown that for a given numerical aperture the XCT has smaller off-axis angles than the CCT and, hence, better resolution. The XCT also has the advantage over the Ebert and CCT in that it is less susceptible to the problem of re-entry spectra.

The basic shape of the spectrometer will have the form of a cylinder oriented with the axis of the cylinder parallel to the longitudinal axis of the carrier rocket. As described earlier, the radial dimension of the spectrometer is critical in that it is dictated by the size of the cryogenic dewar. The diameter of the dewar is determined in turn by the diameter of the carrier rocket. The possible range of 9 to 14 inches for the diameter of the rocket translates into a possible range of 5 to 10 inches for the radial dimension of the spectrometer. There is no critical constraint, within reason, on the length of the spectrometer.

There are two alternative applications of the basic spectrometer design, one as a scanning monochromator, the second as a spectrograph. The spectrograph version has the potential of stationary optics and a multiplex-advantage. The scanning monochromator has the potential advantages of greater throughput and superior spectral resolution. Both versions of the spectrometer were examined at some length.⁵³

6.2.4 SSPM Detectors

Critical to the performance of the spectrometer are the capabilities and limitations of the solid state photomultiplier (SSPM) detectors intended for use with the spectrometer. Information of this nature was supplied by technical personnel of AFGL and the SSPM development team at the Rockwell International Science Center.

SSPM's are small area (pixel size) photon counting detectors. They are a relatively new development in detection techniques and one may expect dramatic advances in their capabilities in the coming years. The detectors work well at cryogenic temperatures, 7 to 10°K, but apparently do not work well at the temperature of liquid helium (4.2°K). They have response capability extending from the visible to approximately 30 μ m, with a quantum efficiency which depends both on photon wavelength and on the type of illumination, front, back or edge.

For a small rocket spectrometer, the signal-to-noise ratio (S/N) is perhaps the most important indicator of spectrometer performance. The noise analysis considered two primary sources: (1) the dark count of the SSPM and (2) photon noise associated with the Zodiacal Light. A comparison of noise predictions for two versions of the spectrometer⁵³ showed that the spectrograph has a average factor of four to six advantage in S/N over the monochromator, the exact value depending on bandpass and specific design parameters.

7. IMPULSE APPROXIMATION FOR ATOM-MOLECULE COLLISIONS

The GL Field-Widened Interferometer (FWI) program¹⁹ observed emissions from excited states of NO in an aurorally disturbed atmosphere. R-branch band heads for the 3-2, 2-1, and 1-0 vibrational-rotational (VR) transitions were observed at 1960, 1990, and 2020 cm^{-1} , respectively. The appearance of these band heads leads to the identification of these emissions as high rotational states. Modeling studies which used a two-temperature model for the NO rotational states indicate that the band heads do not become observable until the high-temperature component reaches 2500 K. Thus the NO is in a highly NLTE state. One hypothesis for the formation of these states is that they result from VR transfer of energy during the collision of ambient species with excited atoms which have been produced via chemiluminescent processes.⁵⁵ This section discusses the Impulse Approximation (IA) for atom-molecule collision processes and its extension to include the effects of VR energy transfers.^{56,57}

In the IA three-body process are treated as a pair of atom-atom collisions, with the third atom in each case remaining a spectator. This formalism was originally developed by Chew⁵⁸ in the context of neutron-deuteron collisions. It has also been applied to atomic physics problems by Bogan,⁵⁹ by Eckelt, Korsch, and Philipp,⁶⁰⁻⁶³ and by Beard and Micha.⁶⁴ The scattering amplitudes for the two processes are determined by the momentum space wave functions of the molecular initial and final states and the two-body T-matrices. The differential cross section is determined by summing over the two two-body amplitudes. The earlier work⁵⁹⁻⁶⁴ dealt with hyperthermal collisions where the energy of the projectile atom is quite high (of the order of an electron volt or higher). In Sharma's suggestion,⁵⁵ low projectile energy collisions may be treated in the IA when the molecular internal energy is large. Thus it is the relative velocity of the projectile with respect to the molecular atom that matters in the two-body impulsive collision. A large relative velocity is achieved by having either a fast projectile or a highly excited molecule. With appropriate modifications, the IA

formalism may then be capable of representing a large variety of collision processes that are applicable to atmospheric processes.

Previously the IA has been employed by making a further approximation called the Peaking Approximation (PA).⁶⁰⁻⁶⁴ The typical two-body process is represented in the IA by

$$I_1 = \int \phi_f^*(\vec{q}_3) T(\vec{q}_1, \vec{q}_1, \epsilon) \phi_i(\vec{q}_3) d\vec{p}_1, \quad (35)$$

where \vec{p}_1 is the spectator atom momentum, ϕ_i and ϕ_f the momentum space wave functions of the initial and final states, and T is the two-body T-matrix. \vec{q}_3 is the molecular relative momentum, and \vec{q}_1 is the two-body relative momentum, with the relation

$$\vec{q}_1 = a\vec{p}_3 - b\vec{q}_3 \quad (36)$$

$$a = 1 - \frac{1}{2}b, \quad b = \frac{m_2}{m_2 + m_3}, \quad (37)$$

where \vec{p}_3 is the incoming (projectile) momentum. The momenta are defined in the center-of-mass reference frame for the collision and are expressible⁶⁴ in terms of any two of the Jacobi momenta \vec{p}_i and \vec{q}_i . For simplicity we describe here the homonuclear case ($m_1 = m_2$). Integration of Eq. (35) is quite involved and is simplified⁶²⁻⁶⁴ in the PA by approximating T with its (fixed) value at $\vec{p}_1 = \vec{p}_1^0$, where the product of the two wave functions is peaked. Then T can be pulled out of the integral, and the remaining molecular wave function overlap integral leads to a form factor which depends on the properties of the target.

While the IA can be applied to many physical situations, the PA is rather restrictive. In order to employ the IA for a wider class of phenomena, it is thus essential to develop a formalism which does not invoke the PA. Initial steps toward such a formalism was developed in the course of this work. It requires a more involved angular momentum coupling algebra and also more intricate radial integrals. The directional correlation between the momentum transfer of the impulse collision and the momentum transfer appearing in the target form factor was not recognized in the PA. The new, more general formalism fully

recognizes this correlation and can determine when the PA is (or is not) a good approximation.^{56,57} In terms of Eq. (37), it can be shown that if \vec{q}_1 is dominated by the projectile momentum, \vec{p}_3 , the PA will be reasonable since T does not vary much over the domain of integration in Eq. (35). On the other hand, for processes dominated by the molecular momentum \vec{q}_3 , the PA will not be adequate, and the more general approach is necessary.

The new formalism is based on a representation for the T-matrix which recognizes the invariance of the momentum transfer $\Delta\vec{p} = \vec{p}_3' - \vec{p}_3 = \vec{q}_1' - \vec{q}_1$ in evaluating the integral in Eq. (35). The T-matrix can be expanded in a complete set of spherical harmonics⁵⁶

$$T(\vec{q}_1', \vec{q}_1; \epsilon) = \sum_{LM} Y_{LM}(\hat{q}_3) T_{LM}(q_3; \Delta p, p_3, \Theta) \quad , \quad (38)$$

where Θ is the angle of scattering between initial and final projectile momenta, \vec{p}_3 and \vec{p}_3' . For low projectile energies ($ap_3 \ll bq_3$), \vec{q}_1 is essentially along \vec{q}_3 , and a simpler expansion results,

$$T(\vec{q}_1', \vec{q}_1; \epsilon) = \sum_L P_L(\hat{q}_3 \cdot \Delta\hat{p}) T_L(q_3; \Delta p, \Theta) \quad . \quad (39)$$

Both Eqs. (38) and (39) are found to be rapidly convergent in L , and thus this Momentum Transfer Representation (MTR) offers significant advantages over the standard expansion.⁶⁰⁻⁶⁴ The expansion coefficients T_{LM} in Eq. (38) were evaluated numerically for the hard core potential by employing the orthogonality relations of the spherical harmonics and taking the T-matrix for the hard core potential as given in the standard representation by Van Leeuwen and Reiner⁶⁵ and Beard and Micha,⁶⁴

$$T(\vec{q}', \vec{q}; \epsilon) = \frac{1}{4\pi} \sum_{\ell} (2\ell + 1) t_{\ell}(q', q; \epsilon) P_{\ell}(\cos \phi) \quad . \quad (40)$$

The expansion coefficients T_L in Eq. (39), for the low projectile energy limit, were evaluated numerically by employing the orthogonality relations of the Legendre functions. For the "post" form of the T-matrix, characterized by $\epsilon = h^2 q_1^2 / 2\mu_{1,3}$, it was discovered from the numerical evaluations that T_L had the exact factorization property

$$T_L(q, \Delta p) = j_L(\Delta p) t_L(q) \quad . \quad (41)$$

This remarkable result offers considerable computational advantage in subsequent calculations. It can also be shown that $t_L(q)$ are related to the forward scattering amplitude and its derivatives.

In the new formalism, the integration in Eq. (35) is accomplished without making any approximations. This is a significant step in the development of the IA, which can now be applied to a wider variety of physical situations since it is no longer necessary to invoke the PA. The general approach is based on taking \vec{q}_3 as the variable of integration in Eq. (35). T is expressed in terms of \vec{q}_3 through Eq. (38). The final state wave function, which depends on $\vec{q}_3 = \vec{q}_3 - \frac{1}{2}\Delta\vec{p}$, is represented through an inverse Fourier transform in terms of a coordinate space integral. The \vec{q}_3 dependence is now explicit, and the angular and radial integrals in \vec{q}_3 space can be carried out. The angular integral gives various Clebsch-Gordan (CG) coefficients.^{56,57} Computer programs were developed to evaluate the radial integrals and the various CG and Racah coefficients. The hyperthermal limit ($ap_3 \gg bq_3$) is compared to previous treatments⁶⁰⁻⁶⁴ for which the PA emerges as limiting cases of this formalism. The precise errors involved in invoking the PA for a given set of physical parameters can be determined with this formalism. As an application, this approach was evaluated by looking at the cross sections for N_2 excitations resulting from collisions with Li^+ .⁵⁷ Figure 39 presents an illustrative comparison of the calculated differential cross sections for the N_2 , $v' = 2$ and 3, excited states and shows that the PA significantly overestimates the exact IA cross section for this excitation processes. Thus the PA is inadequate in the low energy limit, and this new formalism offers a uniform method for any projectile and molecular energies.

Possible extensions for the next higher level of approximation are the double collision terms in the expansion of the scattering matrix. Three feasible approaches that merit further study are:

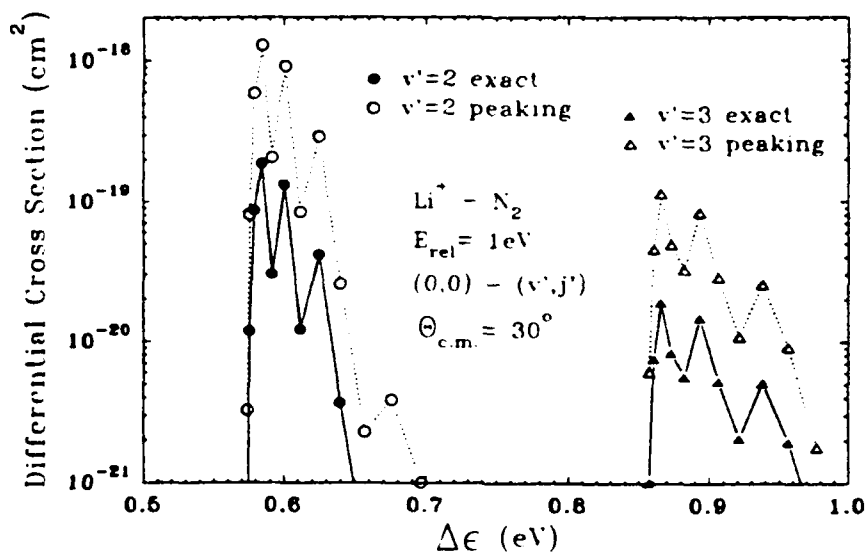


Figure 39. Differential Cross Sections (cm^2) for the Exact and PA Calculations vs. Energy Loss (eV) for the Collision Process $\text{Li}^+ + \text{N}_2(v=0) \rightarrow \text{Li}^+ + \text{N}_2(v=2,3)$ at a Center-of-Mass Scattering Angle of 30° and an Initial Translational Energy of 1 eV. The Peaking Calculations (o and Δ) give Larger Cross Sections than the Exact Calculations (Solid Symbols). (From Ref. 58.)

1) Calculate each process ($\vec{p} \rightarrow \vec{p}''$, $\vec{p}'' \rightarrow \vec{p}'$) in its momentum transfer representation (\hat{z} along $\vec{q}' = \vec{p}'' - \vec{p}$ and $\vec{q}'' = \vec{p}' - \vec{p}''$, respectively). This approach allows the individual collision amplitudes to be calculated with minimal computation. The integration over the intermediate momentum \vec{p}'' , and the summation of the intermediate molecular states is not practical in this approach as it would require numerical integration.

2) Another approach is to take \hat{z} , the quantization axis, along \vec{p} , the incoming projectile direction. The second process can be computed using \vec{p}' as the quantization axis. While the individual amplitudes can again be written down and computed (with slightly more computational effort than in case 1), the intermediate integration over \vec{p}'' is still not feasible, analytically, and would require numerical integration. As in case 1, the accuracy of the final result would be questionable, unless a very large numerical grid is employed.

3) In view of these difficulties, which could not be overcome so far, we return to a previous strategy, that is using the general expression for an arbitrary direction of quantization, and expressing the single collision amplitude in terms of a bilinear harmonic form in terms of the incoming and outgoing directions. Then the intermediate momentum integration over the angles is analytically feasible. This allows one to express the double collision amplitude as an integral over the magnitude \bar{p} and the summation of the intermediate molecular states.

In terms of accuracy, which is essential, since the double collision term is a correction, the third approach may be the best. It is computationally extensive, and it may be best to work with small j and j' to limit the computing time. Considering the same processes as in the cited papers ($0,0 \rightarrow 1,6$ or $0,2 \rightarrow 1,6$, etc.),^{56,57} this would allow one to determine if the double collision term can extend the domain of semi detailed balance non-violation to smaller scattering angles.

8. FINE-STRUCTURE TRANSITIONS IN COLLISIONS OF OXYGEN ATOMS

A detailed formulation of the scattering of oxygen atoms in collisions with each other could provide a basis for inferring oxygen altitude profiles from field measurements of its various ground-state transitions. As part of this formulation, the correspondence between atomic molecular states is worked out. An expression is obtained for the cross section for transitions amongst the fine-structure states. The molecular potential energy curves that enter into the cross section calculations are assembled.

8.1 Introduction

The interpretation of the fine-structure emissions of atomic oxygen in the atmosphere involves a determination of the populations of the fine-structure levels. At low altitudes, collisions will maintain the levels in thermal equilibrium, but at some critical altitude that depends on the magnitude of the collision cross sections the levels will fall out of thermal equilibrium, and a detailed solution of the equations of statistical equilibrium is required. The cross sections are uncertain. The only calculation, that of Allison and Burke,⁶⁶ was based on a first order perturbation theory of the interactions, which cannot be accurate at the low velocities at which collisions take place in the atmosphere. Here we present the full molecular theory. It involves a much more complicated angular momentum coupling process.

8.2 Theoretical Formulation

The total Hamiltonian may be written

$$H_T = H_a + H_b + \sum_{ij} V(\vec{r}_{ia}, \vec{r}_{jb}) + H_N \quad (42)$$

where

$$H_a = -\frac{1}{2\mu} \sum_i \nabla_{r_{ia}}^2 + V(r_{ia}) \quad (43)$$

is the electronic Hamiltonian of one of the atoms a , H_b is the electronic Hamiltonian of the other atom b , $V(\vec{r}_{ia}, \vec{r}_{jb})$ is the electron-electron repulsion between the electrons in a and b , and H_N is the nuclear Hamiltonian containing the electrostatic interactions between the electrons of each atom with the nuclei of the other. We write the eigenstates of H_a as $\phi_a(r_{j,a}, \dots, r_{N,a})$ and of H_b as $\phi_b(r_{N+1,b}, \dots, r_{2N,b})$. We designate the quantum numbers of the states of a by $\alpha = (\ell_a m_a s_a m_{s_a})$ where $\ell_a m_a$ are the orbital angular momentum and projection quantum numbers of a , and similarly we define $\beta = (\ell_b m_b s_b m_{s_b})$ for b .

At large internuclear distances R , the molecular eigenstates are linear combinations of

$$|\ell_a m_a\rangle |\ell_b m_b\rangle |S M_S\rangle$$

where S and M_S are respectively the total spin and spin projection quantum numbers.

It is convenient to introduce the angular functions

$$|L A S M_S\rangle = (-1)^{\ell_b - \ell_a - \Lambda} \sqrt{2L+1} \sum_{m_a m_b} \begin{pmatrix} \ell_b & \ell_a & L \\ m_b & m_a & -\Lambda \end{pmatrix} |\ell_a m_a\rangle |\ell_b m_b\rangle |S M_S\rangle \quad (44)$$

which, however, are not eigenfunctions of the total angular momentum $\vec{L} = \vec{\ell}_a + \vec{\ell}_b$, because the kets $|\ell_a m_a\rangle |\ell_b m_b\rangle$ are defined on different centers. It may be shown by following procedures used by Knipp,⁶⁷ Chang,⁶⁸ and Uminskij and Nikitin,⁶⁹ that for singlet molecular states $S=0$, the gerade (g) Born-Oppenheimer states separate to $L=0$ or $L=2$ atomic states, and ungerade (u) states separate to $L=1$ atomic states. For triplet molecular states $S=1$, the g states separate to $L=1$ and the u states to

L=0 and 2 states, and the u states to L=1. The detailed connections are given in Table 5. There are 81 molecular states formed in the approach of two 3P oxygen atoms.

There is a one-to-one correspondence between the atomic and molecular states except for the $b^1\Sigma_g^+$ and $2^1\Sigma_g^+$ states, the $A^3\Sigma_u^+$ and $2^3\Sigma_u^+$ states, and the $1^5\Sigma_g^+$ and $2^5\Sigma_g^+$ states which are different linear combinations of $|L=0, M=0, S M_S\rangle$ and $|L=2, M=0, S M_S\rangle$ states with $S=0, 1$ and 2 , respectively. To determine the correct linear combinations, we must consider the nature of the interaction at large internuclear distances.

Table 5. Connections between Atomic and Molecular States for Two Oxygen 3P Atoms.

NO. OF DEGEN. STATES	Λ	INVERSION		MOLECULAR STATE	ATOMIC STATE
		S			
2	± 2	0	g	$1\Delta_g$	$ L=2 M=\pm 2 S=0 M_S\rangle$
2	± 1	0	g	$1\Pi_g$	$ L=2 M=\pm 1 S=0 M_S\rangle$
2	± 1	0	u	$1\Pi_u$	$ L=1 M=\pm 1 S=0 M_S\rangle$
1	0	0	u	$1\Sigma_u$	$ L=1 M=0 S=0 M_S\rangle$
2	0	0	g	$b^1\Sigma_g^+, 2^1\Sigma_g^+$	$\{ L=0 M=0 S=0 M_S\rangle, L=2 M=0 S=0 M_S\rangle \}$
<hr/>					
6	± 2	1	u	$3\Delta_u$	$ L=2 M=\pm 2 S=1 M_S\rangle$
6	± 1	1	u	$3\Pi_u$	$ L=2 M=\pm 1 S=1 M_S\rangle$
6	± 1	1	g	$3\Pi_g$	$ L=1 M=\pm 1 S=1 M_S\rangle$
3	0	1	g	$3\Sigma_g$	$ L=1 M=0 S=1 M_S\rangle$
6	0	1	u	$A^3\Sigma_u^+, 2^3\Sigma_u^+$	$\{ L=0 M=0 S=1 M_S\rangle, L=2 M=0 S=1 M_S\rangle \}$
<hr/>					
10	± 2	2	g	$5\Delta_g$	$ L=2 M=\pm 2 S=2 M_S\rangle$
10	± 1	2	g	$5\Pi_g$	$ L=2 M=\pm 1 S=2 M_S\rangle$
10	± 1	2	u	$5\Pi_u$	$ L=1 M=\pm 1 S=2 M_S\rangle$
5	0	2	u	$5\Sigma_u$	$ L=1 M=0 S=2 M_S\rangle$
10	0	2	g	$1^5\Sigma_g^+, 2^5\Sigma_g^+$	$\{ L=2 M=0 S=2 M_S\rangle, L=0 M=0 S=2 M_S\rangle \}$

Expanding the interaction potential in multiples,

$$V = \sum_{Q=3}^{\infty} \frac{V_Q}{R^Q}, \quad (45)$$

where

$$V_Q = \sum_{i=1,2} \sum_{j=3,4} \sum_{L=1}^{Q-2} \sum_M G(L,M) \times Y_L^M(\vec{r}_i) Y_{-Q-L-1}^{-M}(\vec{r}_j) r_i^L r_j^{Q-L-1}, \quad (46)$$

i refers to electrons on atom a and j to electrons on atom b , and $G(L,M)$ is a coefficient given by Chang.⁶⁸ For $3p-3p$ interactions of neutral atoms, the leading term is the quadrupole-quadrupole interaction $Q=5$. After some angular momentum algebra, we obtain for the asymptotic matrix element of the interaction potential

$$\langle M_a, M_b | V_5 | M_a, M_b \rangle = \frac{54}{\pi} \frac{\langle r^2 \rangle^2}{R^5} R(M_a, M_a'; M_b, M_b') \quad (47)$$

where r^2 is the expectation value for a single p electron of oxygen, and R is a sum of products of 3- j symbols

$$R(M_a, M_a'; M_b, M_b') = (-1)^{M_a + M_a' + M_b + M_b'} \sum_M G(L=2, M) \times \sum_{\substack{M_1, M_3 \\ M_1', M_3'}} (-1)^{M_1' + M_3'} \begin{pmatrix} 1 & 1 & 1 \\ M & M_1 & -M_a \end{pmatrix} \begin{pmatrix} 1 & 1 & 1 \\ M & M_1' & -M_a' \end{pmatrix} \times \begin{pmatrix} 1 & 2 & 1 \\ -M_1' & M & M_1 \end{pmatrix} \begin{pmatrix} 1 & 1 & 1 \\ M_3 & M' & -M_b \end{pmatrix} \begin{pmatrix} 1 & 1 & 1 \\ M_3' & M' & -M_b' \end{pmatrix} \begin{pmatrix} 1 & 2 & 1 \\ -M_3' & -M & M_3 \end{pmatrix} \quad (48)$$

The matrix element of V_5 can be expressed more simply by introducing a 6- j coefficient in the form

$$\langle M_a, M_b | V_5 | M_a M_b \rangle = \frac{54}{\pi} \left| \begin{pmatrix} 1 & 1 & 2 \\ 1 & 1 & 1 \end{pmatrix} \right|^2 \sum_M g(2, M) (-1)^{M_a + M_b} \quad (49)$$

$$\times \begin{pmatrix} 1 & 1 & 2 \\ -M_a & M_a & -M \end{pmatrix} \begin{pmatrix} 1 & 1 & 2 \\ -M_b & M_b & M \end{pmatrix} .$$

Now define states of angular momentum $J=L+S$ according to

$$|JM_J\rangle = (-1)^{M_J} \sqrt{2J+1} \sum_{M_a M_b} \begin{pmatrix} 1 & 1 & J \\ M_b & M_a & -M_J \end{pmatrix} |L=1, M_a\rangle |L=1, M_b\rangle \quad (50)$$

Then

$$\langle J' M_J' | V_5 | JM_J \rangle = \frac{54}{\pi} \frac{\langle r^2 \rangle^2}{R^5} \left| \begin{pmatrix} 1 & 1 & 2 \\ 1 & 1 & 1 \end{pmatrix} \right|^2 \sum_M g(2, M) \sqrt{2J+1} \sqrt{2J'+1} \quad (51)$$

$$\times \sum_{\substack{M_a, M_a' \\ M_b, M_b'}} \begin{pmatrix} 1 & 1 & J \\ M_b & M_a & -M_J \end{pmatrix} \begin{pmatrix} 1 & 1 & J' \\ M_b' & M_a' & -M_J' \end{pmatrix} \begin{pmatrix} 1 & 1 & 2 \\ -M_a & M_a & -M \end{pmatrix} \begin{pmatrix} 1 & 1 & 2 \\ -M_b & M_b & M \end{pmatrix} .$$

Now

$$g(2, M) = \frac{4\pi}{5} \frac{4!}{(2-M)!(2+M)!} \quad (52)$$

and

$$\left\{ \begin{pmatrix} 1 & 1 & 2 \\ 1 & 1 & 1 \end{pmatrix} \right\} = \frac{1}{6} \quad (53)$$

Hence

$$\langle J' M_J' | V_5 | JM_J \rangle = \frac{54}{\pi} \left(\frac{4\pi}{5} \right) \frac{1}{36} \frac{\langle r^2 \rangle^2}{R^5} \chi(J' M_J', JM_J) \quad (54)$$

where

$$\begin{aligned}
X(J'M_J', JM_J) &= \sum_M \frac{4!}{(2-M)!(2+M)!} \sum_{M_a, M_a'} \sqrt{2J'+1} \sqrt{2J+1} \\
&\times \begin{pmatrix} 1 & 1 & J \\ M_J - M_a & M_a & -M_J \end{pmatrix} \begin{pmatrix} -M_a' + M_J' & 1 & J' \\ M_a' & -M_J' & \end{pmatrix} \\
&\times \begin{pmatrix} 1 & 1 & 2 \\ -M_a & M_a & M \end{pmatrix} \begin{pmatrix} M_J - M_a & -M_a' + M_J' & 2 \\ M & M & \end{pmatrix} .
\end{aligned} \tag{55}$$

Numerical evaluation yields

$$X(2222) = \frac{1}{5}, \quad X(2121) = -\frac{4}{5}, \quad X(2020) = \frac{6}{5} . \tag{56}$$

All other matrix elements vanish and there is no mixing between the $|J=2, M=0\rangle$ and $|J=0, M=0\rangle$ states. The element $\langle 0000 \rangle$ vanishes, and $\langle 020 \rangle$ is positive. So $|J=2, M=2\rangle$ is associated with the $2^1\Sigma_g^+$ state, and $|J=2, M=0\rangle$ with the $b^1\Sigma_g^+$ state.

The asymptotic interaction energies of the molecular states have the form $C_5 \frac{\langle r^2 \rangle^2}{R^5}$ with the values of C_5 listed in Table 6.

We now summarize the angular momentum coupling for the scattering problem. Let $\vec{\ell}$ be the angular momentum of the relative motion of the two atoms. We couple $\vec{\ell}$ to the internal angular momentum $\vec{j} = \vec{J}_a + \vec{J}_b$ of the atoms to form $J = \ell + j$. Introduce scattering wave functions with relative momentum k

$$\bar{\Psi}(\vec{k}, \vec{R}) = \sum_{JM_J \ell j} \frac{F(R; JM_J \ell j)}{R} |JM_J \ell j\rangle , \tag{57}$$

where

$$|JM_J \ell j\rangle = (-1)^{j-\ell-M_J} \sqrt{2J+1} \sum_{M_\ell M_j} \begin{pmatrix} j & \ell & J \\ M_j & M_\ell & -M_J \end{pmatrix} Y_{\ell M_\ell}(\vec{k}) |jM_j\rangle . \tag{58}$$

Table 6. Values of the Parameter C_5 .

MOLECULAR STATE	L	ATOMIC M	STATE S	C_5^{**}
<u>SINGLETs</u>				
$1\Delta_g$	2	± 2	0	6
$1\Pi_g$	2	± 1	0	-24
$1\Pi_u$	1	± 1	0	0
$1\Sigma_u$	1	0	0	0
$2^1\Sigma_g$	2	0	0	36
$b^1\Sigma_g$	0	0	0	0
<u>TRIPLETs</u>				
$3\Delta_u$	2	± 2	1	6
$3\Pi_u$	2	± 1	1	-24
$3\Pi_g$	1	± 1	1	0
$3\Sigma_g$	1	0	1	0
$2^3\Sigma_u^+$	2	0	1	36
$A^3\Sigma_u^+$	0	0	1	0
<u>QUARTETs</u>				
$5\Delta_g$	2	± 2	2	6
$5\Pi_g$	2	± 1	2	-24
$5\Pi_u$	1	± 1	2	0
$5\Sigma_u$	1	0	2	0
$2^5\Sigma_g$	2	0	2	36
$1^5\Sigma_g$	0	0	2	0

**Units of $\frac{|\langle r^6 \rangle|^2}{25}$

Following and slightly generalizing the procedures used for example by Roueff and Dalgarno,⁷⁰ we obtain for the interaction Hamiltonian in the molecular description

$$\begin{aligned}
 \langle J'M_J, \ell'j' | V | j\ell M_J J \rangle &= (-1)^{j+j'-\ell-\ell'-M_J-M_J'} \delta_{M_J M_J'} \delta_{J J'} \sqrt{2\ell+1} \sqrt{2\ell'+1} \\
 &\times \sum_M \begin{pmatrix} j' & \ell' & J \\ M & 0 & -M \end{pmatrix} \begin{pmatrix} j & \ell & J \\ M & 0 & -M \end{pmatrix} \sum_{LS} \sum_{L'S'} \sum_{M_L M_S} \sum_{M_L' M_S'} (-1)^{M+M'} \quad (59) \\
 &\times \begin{Bmatrix} L_a & S_a & J_a \\ L_b & S_b & J_b \\ L & S & j \end{Bmatrix} \begin{Bmatrix} L_a' & S_a' & J_a' \\ L_b' & S_b' & J_b' \\ L' & S' & j' \end{Bmatrix} \begin{pmatrix} L & S & j \\ M_L & M_S & -M \end{pmatrix} \begin{pmatrix} L' & S' & j' \\ M_L' & M_S' & -M' \end{pmatrix} \\
 &\times \langle L'M_L, S'M_S | H | M_S S M_L L \rangle .
 \end{aligned}$$

Various selection rules are embedded in this algebra which simplify the sets of coupled equations that have to be solved to determine the scattering matrix. We are at the state of deciding upon the best representations of the potential energy curves which enter as diagonal elements of the interaction matrix. We have obtained satisfactory representations of $X^3\Sigma_g^-$, $a^3\Pi_u$, $1^5\Pi_u$, and $1^1\Pi_u$ states and acceptable estimates of the remainder. These final results need to be tested for their sensitivity to the adopted potentials.

9. REFERENCES

1. J. W. Duff, R. L. Sundberg, J. H. Gruninger, L. S. Bernstein, D. C. Robertson, and R. J. Healey, "Description of the Strategic High-Altitude Atmospheric Radiation Code (SHARC)," GL-TR-90-0315, Geophysics Laboratory, Hanscom AFB, MA 01731 (November 1990). AD237089
2. R. D. Sharma, J. W. Duff, R. L. Sundberg, L. S. Bernstein, J. H. Gruninger, D. C. Robertson, and R. J. Healey, "Description of SHARC-2, The Strategic High-Altitude Radiance Code," Phillips Laboratory Report No. PL-TR-91-2071 (1991). ADA239008
3. Handbook of Geophysics and the Space Environment, A. S. Jursa, Ed., Air Force Geophysics Laboratory, Hanscom AFB, MA 01731 (1985); copies can be obtained from NTIS, 5285 Port Royal Road, Springfield, VA 22161, ADA167000.
4. W. T. Rawlins, "Chemistry of Vibrationally Excited Ozone in the Upper Atmosphere," J. Geophys. Res., 90, 12283-12292 (1985).
5. For example, see W. T. Rawlins, G. E. Caledonia, J. J. Gibson, and A. T. Stair, Jr., "Infrared Emission from NO ($\Delta v=1$) in an Aurora: Spectral Analysis and Kinetic Interpretation of HIRIS Measurements," J. Geophys. Res., 86, 1313 (1981).
6. R. D. Sharma, "Infrared Airglow," Progress in Atmospheric Physics, Eds. R. Rodrigo et al., Kluwer Academic Publishers (1988).
7. R. D. Sharma, A. J. Ratkowski, R. L. Sundberg, J. W. Duff, L. S. Bernstein, P. K. Acharya, J. H. Gruninger, D. C. Robertson, and R. J. Healey, "Description of SHARC, The Strategic High-Altitude Radiance Code," Geophysics Laboratory Rpt. No. GL-TR-89-0229 (August 1989). ADA213806
8. R. Sharma, A. Ratkowski, P. Acharya, L. Bernstein, J. Duff, J. Gruninger, D. Robertson, and R. Sundberg, "SHARC - An Atmospheric Model for High Altitudes (60-300 km)". Presented at the 1989 Meeting of the IRIS Targets, Backgrounds and Discrimination (February 1989).
9. R. Sharma, A. Ratkowski, J. Duff, L. Bernstein, J. Gruninger, R. Sundberg, and D. Robertson, "Current Status of SHARC - The Strategic High Altitude Radiance Code, and Description of Its New Auroral Module". Presented at the 1990 Meeting of the IRIS Targets, Backgrounds and Discrimination (January 1990).

10. R. D. Sharma, J. W. Duff, L. S. Bernstein, J. H. Gruninger, R. L. Sundberg, D. C. Robertson, and R. J. Healey, "SHARC, the Atmospheric Radiation and Transmittance Code for Altitudes from 50 to 300 km," Presented at the 1991 Meeting of the IRIS Targets, Backgrounds and Discrimination (January 1991).
11. T. C. Degges and A. P. D'Agati, "A User's Guide to the AFGL/Visidyne High Altitude Infrared Radiance Model Computer Program," Rpt. No. AFGL-TR-85-0015, Air Force Geophysics Laboratory, Hanscom AFB, MA 01731 (1984). ADA161432
12. R. L. Sundberg, D. C. Robertson, R. D. Sharma, and A. J. Ratkowski, "HAIRM-87 A High Altitude Infrared Radiance Model," Rpt. No. AFGL-TR-88-0014, Air Force Geophysics Laboratory, Hanscom AFB, MA 01731 (1988). ADA197637
13. L. S. Rothman, R. R. Gamache, A. Goldman, L. R. Brown, R. A. Toth, H. M. Pickett, R. L. Poynter, J. M. Flaud, C. Camy-Peyret, A. Barbe, N. Husson, C. P. Rinsland, and M. A. H. Smith, "The HITRAN Database: 1986 Edition," Appl. Optics, 26, 4058 (1987).
14. J. P. Winick, R. H. Picard, R. A. Joseph, R. D. Sharma, and P. P. Wintersteiner, "AARC: The Auroral Atmospheric Radiance Code," Rpt. No. AFGL-TR-87-0334, Air Force Geophysics Laboratory/OPE, Hanscom AFB, MA 01731 (November 1987). ADA202432
15. R. J. Kee, J. A. Miller, and T. H. Jefferson, "CHEMKIN: Problem-Independent, Transportable, Fortran Chemical Kinetics Code Package," Sandia Rpt. No. SAND80-8003, Sandia National Laboratory, Livermore, CA 94550 (March 1980).
16. L. S. Bernstein, "Non-Equilibrium Molecular Emission and Scattering Intensity Subroutine (NEMESIS)," AFGL-TR-88-0124, Geophysics Laboratory, Hanscom AFB, MA 01731 (April 1988). ADA199295
17. A. T. Stair, Jr., R. D. Sharma, R. M. Nadile, D. J. Baker, and W. F. Grieder, "Observations of Limb Radiance with Cryogenic spectral Infrared Rocket Experiment," J. Geophys. Res., 90, 9763 (1985)
18. S. M. Adler-Golden, M. W. Matthew, D. R. Smith, and A. J. Ratkowski, "9-12 μ m Atmospheric Ozone Emission Observed in the SPIRIT I Experiment," J. Geophys. Res., 95, 15,243 (1990)
19. P. J. Espy, C. R. Harris, A. J. Steed, J. C. Ulwick, R. H. Haycock and R. A. Straka, "Rocketborne Interferometer Measurement of Infrared Auroral Spectra," Planet. Space Sci., 36, 543 (1988)
20. F. X. Kneizys, E. P. Shettle, W. O. Gallery, J. H. Chetwynd, Jr., L. W. Abreu, J. E. A. Selby, S. A. Clough, and R. W. Fenn, Atmospheric Transmittance/Radiance: Computer Code LOWTRAN 6, AFGL-TR-83-0187 (1983). AD A137796

21. C. H. Humphrey, R. M. Nauile, C. R. Philbrick, and D. R. Smith, "Atmospheric Infrared Rad ance Variability," AFGL-TR-81-0207, Geophysics Laboratory, Hanscom AFB, MA (May 1981). ADA109928
22. A. E. Hedin, "MSIS-86 Thermospheric Model," J. Geophys. Res., 92, 4649 (1987).
23. L. G. Jacchia, "Thermospheric Temperature, Density and Composition: New Models," Special Report 375, Smithsonian Astrophysical Observatory, Harvard University, Cambridge, MA (March 1977).
24. T. J. Kenesha, S. P. Zimmerman, and C. R. Philbrick, "A Dynamic Model of the Mesosphere and Lower Thermosphere," Planet. & Space Sci., 27, 385-401 (1979).
25. J. I. Steinfeld, S. M. Adler-Golden, and J. W. Gallagher, "Critical Survey of Data on the Spectroscopy and Kinetics of Ozone in the Thermosphere," J. Phys. Chem. Ref. Data, 16, 911 (1987).
26. M. Allen, J. I. Lunine, and Y. L. Yung, "The Vertical Distribution of Ozone in the Mesosphere and Lower Thermosphere," J. Geophys. Res., 89, 4841-4872 (1984).
27. R. C. Whitten and I. G. Poppoff, Fundamentals of Aeronomy, John Wiley and Sons, Inc., New York (1971).
28. R. R. Garcia and S. Solomon, "A Numerical Model of the Zonally Averaged Dynamical and Chemical Structure of the Middle Atmosphere," J. Geophys. Res., 88, 1379-1400 (February 1983).
29. R. R. Garcia and S. Solomon, "The Effect of Breaking Gravity Waves on the Dynamics and Chemical Composition of the Mesosphere and Lower Thermosphere," J. Geophys. Res., 90, 3850-3868 (April 1985).
30. M. R. Schoeberl, D. F. Strobel, and J. P. Apruzese, "A Numerical Model of Gravity Wave Breaking and Stress in Mesosphere," J. of Geophys. Res., 88, 5249-5259 (June 1983).
31. R. S. Lindzen, "Turbulence and Stress Owing to Gravity Wave and Tidal Breakdown," J. Geophys. Res., 86, 9707-9714 (1981).
32. R. S. Lindzen and J. Forbes, "Turbulence Originating from Convectively Unstable Internal Waves," J. Geophys. Res., 88, 6549-6553 (1983).
33. J. R. Holton, "The Role of Gravity Induced Drag and Diffusion in the Momentum Budget of the Mesosphere," J. Atmos. Sci., 39, 791-799 (1982).
34. J. R. Holton, "The Influence of Gravity Wave Breaking on the General Circulation of the Middle Atmosphere," J. Atmos. Sci., 40, 2497-2507 (1983).

35. J. M. Forbes and H. B. Garrett, "Seasonal-Latitudinal Structure of the Diurnal Thermospheric Tide," J. Atmos. Sci., 35, 148-159 (1978).
36. S. Chapman and R. S. Lindzen, Atmospheric Tides, D. Reidel Publishing Company, Holland (1970).
37. J. B. Kumer, "Theory of the CO₂ 4.3 μ m Aurora and Related Phenomena," J. Geophys. Res., 82, 2203 (1977).
38. A. E. Grün, "Luminescenz-photometrische Messungen der Energieabsorption im Strahlungsfeld von Elektronenquellen Eindimensionaler Fall im Luft," Z. Naturforsch., 112a, 89-95 (1957).
39. M. H. Rees, "Auroral Ionization and Excitation by Incident Energetic Electrons," Planet. Space Sci., 111, 1209-18 (1964).
40. D. J. Strickland, J. R. Jasperse, and J. A. Whalen, "Dependence of Auroral FUV Emissions on the Incident Electron Spectrum and Neutral Atmosphere," J. Geophys. Res., 88, 8051-62 (1983).
41. O. Ashihara and K. Takayanagi, "Velocity Distribution of Ionospheric Low-Energy Electrons," Planet. Space Sci., 22, 1201 (1974).
42. G. E. Caledonia and J. P. Kennealy, "NO Infrared Radiation in the Upper Atmosphere," Planet. Space Sci., 30, 1043 (1982).
43. S. M. Adler-Golden, J. H. Gruninger, and D. R. Smith, "Derivation of Atmospheric Atomic Oxygen and Hydrogen Profiles from Ozone ν_3 Band Emission," to be published in J. Geophys. Res. (1991).
44. S. M. Adler-Golden and D. R. Smith, "Identification of 4- to 7-Quantum ν_3 Bands in the Atmospheric Recombination Spectrum of Ozone," Planet. Space Sci., 38, 1121-1132 (1990).
45. S. M. Adler-Golden, M. W. Matthew, and D. R. Smith, "Upper Atmospheric Infrared Radiance from CO₂ and NO Observed During the SPIRIT 1 Rocket Experiment," J. Geophys. Res. (in press).
46. A. Barbe, C. Secroun, and P. Jouve, "Infrared Spectra of ¹⁶O₃ and ¹⁸O₃: Darling and Dennison Resonance and Anharmonic Potential Function of Ozone," J. Mol. Spectrosc., 49, 171 (1974).
47. W. T. Rawlins and R. A. Armstrong, "Dynamics of Vibrationally Excited Ozone Formed by Three-Body Recombination. I. Spectroscopy," J. Chem. Phys., 87, 5202 (1987).
48. E. Damon, R. L. Hawkins, and J. H. Shaw, "A Spectrum of Ozone from 760 to 5800 cm⁻¹," Report RF Project 761420/711626, Interim Technical Report, The Ohio State University Research Foundation, Columbus, OH, Grant No. NSG-4749 (1981).

49. D. G. Imre, "Reaction Dynamics Studied by Photoemission Spectroscopy," Ph.D. Thesis, Massachusetts Institute of Technology (August 1984).
50. W. A. M. Blumberg and B. D. Green, private communication.
51. P. W. Tarr, D. H. Archer, and N. G. Utterback, Studies of Auroral Simulation, DNA Report No. 3297F, Defense Nuclear Agency, Washington, DC 20305 (1974).
52. "SHRIMP Stray Light Analysis," Rpt. No. 3 Telic Optics, Inc., Marlborough, MA (1990). Prepared for Spectral Sciences, Inc. 99 S. Bedford St., Burlington, MA under Contract SSI-2184-T-001.
53. D. F. Hansen and A. H. Pierson, "Design of a High-Resolution Small-Rocket Infrared Grating Spectrometer," HSS, Inc. Rpt. No. HSS-B-181 (December 1990). Prepared for Spectral Sciences, Inc., 99 S. Bedford St., Burlington, MA under Contract SSI-2184-H-001.
54. D. R. Smith, "Evidence for Off-Axis Leakage Radiance in High-Altitude IR Rocketborne Measurements," SPIE, 967 (1988).
55. R. D. Sharma, "Filling of Atmospheric Transmission Windows Due to Emission from Very High Rotation Levels of NO and O₃," Proceedings of the 1988 IRIS Study Group on Targets, Backgrounds and Discrimination, E. J. ... , P.O. Box 8618, Ann Arbor, MI 48107.
56. R. D. Sharma, P. M. Bakshi, and J. M. Sindoni, "Criteria for Applicability of the Impulse Approach to Collisions," Phys. Rev. A, 41, 6540 (1990).
57. R. D. Sharma, P. M. Bakshi, and J. M. Sindoni, "Impulse formalism for atom-diatom collisions," Phys. Rev. A, 43, 189 (1991).
58. G. F. Chew, "The Inelastic Scattering of High Energy Neutrons by Deuterons According to the Impulse Approximation," Phys. Rev., 80, 196 (1950).
59. A. Bogan, "Impulse Approximation for Three-dimensional Inelastic Atom-diatom-molecule Collisions," Phys. Rev. A, 9, 1230 (1974).
60. P. Eckelt, H. J. Korsch, and V. Philipp, "Energy Loss Spectra for Vibro-rotational Molecular Excitation in an Impulsive Spectator Model," J. Phys. B, 7, 1649 (1974).
61. H. J. Korsch and V. Philipp, "Quantum-mechanical Impulse Approximation for Vibro-rotational Excitation in Atom-diatom Collisions," Phys. Rev. A, 13, 497 (1976).

62. V. Philipp, H. J. Korsch, and P. Eckelt, "Inelastic Atom-diatom-molecule Collisions I. Influence of Mass Asymmetry of Heteronuclear Molecules," J. Phys. B, 9, 2345 (1976).
63. V. Philipp, H. J. Korsch, and P. Eckelt, "Inelastic Atom-diatom-molecule Collision II. Influence of Initial Vibrational and Rotational Excitation." J. Phys. B, 10, 117 (1977).
64. L. H. Beard and D. A. Micha, "Collisional Dynamics of Three Interacting Atoms: Vibrational-Rotational Excitation in Atom-Diatom Hyperthermal Collisions," J. Chem. Phys., 74, 6700 (1981).
65. J. M. J. Van Leeuwen and A. S. Reiner, "On the Calculation of the T-matrix for Potentials With a Hard Core," Physica, 27, 99 (1961).
66. D. C. S. Allison and P. G. Burke, "Inelastic Collisions of Slow Atoms," J. Phys. B, 2, 941 (1969).
67. J. K. Knipp, "Quadrupole-quadrupole Interatomic Forces," Phys. Rev., 53, 734 (1939).
68. T. Y. Chang, "Moderately Long-range Interatomic Forces," Rev. Mod. Phys., 39, 911 (1967).
69. S. J. A. Uminskij and E. E. Nikitin, "Electronic Wave Functions and States of Diatomic Molecules at Long Atomic Distances," Theoret. Chem. Acta, 13, 91 (1969).
70. E. Roueff and A. Dalgarno, "Fine-structure Excitation of O^{2+} by Charge Transfer of O^{3+} in H at High Energies," Phys. Rev. A, 38, 93 (1988).

APPENDIX A

SHARC CHEMICAL KINETICS SCHEME

The current version of SHARC-2 contains chemical kinetics/reaction mechanisms for ambient infrared radiance from CO₂, O₃, NO, H₂O, and CO. The original SHARC radiation (i.e., chemical kinetics mechanisms and associated rate constants) mechanisms were based on those used in the HAIRM code.^{A1} In order to be consistent with limited SHARC and field data comparisons, as well as recent laboratory measurements, the mechanisms and associated rate constants from the HAIRM code have been extensively revised.

In the following sections, the vibrational excitation/deexcitation mechanisms and radiative relaxation processes are listed. The species M represents N₂ and O₂, while M' represents N₂, O₂, and O. Also included in the tables (Tables A1-A5) are the rate constants associated with the kinetics mechanisms, as currently used in SHARC. When available, references for the rate constants in each Table are also provided. Much of the work on rate constant measurements prior to 1974 (and to a lesser extent calculations) has been reviewed by Taylor.^{A2}

REFERENCES

- A1. T. C. Degges and A. P. D'Agati, "A User's Guide to the AFGL/Visidyne High Altitude Infrared Radiance Model Computer Program," AFGL-TR-85-0015, Air Force Geophysics Laboratory, Hanscom AFB, MA 01731 (1984). ADA161432
- A2. R. L. Taylor, "Energy Transfer Processes in the Stratosphere," Can. J. Chem., 52, 1436 (1974) and references therein.

TABLE A1. REACTIONS AND RATE CONSTANTS FOR CO₂ MODEL.

Reaction	Rate Constant*	Reference
CO ₂ (01101) + M = CO ₂ (00001) + M	1.50x10 ⁻²² T ³	a
CO ₂ (01101) + O = CO ₂ (00001) + O	1.00x10 ⁻¹³ T ^{1/2}	b
CO ₂ (10002) + M = CO ₂ (01101) + M	3.00x10 ⁻²² T ³	c,d
CO ₂ (10002) + O = CO ₂ (01101) + O	2.00x10 ⁻¹³ T ^{1/2}	c,d
CO ₂ (02201) + M = CO ₂ (01101) + M	6.00x10 ⁻²² T ³	c
CO ₂ (02201) + O = CO ₂ (01101) + O	4.00x10 ⁻¹³ T ^{1/2}	c
CO ₂ (10001) + M = CO ₂ (01101) + M	3.00x10 ⁻²² T ³	c,d
CO ₂ (10001) + O = CO ₂ (01101) + O	2.00x10 ⁻¹³ T ^{1/2}	c,d
CO ₂ (02201) + M = CO ₂ (10002) + M	2.90x10 ⁻¹³	e
CO ₂ (10001) + M = CO ₂ (02201) + M	5.80x10 ⁻¹³	e
CO ₂ (10001) + M = CO ₂ (10002) + M	1.70x10 ⁻¹³	e
CO ₂ (11102) + M = CO ₂ (10002) + M	1.50x10 ⁻²² T ³	c,d
CO ₂ (11102) + O = CO ₂ (10002) + O	1.00x10 ⁻¹³ T ^{1/2}	c,d
CO ₂ (11102) + M = CO ₂ (02201) + M	3.00x10 ⁻²² T ³	c,d
CO ₂ (11102) + O = CO ₂ (02201) + O	2.00x10 ⁻¹³ T ^{1/2}	c,d
CO ₂ (11102) + M = CO ₂ (10001) + M	1.50x10 ⁻²² T ³	c,d
CO ₂ (11102) + O = CO ₂ (10001) + O	1.00x10 ⁻¹³ T ^{1/2}	c,d
CO ₂ (03301) + M = CO ₂ (10002) + M	4.50x10 ⁻²² T ³	c,d
CO ₂ (03301) + O = CO ₂ (10002) + O	3.00x10 ⁻¹³ T ^{1/2}	c,d
CO ₂ (03301) + M = CO ₂ (02201) + M	9.00x10 ⁻²² T ³	c,d
CO ₂ (03301) + O = CO ₂ (02201) + O	6.00x10 ⁻¹³ T ^{1/2}	c,d
CO ₂ (03301) + M = CO ₂ (10001) + M	4.50x10 ⁻²² T ³	c,d
CO ₂ (03301) + O = CO ₂ (10001) + O	3.00x10 ⁻¹³ T ^{1/2}	c,d
CO ₂ (11101) + M = CO ₂ (10002) + M	1.50x10 ⁻²² T ³	c,d
CO ₂ (11101) + O = CO ₂ (10002) + O	1.00x10 ⁻¹³ T ^{1/2}	c,d
CO ₂ (11101) + M = CO ₂ (02201) + M	3.00x10 ⁻²² T ³	c,d
CO ₂ (11101) + O = CO ₂ (02201) + O	2.00x10 ⁻¹³ T ^{1/2}	c,d
CO ₂ (11101) + M = CO ₂ (10001) + M	1.50x10 ⁻²² T ³	c,d
CO ₂ (11101) + O = CO ₂ (10001) + O	1.00x10 ⁻¹³ T ^{1/2}	c,d

TABLE A1. (CONTINUED)

Reaction	Rate Constant*	Reference
$\text{CO}_2(03301) + \text{M} = \text{CO}_2(11102) + \text{M}$	2.90×10^{-13}	f
$\text{CO}_2(11101) + \text{M} = \text{CO}_2(11102) + \text{M}$	1.70×10^{-13}	f
$\text{CO}_2(11101) + \text{M} = \text{CO}_2(03301) + \text{M}$	2.90×10^{-13}	f
$\text{CO}_2(00011) + \text{M} = \text{CO}_2(03301) + \text{M}$	$1.00 \times 10^{-15} + 5.16 \times 10^{-11} e^{-76.75/T^{1/3}}$	g
$\text{CO}_2(00011) + \text{O} = \text{CO}_2(03301) + \text{O}$	$1.10 \times 10^{-13} T^{1/2}$	h
$\text{CO}_2(00011) + \text{M} = \text{CO}_2(11102) + \text{M}$	$1.00 \times 10^{-15} + 5.16 \times 10^{-11} e^{-76.75/T^{1/3}}$	d
$\text{CO}_2(00011) + \text{M} = \text{CO}_2(11101) + \text{M}$	$1.00 \times 10^{-15} + 5.16 \times 10^{-11} e^{-76.75/T^{1/3}}$	d
$\text{CO}_2(20003) + \text{M} = \text{CO}_2(03301) + \text{M}$	$1.20 \times 10^{-21} T^3$	c,d
$\text{CO}_2(20003) + \text{O} = \text{CO}_2(03301) + \text{O}$	$8.00 \times 10^{-13} T^{1/2}$	c,d
$\text{CO}_2(12202) + \text{M} = \text{CO}_2(03301) + \text{M}$	$1.20 \times 10^{-21} T^3$	c,d
$\text{CO}_2(12202) + \text{O} = \text{CO}_2(03301) + \text{O}$	$8.00 \times 10^{-13} T^{1/2}$	c,d
$\text{CO}_2(20002) + \text{M} = \text{CO}_2(03301) + \text{M}$	$1.20 \times 10^{-21} T^3$	c,d
$\text{CO}_2(20002) + \text{O} = \text{CO}_2(03301) + \text{O}$	$8.00 \times 10^{-13} T^{1/2}$	c,d
$\text{CO}_2(04401) + \text{M} = \text{CO}_2(03301) + \text{M}$	$1.20 \times 10^{-21} T^3$	c,d
$\text{CO}_2(04401) + \text{O} = \text{CO}_2(03301) + \text{O}$	$8.00 \times 10^{-13} T^{1/2}$	c,d
$\text{CO}_2(12201) + \text{M} = \text{CO}_2(03301) + \text{M}$	$1.20 \times 10^{-21} T^3$	c,d
$\text{CO}_2(12201) + \text{O} = \text{CO}_2(03301) + \text{O}$	$8.00 \times 10^{-13} T^{1/2}$	c,d
$\text{CO}_2(20001) + \text{M} = \text{CO}_2(03301) + \text{M}$	$1.20 \times 10^{-21} T^3$	c,d
$\text{CO}_2(20001) + \text{O} = \text{CO}_2(03301) + \text{O}$	$8.00 \times 10^{-13} T^{1/2}$	c,d
$\text{CO}_2(01111) + \text{M} = \text{CO}_2(00011) + \text{M}$	$1.50 \times 10^{-22} T^3$	c,d
$\text{CO}_2(01111) + \text{O} = \text{CO}_2(00011) + \text{O}$	$1.00 \times 10^{-13} T^{1/2}$	c,d
$\text{CO}_2(20003) + \text{M} = \text{CO}_2(00011) + \text{M}$	$5.00 \times 10^{-16} + 2.58 \times 10^{-11} e^{-76.75/T^{1/3}}$	i
$\text{CO}_2(12202) + \text{M} = \text{CO}_2(00011) + \text{M}$	$1.00 \times 10^{-15} + 5.16 \times 10^{-11} e^{-76.75/T^{1/3}}$	i
$\text{CO}_2(20002) + \text{M} = \text{CO}_2(00011) + \text{M}$	$1.00 \times 10^{-15} + 5.16 \times 10^{-11} e^{-76.75/T^{1/3}}$	i

TABLE A1. (CONTINUED)

Reaction	Rate Constant*	Reference
$\text{CO}_2(04401) + \text{M} = \text{CO}_2(00011) + \text{M}$	$1.00 \times 10^{-15} + 5.16 \times 10^{-11} e^{-76.75/T^{1/3}}$	i
$\text{CO}_2(20001) + \text{M} = \text{CO}_2(00011) + \text{M}$	$5.00 \times 10^{-16} + 2.58 \times 10^{-11} e^{-76.75/T^{1/3}}$	i
$\text{CO}_2(12201) + \text{M} = \text{CO}_2(00011) + \text{M}$	$1.00 \times 10^{-15} + 5.16 \times 10^{-11} e^{-76.75/T^{1/3}}$	i
$\text{CO}_2(04401) + \text{M} = \text{CO}_2(20003) + \text{M}$	2.90×10^{-13}	f
$\text{CO}_2(04401) + \text{M} = \text{CO}_2(20002) + \text{M}$	2.90×10^{-13}	f
$\text{CO}_2(20001) + \text{M} = \text{CO}_2(04401) + \text{M}$	5.80×10^{-13}	f
$\text{CO}_2(04401) + \text{M} = \text{CO}_2(12202) + \text{M}$	2.90×10^{-13}	f
$\text{CO}_2(12201) + \text{M} = \text{CO}_2(04401) + \text{M}$	2.90×10^{-13}	f
$\text{CO}_2(12201) + \text{M} = \text{CO}_2(12202) + \text{M}$	1.70×10^{-13}	f
$\text{CO}_2(20002) + \text{M} = \text{CO}_2(20003) + \text{M}$	1.70×10^{-13}	f
$\text{CO}_2(20001) + \text{M} = \text{CO}_2(20003) + \text{M}$	1.70×10^{-13}	f
$\text{CO}_2(20001) + \text{M} = \text{CO}_2(20002) + \text{M}$	1.70×10^{-13}	f
$\text{CO}_2(02211) + \text{M} = \text{CO}_2(10012) + \text{M}$	2.90×10^{-13}	f
$\text{CO}_2(10011) + \text{M} = \text{CO}_2(02211) + \text{M}$	5.80×10^{-13}	f
$\text{CO}_2(10011) + \text{M} = \text{CO}_2(10012) + \text{M}$	1.70×10^{-13}	f
$\text{CO}_2(03311) + \text{M} = \text{CO}_2(11112) + \text{M}$	2.90×10^{-13}	f
$\text{CO}_2(11111) + \text{M} = \text{CO}_2(03311) + \text{M}$	2.90×10^{-13}	f
$\text{CO}_2(11111) + \text{M} = \text{CO}_2(11112) + \text{M}$	1.70×10^{-13}	f
$\text{CO}_2(04411) + \text{M} = \text{CO}_2(20013) + \text{M}$	2.90×10^{-13}	f
$\text{CO}_2(20012) + \text{M} = \text{CO}_2(04411) + \text{M}$	5.80×10^{-13}	f
$\text{CO}_2(20011) + \text{M} = \text{CO}_2(04411) + \text{M}$	5.80×10^{-13}	f
$\text{CO}_2(20012) + \text{M} = \text{CO}_2(20013) + \text{M}$	1.70×10^{-13}	f
$\text{CO}_2(20011) + \text{M} = \text{CO}_2(20012) + \text{M}$	1.70×10^{-13}	f
$\text{CO}_2(20011) + \text{M} = \text{CO}_2(20013) + \text{M}$	1.70×10^{-13}	f
$\text{CO}_2(00011) + \text{N}_2(0) = \text{CO}_2(00001) + \text{N}_2(1)$	$8.91 \times 10^{-12}/T^{1/2}$	g
$\text{CO}_2(01111) + \text{N}_2(0) = \text{CO}_2(01101) + \text{N}_2(1)$	$8.91 \times 10^{-12}/T^{1/2}$	j
$\text{CO}_2(10012) + \text{N}_2(0) = \text{CO}_2(10002) + \text{N}_2(1)$	$8.91 \times 10^{-12}/T^{1/2}$	j

TABLE A1. (CONTINUED)

Reaction	Rate Constant*	Reference
$\text{CO}_2(02211) + \text{N}_2(0) = \text{CO}_2(02201) + \text{N}_2(1)$	$8.91 \times 10^{-12} / T^{1/2}$	j
$\text{CO}_2(10011) + \text{N}_2(0) = \text{CO}_2(10001) + \text{N}_2(1)$	$8.91 \times 10^{-12} / T^{1/2}$	j
$\text{CO}_2(11112) + \text{N}_2(0) = \text{CO}_2(11102) + \text{N}_2(1)$	$8.91 \times 10^{-12} / T^{1/2}$	j
$\text{CO}_2(03311) + \text{N}_2(0) = \text{CO}_2(03301) + \text{N}_2(1)$	$8.91 \times 10^{-12} / T^{1/2}$	j
$\text{CO}_2(11111) + \text{N}_2(0) = \text{CO}_2(11101) + \text{N}_2(1)$	$8.91 \times 10^{-12} / T^{1/2}$	j
$\text{CO}_2(20013) + \text{N}_2(0) = \text{CO}_2(20003) + \text{N}_2(1)$	$8.91 \times 10^{-12} / T^{1/2}$	j
$\text{CO}_2(04411) + \text{N}_2(0) = \text{CO}_2(04401) + \text{N}_2(1)$	$8.91 \times 10^{-12} / T^{1/2}$	j
$\text{CO}_2(20012) + \text{N}_2(0) = \text{CO}_2(20002) + \text{N}_2(1)$	$8.91 \times 10^{-12} / T^{1/2}$	j
$\text{CO}_2(20011) + \text{N}_2(0) = \text{CO}_2(20001) + \text{N}_2(1)$	$8.91 \times 10^{-12} / T^{1/2}$	j
$\text{CO}_2(01101) \rightarrow \text{CO}_2(00001) + h\nu$	1.50	k
$\text{CO}_2(11102) \rightarrow \text{CO}_2(00001) + h\nu$	0.001	k
$\text{CO}_2(11101) \rightarrow \text{CO}_2(00001) + h\nu$	0.010	k
$\text{CO}_2(00011) \rightarrow \text{CO}_2(00001) + h\nu$	432.95	k
$\text{CO}_2(10012) \rightarrow \text{CO}_2(00001) + h\nu$	11.15	k
$\text{CO}_2(10011) \rightarrow \text{CO}_2(00001) + h\nu$	17.92	k
$\text{CO}_2(20013) \rightarrow \text{CO}_2(00001) + h\nu$	0.150	k
$\text{CO}_2(20012) \rightarrow \text{CO}_2(00001) + h\nu$	0.718	k
$\text{CO}_2(20011) \rightarrow \text{CO}_2(00001) + h\nu$	0.233	k
$\text{CO}_2(10002) \rightarrow \text{CO}_2(01101) + h\nu$	1.15	k
$\text{CO}_2(02201) \rightarrow \text{CO}_2(01101) + h\nu$	3.03	k
$\text{CO}_2(10001) \rightarrow \text{CO}_2(01101) + h\nu$	1.57	k
$\text{CO}_2(01111) \rightarrow \text{CO}_2(01101) + h\nu$	423.35	k
$\text{CO}_2(11112) \rightarrow \text{CO}_2(01101) + h\nu$	10.52	k
$\text{CO}_2(11111) \rightarrow \text{CO}_2(01101) + h\nu$	18.55	k
$\text{CO}_2(11102) \rightarrow \text{CO}_2(10002) + h\nu$	1.96	k
$\text{CO}_2(11101) \rightarrow \text{CO}_2(10002) + h\nu$	0.117	k
$\text{CO}_2(00011) \rightarrow \text{CO}_2(10002) + h\nu$	0.467	k
$\text{CO}_2(10012) \rightarrow \text{CO}_2(10002) + h\nu$	411.14	k
$\text{CO}_2(20013) \rightarrow \text{CO}_2(10002) + h\nu$	17.18	k

TABLE A1. (CONTINUED)

Reaction	Rate Constant*	Reference
CO ₂ (20012) → CO ₂ (10002) + hν	22.28	k
CO ₂ (11102) → CO ₂ (02201) + hν	0.500	k
CO ₂ (03301) → CO ₂ (02201) + hν	4.58	k
CO ₂ (11101) → CO ₂ (02201) + hν	1.17	k
CO ₂ (02211) → CO ₂ (02201) + hν	414.50	k
CO ₂ (11102) → CO ₂ (10001) + hν	0.028	k
CO ₂ (11101) → CO ₂ (10001) + hν	2.46	k
CO ₂ (00011) → CO ₂ (10001) + hν	0.442	k
CO ₂ (10011) → CO ₂ (10001) + hν	408.85	k
CO ₂ (20012) → CO ₂ (10001) + hν	14.99	k
CO ₂ (20011) → CO ₂ (10001) + hν	30.06	k
CO ₂ (11112) → CO ₂ (11102) + hν	404.14	k
CO ₂ (03311) → CO ₂ (03301) + hν	408.56	k
CO ₂ (11111) → CO ₂ (11101) + hν	400.33	k

* Rate constants are in units of 1/s for unimolecular reactions, cm³/molecule-s for bimolecular reactions and cm⁶/molecule-s for termolecular reactions.

a S. L. Lunt, C. T. Wickham-Jones, and C. J. S. M. Simpson, "Rate Constants for the Deactivation of the 15 μm Band of Carbon Dioxide by the Collision Partners CH₃F, CO₂, N₂, Ar and Kr over the Temperature Range 300 to 150 K," Chem. Phys. Letters, **115**, 60 (1985). C. J. S. M. Simpson, T. R. D. Chandler, "A Shock Tube Study of Vibrational Relaxation in Pure CO₂ and Mixtures of CO₂ with the Inert Gases, Nitrogen, Deuterium and Hydrogen," Proc. Roy. Soc. Lond. A., **317**, 265 (1970).

b The value of the deexcitation rate constant given here is approximately a factor of three lower than that reported by R. D. Sharma and P. P. Wintersteiner, "Role of Carbon Dioxide in Cooling Planetary Thermospheres," Geophys. Res. Letters, **17**, 2201 (1990). R. E. Center, "Vibrational Relaxation of CO₂ by O Atoms," J. Chem. Phys., **59**, 3523 (1973).

c Estimate based on SSH theory, $k_{n_1 n_2 l n_3 x \rightarrow n_1 n_2 - 1 l - n_3 x} = g_{n_1 n_2 - 1 l - n_3 x} n_2^2 k_{01101 \rightarrow 00001}$.

- d Deexcitation rate constants for Fermi coupled states are assumed to be equal.
- e C. Dang, J. Reid, and B. K. Garside, "Dynamics of the CO₂ Lower Laser Levels as Measured with a Tunable Diode Laser," Appl. Phys. B, 31, 163 (1983).
- f Estimate based on $k_{n_1+1n_2ln_3x \rightarrow n_1n_2+2l+2n_3x'} = k_{1000x \rightarrow 0220x'}$, or $k_{n_1n_2ln_3x \rightarrow n_1n_2ln_3x'} = k_{1000x \rightarrow 1000x'}$.
- g W. A. Rosser, Jr., A. D. Wood, and E. T. Gerry, "Deactivation of Vibrationally Excited Carbon Dioxide (ν_3) by Collisions with Carbon Dioxide or with Nitrogen," J. Chem. Phys., 50, 4996 (1969).
- h J. H. W. Cramp and J. D. Lambert, "Vibrational Relaxation of CO₂(ν_3) by O Atoms," Chem. Phys. Letters, 22, 146 (1973).
- i Estimate based on $k_{00011 \rightarrow n_1n_2ln_3x'} = k_{00011 \rightarrow 03301} e^{-\Delta E/kT}$.
- j Estimate based on $k_{n_1n_2ln_3x \rightarrow n_1n_2ln_3-1x} = k_{00011 \rightarrow 00001}$.
- k L. S. Rothman, et al., "The HITRAN Database: 1986 Edition," Appl. Opt., 26, 4058 (1987).

TABLE A2. REACTIONS AND RATE CONSTANTS FOR O₃ MODEL.

Reaction	Rate Constant*	Reference
$O + O_2 + M \rightarrow O_3(000) + M$	$2.79 \times 10^{-35} e^{510.0/T}$	a,b
$O + O_2 + M \rightarrow O_3(001) + M$	$2.35 \times 10^{-35} e^{510.0/T}$	a,b
$O + O_2 + M \rightarrow O_3(002) + M$	$1.85 \times 10^{-35} e^{510.0/T}$	a,b
$O + O_2 + M \rightarrow O_3(003) + M$	$1.42 \times 10^{-35} e^{510.0/T}$	a,b
$O + O_2 + M \rightarrow O_3(004) + M$	$1.06 \times 10^{-35} e^{510.0/T}$	a,b
$O + O_2 + M \rightarrow O_3(005) + M$	$7.59 \times 10^{-36} e^{510.0/T}$	a,b
$O + O_2 + M \rightarrow O_3(006) + M$	$4.73 \times 10^{-36} e^{510.0/T}$	a,b
$O + O_2 + M \rightarrow O_3(007) + M$	$2.53 \times 10^{-36} e^{510.0/T}$	a,b
$O + O_2 + M \rightarrow O_3(008) + M$	$8.80 \times 10^{-37} e^{510.0/T}$	a,b
$O + O_2 + M \rightarrow O_3(009) + M$	$2.20 \times 10^{-37} e^{510.0/T}$	a,b
$O_3(010) + M \rightleftharpoons O_3(000) + M$	$1.73 \times 10^{-15} T^{1/2}$	c
$O_3(010) + O \rightleftharpoons O_3(000) + O$	$1.73 \times 10^{-13} T^{1/2}$	d
$O_3(020) + M \rightleftharpoons O_3(010) + M$	$3.46 \times 10^{-15} T^{1/2}$	e
$O_3(020) + O \rightleftharpoons O_3(010) + O$	$3.46 \times 10^{-13} T^{1/2}$	e
$O_3(100) + M \rightleftharpoons O_3(010) + M$	$2.89 \times 10^{-15} T^{1/2}$	c
$O_3(100) + O \rightleftharpoons O_3(010) + O$	$5.20 \times 10^{-13} T^{1/2}$	d
$O_3(100) + M' \rightleftharpoons O_3(001) + M'$	1.00×10^{-11}	b,c
$O_3(200) + M \rightleftharpoons O_3(100) + M$	$5.80 \times 10^{-15} T^{1/2}$	e
$O_3(200) + O \rightleftharpoons O_3(100) + O$	$1.04 \times 10^{-12} T^{1/2}$	e
$O_3(200) + M' \rightleftharpoons O_3(101) + M'$	1.00×10^{-11}	f
$O_3(001) + M \rightleftharpoons O_3(010) + M$	$2.89 \times 10^{-15} T^{1/2}$	c
$O_3(001) + O \rightleftharpoons O_3(010) + O$	$5.20 \times 10^{-13} T^{1/2}$	d
$O_3(002) + M \rightleftharpoons O_3(001) + M$	$5.80 \times 10^{-15} T^{1/2}$	e
$O_3(002) + O \rightleftharpoons O_3(001) + O$	$1.04 \times 10^{-12} T^{1/2}$	e
$O_3(003) + M \rightleftharpoons O_3(002) + M$	$8.70 \times 10^{-15} T^{1/2}$	e
$O_3(003) + O \rightleftharpoons O_3(002) + O$	$1.56 \times 10^{-12} T^{1/2}$	e
$O_3(004) + M \rightleftharpoons O_3(003) + M$	$1.16 \times 10^{-14} T^{1/2}$	e
$O_3(004) + O \rightleftharpoons O_3(003) + O$	$2.08 \times 10^{-12} T^{1/2}$	e
$O_3(005) + M \rightleftharpoons O_3(004) + M$	$1.45 \times 10^{-14} T^{1/2}$	e

TABLE A2. (CONTINUED)

Reaction	Rate Constant*	Reference
$O_3(005) + O \rightleftharpoons O_3(004) + O$	$2.60 \times 10^{-12} T^{1/2}$	e
$O_3(006) + M \rightleftharpoons O_3(005) + M$	$1.74 \times 10^{-14} T^{1/2}$	e
$O_3(006) + O \rightleftharpoons O_3(005) + O$	$3.12 \times 10^{-12} T^{1/2}$	e
$O_3(007) + M \rightleftharpoons O_3(006) + M$	$2.03 \times 10^{-14} T^{1/2}$	e
$O_3(007) + O \rightleftharpoons O_3(006) + O$	$3.64 \times 10^{-12} T^{1/2}$	e
$O_3(008) + M \rightleftharpoons O_3(007) + M$	$2.32 \times 10^{-14} T^{1/2}$	e
$O_3(008) + O \rightleftharpoons O_3(007) + O$	$4.16 \times 10^{-12} T^{1/2}$	e
$O_3(009) + M \rightleftharpoons O_3(008) + M$	$2.61 \times 10^{-14} T^{1/2}$	e
$O_3(009) + O \rightleftharpoons O_3(008) + O$	$4.68 \times 10^{-12} T^{1/2}$	e
$O_3(001) + O \rightarrow O_2 + O_2$	1.00×10^{-11}	b,d
$O_3(002) + O \rightarrow O_2 + O_2$	1.00×10^{-11}	b,d
$O_3(003) + O \rightarrow O_2 + O_2$	1.00×10^{-11}	b,d
$O_3(004) + O \rightarrow O_2 + O_2$	1.00×10^{-11}	b,d
$O_3(005) + O \rightarrow O_2 + O_2$	1.00×10^{-11}	b,d
$O_3(006) + O \rightarrow O_2 + O_2$	1.00×10^{-11}	b,d
$O_3(007) + O \rightarrow O_2 + O_2$	1.00×10^{-11}	b,d
$O_3(008) + O \rightarrow O_2 + O_2$	1.00×10^{-11}	b,d
$O_3(009) + O \rightarrow O_2 + O_2$	1.00×10^{-11}	b,d
$O_3(011) + M \rightleftharpoons O_3(010) + M$	$2.89 \times 10^{-15} T^{1/2}$	g
$O_3(011) + O \rightleftharpoons O_3(010) + O$	$5.20 \times 10^{-13} T^{1/2}$	g
$O_3(011) + M \rightleftharpoons O_3(001) + M$	$1.73 \times 10^{-15} T^{1/2}$	g
$O_3(011) + O \rightleftharpoons O_3(001) + O$	$1.73 \times 10^{-13} T^{1/2}$	g
$O_3(110) + M \rightleftharpoons O_3(010) + M$	$2.89 \times 10^{-15} T^{1/2}$	g
$O_3(110) + O \rightleftharpoons O_3(010) + O$	$5.20 \times 10^{-13} T^{1/2}$	g
$O_3(110) + M \rightleftharpoons O_3(100) + M$	$1.73 \times 10^{-15} T^{1/2}$	g
$O_3(110) + O \rightleftharpoons O_3(100) + O$	$1.73 \times 10^{-13} T^{1/2}$	g
$O_3(101) + M \rightleftharpoons O_3(001) + M$	$2.89 \times 10^{-15} T^{1/2}$	g
$O_3(101) + O \rightleftharpoons O_3(001) + O$	$5.20 \times 10^{-13} T^{1/2}$	g
$O_3(101) + M \rightleftharpoons O_3(100) + M$	$2.89 \times 10^{-15} T^{1/2}$	g

TABLE A2. (CONTINUED)

Reaction	Rate Constant*	Reference
$O_3(101) + O \rightleftharpoons O_3(100) + O$	$5.20 \times 10^{-13} T^{1/2}$	g
$O_3(101) + M' \rightleftharpoons O_3(002) + M'$	1.00×10^{-11}	f
$O_3(111) + M \rightleftharpoons O_3(101) + M$	$1.73 \times 10^{-15} T^{1/2}$	g
$O_3(111) + O \rightleftharpoons O_3(101) + O$	$1.73 \times 10^{-13} T^{1/2}$	g
$O_3(111) + M \rightleftharpoons O_3(011) + M$	$2.89 \times 10^{-15} T^{1/2}$	g
$O_3(111) + O \rightleftharpoons O_3(011) + O$	$5.20 \times 10^{-13} T^{1/2}$	g
$O_3(111) + M \rightleftharpoons O_3(110) + M$	$2.89 \times 10^{-15} T^{1/2}$	g
$O_3(111) + O \rightleftharpoons O_3(110) + O$	$5.20 \times 10^{-13} T^{1/2}$	g
$O_3(010) \rightarrow O_3(000) + h\nu$	0.224	h
$O_3(001) \rightarrow O_3(000) + h\nu$	11.00	h
$O_3(100) \rightarrow O_3(000) + h\nu$	0.594	h
$O_3(011) \rightarrow O_3(000) + h\nu$	0.116	h
$O_3(110) \rightarrow O_3(000) + h\nu$	0.053	h
$O_3(002) \rightarrow O_3(000) + h\nu$	0.342	h
$O_3(101) \rightarrow O_3(000) + h\nu$	3.67	h
$O_3(200) \rightarrow O_3(000) + h\nu$	0.106	h
$O_3(111) \rightarrow O_3(000) + h\nu$	0.131	h
$O_3(003) \rightarrow O_3(000) + h\nu$	0.746	h
$O_3(020) \rightarrow O_3(010) + h\nu$	0.446	h
$O_3(011) \rightarrow O_3(010) + h\nu$	10.39	h
$O_3(110) \rightarrow O_3(010) + h\nu$	0.291	h
$O_3(111) \rightarrow O_3(010) + h\nu$	3.67	h
$O_3(002) \rightarrow O_3(001) + h\nu$	20.72	h
$O_3(101) \rightarrow O_3(001) + h\nu$	0.437	h
$O_3(111) \rightarrow O_3(001) + h\nu$	0.053	h
$O_3(003) \rightarrow O_3(001) + h\nu$	1.03	h
$O_3(101) \rightarrow O_3(100) + h\nu$	9.68	h
$O_3(200) \rightarrow O_3(100) + h\nu$	1.18	h
$O_3(111) \rightarrow O_3(100) + h\nu$	0.116	h

TABLE A2. (CONTINUED)

Reaction	Rate Constant*	Reference
$O_3(111) \rightarrow O_3(011) + h\nu$	0.593	h
$O_3(111) \rightarrow O_3(110) + h\nu$	11.01	h
$O_3(003) \rightarrow O_3(002) + h\nu$	30.44	h
$O_3(004) \rightarrow O_3(003) + h\nu$	36.34	h
$O_3(005) \rightarrow O_3(004) + h\nu$	43.08	h
$O_3(006) \rightarrow O_3(005) + h\nu$	48.49	h
$O_3(007) \rightarrow O_3(006) + h\nu$	52.71	h
$O_3(008) \rightarrow O_3(007) + h\nu$	56.12	h
$O_3(009) \rightarrow O_3(008) + h\nu$	58.67	h

* Rate constants are in units of 1/s for unimolecular reactions, $cm^3/molecule\cdot s$ for bimolecular reactions and $cm^6/molecule\cdot s$ for termolecular reactions.

a R.E. Huie, J.T. Herron, and D.D. Davis, "Absolute Rate Constants for the Reaction of $O+O_2+M \rightarrow O_3+M$ over the Temperature Range 200-346 K," J. Phys. Chem., **76**, 2653 (1972).

b W.T. Rawlins, "Chemistry of Vibrationally Excited Ozone in the Upper Atmosphere," J. Geophys. Res., **90**, 12283 (1985).

c S.M. Adler-Golden and J.I. Steinfeld, "Vibrational Energy Transfer in Ozone by Infrared-Ultraviolet Double Resonance," Chem. Phys. Letters, **76**, 479 (1980).

d G.A. West, R.E. Weston, Jr., and G.W. Flynn, "Deactivation of Vibrationally Excited ozone by $O(^3P)$ Atoms," Chem. Phys. Lett., **42**, 488 (1976).

e Estimate based on SSH theory, $k_{n \rightarrow n-1} = nk_{1 \rightarrow 0}$.

f Estimate based on $k_{lmn \rightarrow l-1mn+1} = k_{100 \rightarrow 001}$.

g Estimate based on $k_{lmn \rightarrow lm-1n} = k_{010 \rightarrow 000}$, $k_{lmn \rightarrow l-1mn} = k_{100 \rightarrow 000}$, or $k_{lmn \rightarrow lmn-1} = k_{001 \rightarrow 000}$.

h L. S. Rothman, et al., "The HITRAN Database: 1986 Edition," Appl. Opt., **26**, 4058 (1987).

TABLE A3. REACTIONS AND RATE CONSTANTS FOR NO MODEL.

Reaction	Rate Constant*	Reference
NO(1) + O ₂ = NO(0) + O ₂	2.6x10 ⁻¹⁴	a
NO(2) + O ₂ = NO(1) + O ₂	6.6x10 ⁻¹⁴	a
NO(1) + O = NO(0) + O	6.5x10 ⁻¹¹	b
NO(2) + O = NO(1) + O	2.17x10 ⁻¹¹	c
NO(2) + O = NO(0) + O	4.33x10 ⁻¹¹	c
NO(1) → NO(0) + hν	13.30	d
NO(2) → NO(1) + hν	25.43	d
NO(2) → NO(0) + hν	0.857	d

* Rate constants are in units of cm³/molecule-sec for bimolecular processes and 1/sec for the Einstein A coefficients.

a B. D. Green, B. E. Caledonia, R. E. Murphy, and F. X. Robert, "The Vibrational Relaxation of NO(v=1-7) by O₂," J. Chem. Phys., **76**, 2441 (1982).

b R. P. Fernando and I. W. M. Smith, "Vibrational Relaxation of NO by Atomic Oxygen," Chem. Phys. Letters, **66**, 218 (1979).

c K. Glänzer and J. Troe, "Vibrational Relaxation of NO in Collisions with Atomic Oxygen and Chlorine," J. Chem. Phys., **63**, 4352 (1975). For an estimate of the importance of multiquantum quenching, see M. Quack and J. Troe, "Complex Formation in Reactive and Inelastic Scattering: Statistical Adiabatic Channel Model of Unimolecular Processes III," Ber. Bunsenges. Physik Chem., **79**, 170 (1975).

d L. S. Rothman, et al., "The HITRAN Database: 1986 Edition," Appl. Opt., **26**, 4058 (1987).

TABLE A4. REACTIONS AND RATE CONSTANTS FOR H₂O MODEL.

Reaction	Rate Constant*	Reference
H ₂ O(010) + M = H ₂ O(000) + M	$1.10 \times 10^{-10} e^{-54.0/T^{1/3}}$	a,b
H ₂ O(100) + N ₂ = H ₂ O(020) + N ₂	$2.7 \times 10^{-14} T^{1/2}$	c
H ₂ O(100) + O ₂ = H ₂ O(020) + O ₂	$1.9 \times 10^{-14} T^{1/2}$	c
H ₂ O(100) + O = H ₂ O(020) + O	4×10^{-12}	d
H ₂ O(001) + N ₂ = H ₂ O(020) + N ₂	$2.7 \times 10^{-14} T^{1/2}$	c
H ₂ O(001) + O ₂ = H ₂ O(020) + O ₂	$1.9 \times 10^{-14} T^{1/2}$	c
H ₂ O(001) + O = H ₂ O(020) + O	4×10^{-12}	d
H ₂ O(001) + M = H ₂ O(100) + M	$1.4 \times 10^{-11} T^{1/2}$	e
H ₂ O(020) + M = H ₂ O(010) + M	$2.20 \times 10^{-10} e^{-54.0/T^{1/3}}$	f
H ₂ O(030) + M = H ₂ O(020) + M	$3.30 \times 10^{-10} e^{-54.0/T^{1/3}}$	f
H ₂ O(110) + M = H ₂ O(100) + M	$1.10 \times 10^{-10} e^{-54.0/T^{1/3}}$	a,b
H ₂ O(011) + M = H ₂ O(001) + M	$1.10 \times 10^{-10} e^{-54.0/T^{1/3}}$	a,b
H ₂ O(110) + N ₂ = H ₂ O(030) + N ₂	$2.7 \times 10^{-14} T^{1/2}$	g
H ₂ O(110) + O ₂ = H ₂ O(030) + O ₂	$1.9 \times 10^{-14} T^{1/2}$	g
H ₂ O(011) + N ₂ = H ₂ O(030) + N ₂	$2.7 \times 10^{-14} T^{1/2}$	g
H ₂ O(011) + O ₂ = H ₂ O(030) + O ₂	$1.9 \times 10^{-14} T^{1/2}$	g
H ₂ O(010) + O ₂ (0) = H ₂ O(000) + O ₂ (1)	$2.2 \times 10^{-11} / T^{1/2}$	a
H ₂ O(020) + O ₂ (0) = H ₂ O(010) + O ₂ (1)	$2.2 \times 10^{-11} / T^{1/2}$	a
H ₂ O(030) + O ₂ (0) = H ₂ O(020) + O ₂ (1)	$2.2 \times 10^{-11} / T^{1/2}$	a
H ₂ O(110) + O ₂ (0) = H ₂ O(100) + O ₂ (1)	$2.2 \times 10^{-11} / T^{1/2}$	a
H ₂ O(011) + O ₂ (0) = H ₂ O(001) + O ₂ (1)	$2.2 \times 10^{-11} / T^{1/2}$	a
H ₂ O(010) → H ₂ O(000) + hν	20.46	h
H ₂ O(020) → H ₂ O(000) + hν	0.501	h
H ₂ O(100) → H ₂ O(000) + hν	5.79	h
H ₂ O(001) → H ₂ O(000) + hν	82.51	h
H ₂ O(030) → H ₂ O(000) + hν	0.005	h
H ₂ O(110) → H ₂ O(000) + hν	0.596	h
H ₂ O(011) → H ₂ O(000) + hν	17.09	h
H ₂ O(020) → H ₂ O(010) + hν	35.27	h

TABLE A4. (CONTINUED)

Reaction	Rate Constant*	Reference
$\text{H}_2\text{O}(100) \rightarrow \text{H}_2\text{O}(010) + h\nu$	1.34	h
$\text{H}_2\text{O}(001) \rightarrow \text{H}_2\text{O}(010) + h\nu$	2.21	h
$\text{H}_2\text{O}(030) \rightarrow \text{H}_2\text{O}(010) + h\nu$	1.13	h
$\text{H}_2\text{O}(110) \rightarrow \text{H}_2\text{O}(010) + h\nu$	5.12	h
$\text{H}_2\text{O}(011) \rightarrow \text{H}_2\text{O}(010) + h\nu$	77.20	h
$\text{H}_2\text{O}(030) \rightarrow \text{H}_2\text{O}(020) + h\nu$	40.28	h

* Rate constants are in units of 1/s for unimolecular reactions, $\text{cm}^3/\text{molecule-s}$ for bimolecular reactions and $\text{cm}^6/\text{molecule-s}$ for termolecular reactions.

a H. E. Bass and F. D. Shields, "Vibrational Relaxation and Sound Absorption in $\text{O}_2/\text{H}_2\text{O}$ Mixtures," J. Acoust. Soc. Am., **56**, 856 (1974).

b R. T. V. Kung and R. E. Center, "High Temperature Vibrational Relaxation of H_2O by H_2O , He, Ar, and N_2 ," J. Chem. Phys., **62**, 2187 (1975).

c J. Finzi, F. E. Hovis, V. N. Panfilov, P. Hess, and C. B. Moore, "Vibrational Relaxation of Water Vapor," J. Chem. Phys., **67**, 4053 (1977).

d P. F. Zittel and D. E. Masturzo, Vibrational Relaxation of H_2O from 295 to 1020 K," J. Chem. Phys., **90**, 977 (1989).

e Gas kinetic estimate.

f Estimate based on SSH theory, $k_{n \rightarrow n-1} = nk_{1 \rightarrow 0}$.

g Estimate based on $k_{1n0 \rightarrow 0n+20} = k_{100 \rightarrow 020}$ or $k_{0n1 \rightarrow 0n+20} = k_{001 \rightarrow 020}$.

h L. S. Rothman, et al., "The HITRAN Database: 1986 Edition," Appl. Opt., **26**, 4058 (1987).

TABLE A5. REACTIONS AND RATE CONSTANTS FOR CO MODEL.

Reaction	Rate Constant*	Reference
CO(1) + M = CO(0) + M	$9.90 \times 10^{-9} e^{-168.1/T^{1/3}}$	a
CO(2) + M = CO(1) + M	$1.98 \times 10^{-8} e^{-168.1/T^{1/3}}$	b
CO(1) + O = CO(0) + O	$2.82 \times 10^{-9} e^{-75.4/T^{1/3}}$	c,d
CO(2) + O = CO(1) + O	$2.82 \times 10^{-9} e^{-75.4/T^{1/3}}$	e
CO(2) + O = CO(0) + O	$2.82 \times 10^{-9} e^{-75.4/T^{1/3}}$	e
CO(0) + N ₂ (1) = CO(1) + N ₂ (0)	$6.98 \times 10^{-13} e^{-25.6/T^{1/3}}$	a
CO(1) → CO(0) + hν	30.96	f
CO(2) → CO(1) + hν	60.45	f
CO(2) → CO(0) + hν	1.03	f

* Rate constants are in units of 1/s for unimolecular reactions, cm³/molecule-s for bimolecular reactions and cm⁶/molecule-s for termolecular reactions.

a R.L. Taylor, "Energy Transfer Processes in the Stratosphere," Can. J. Chem., **52**, 1436 (1974).

b Estimate based on SSH theory, $k_{21} = 2k_{10}$

c R. E. Center, "Vibrational Relaxation of CO by O Atoms," J. Chem. Phys., **58**, 5230 (1973).

d M. E. Lewittes, C. C. Davis, R. A. Mcfarlane, "Vibrational Deactivation of CO by Oxygen Atoms," J. Chem. Phys., **69**, 5230 (1978).

e Estimate.

f L. S. Rothman, et al., "The HITRAN Database: 1986 Edition," Appl. Opt., **26**, 4058 (1987).